UNIVERSITY OF CALIFORNIA
Santa Barbara

A Study of the Decay $D^0 \to K^-\pi^+\pi^0$ in High Energy Photoproduction

A Dissertation submitted in partial satisfaction
of the requirements for the degree of
Doctor of Philosophy
in
Physics
by

Donald Joseph Summers

Committee in charge:
Professor Rollin J. Morrison, Chairman
Professor Steven J. Yellin
Professor Raymond F. Sawyer

March 1984

The thesis of Donald Joseph Summers is approved:

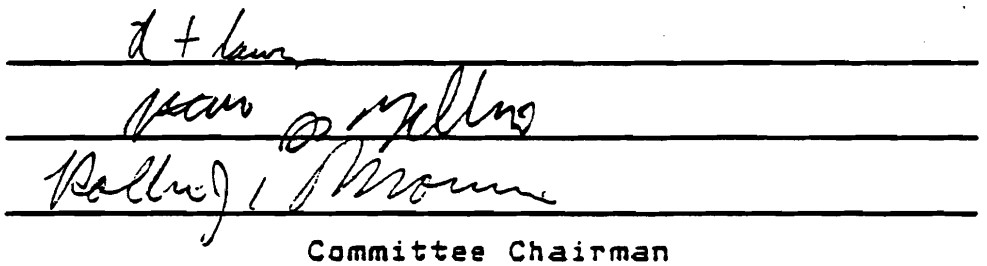

Committee Chairman

March 1984

ACKNOWLEDGEMENTS

I take great pleasure in thanking all the members of the the Tagged Photon Collaboration who have just spent some half million odd hours exploring the frontiers of the universe. The members of this unique group are:

Rolly Morrison, Vinod Bharadwaj, Don Summers, Al Lu, Al Eisner, Steve Yellin, Dave Caldwell, Bruce Denby, Mike Witherell, Rosemary Kennett, Umeshwar Joshi
(University of California, Santa Barbara 93106)

Penny Estabrooks, Jim Pinfold
(Carleton University, Ottawa K1S 5B6)

Sampa Bhadra, Alan Duncan, Dave Bartlett, Jim Elliott, Uriel Nauenberg
(University of Colorado, Boulder 80302)

Jeff Appel, Joe Biel, Tom Nash, Dave Bintinger, Bill Schmidke, Lisa Chen, Kees Daum, Mike Sokoloff, Ken Stanfield, Krzysztof Sliwa, Marcia Streetman, John Bronstein, Paul Mantsch, Suzanne Willis
(Fermilab, Batavia, Illinois 60510)

Mike Losty
(National Research Council of Canada)
(Montreal Road, Ottawa, Ontario K1A 0R6)

George Kalbfleisch, Mike Robertson
(University of Oklahoma, Norman 73019)

John Martin, George Luste, Gerd Hartner, Carl Zorn, Doug Gingrich, Jeff Spalding, Khatchik Shahbazian, Jim Stacey, Dale Blodgett, Bob Sheperd, Ravi Kumar, Steve Bracker
(University of Toronto, Toronto M5S 1A7)

I thank my advisor, Professor Rolly Morrison, for all his help and support, and particularly for entrusting me with the responsibility for a few fairly large segments of our experiment, so that I might have the opportunity to learn about experimental physics in detail.

For their friendship and help over the years, I thank Vinod Bharadwaj and Bruce Denby. Their presence added greatly to my enjoyment of the experiment.

For their leadership and enormous efforts in bringing the experiment up, I thank Tom Nash and John Martin. I also thank John Martin for teaching me about triggers.

I thank Mike Witherell and Kris Sliwa for their

excellent assistance with the data analysis. They have been a pleasure to work with.

The support of the Fermilab technical and computing staffs, as well as the UCSB machine and electronics shop staffs, was excellent. I particularly thank Dave Hale and Rudi Stuber for their superb efforts during the construction of the SLIC and Outriggers.

I thank Carol Denby for making Figure 52, the Outrigger $D^{*+} - D^0$ mass difference peak, possible.

I have profited greatly from the help and advice of Umeshwar Joshi, Jim Elliott, Dave Bintinger, Penny Estabrooks, Jeff Spaulding, Jeff Appel, John Bronstein, Marcia Streetman, Gerd Hartner, Mike Sokoloff, Dave Tanner, and Steve Bracker. I take this opportunity to thank them.

I thank my fellow custodian, Jim Pinfold, for his years of service.

Special thanks to Mike Robertson for rescuing the muskrat. Not only was a poor confused creature set free but also most of Tagged Photon's cables were

saved in the bargain.

For their invaluable assistance with the figures, I thank Bruce Denby, Alan Duncan, Rolly Morrison, Gerd Hartner, Tony Korda, D. J. McLaren, Dan Callahan, Carmen Vera, Gary Smith, and Roland Egloff.

Finally, I would like thank my mother, Helen Summers, who has always provided such great moral and financial support for my educational endeavors and to dedicate this thesis to the memory of my father, Joseph Summers.

VITA

[redacted]

1973--B.A., Physics and Economics,
University of California, Santa Cruz

1973-1975--Teaching Assistant, Montana State University

1975--Research Assistant, Montana State University

1975--M.S., Physics, Montana State University

1975-1977--Teaching Assistant and EOP Tutor
University of California, Santa Barbara

1977-1984--Research Assistant, High Energy Physics,
University of California, Santa Barbara

PUBLICATIONS

with V.K. Bharadwaj et alii, An Inexpensive Large Area Shower Detector with High Spatial and Energy Resolution, Nuclear Instruments and Methods 155 (1978) 411.

D.J. Summers et alii, Study of the Decay $D^0 \to K^- \pi^+ \pi^0$ in High-Energy Photoproduction, Physical Review Letters 52 (1984) 410.

with B.H. Denby et alii, Inelastic and Elastic Photoproduction of J/ψ(3097), Physical Review Letters 52 (1984) 795.

with K. Sliwa et alii, A Study of D* Production in High-Energy γp Interactions, FERMILAB-Pub-83/96-EXP 7320.516 (November 1983)

ABSTRACT

A Study of the Decay $D^0 \rightarrow K^-\pi^+\pi^0$

in High Energy Photoproduction

by

Donald Joseph Summers

A study of the charmed decay $D^0 \rightarrow K^-\pi^+\pi^0$ is presented. D^{*+} mesons were produced in a liquid hydrogen target by the Fermilab Tagged Photon Beam, which consisted of photons between 60 and 160 GeV. The 5.8 Mev/c^2 $D^{*+}-D^0-\pi^+$ mass difference was exploited to observe two decay cascades; $D^{*+} \rightarrow D^0\pi^+$, $D^0 \rightarrow K^-\pi^+$ and $D^{*+} \rightarrow D^0\pi^+$, $D^0 \rightarrow K^-\pi^+\pi^0$, $\pi^0 \rightarrow \gamma\gamma$. We built and used a spectrometer, which had almost full acceptance for photons and charged particles, to detect these decay products. The relative efficiency of the spectrometer for detecting these two decay cascades was determined with a Monte Carlo simulation, which allowed us to find $B(D^0 \rightarrow K^-\pi^+\pi^0) / B(D^0 \rightarrow K^-\pi^+)$. Using the current branching ratio for $D^0 \rightarrow K^-\pi^+$ of 2.4±0.4% [1], we obtained a value of 10.3±3.7% for $B(D^0 \rightarrow K^-\pi^+\pi^0)$. A fit to the $K^-\pi^+\pi^0$ Dalitz plot yielded branching ratios for $K^-\rho^+$, $K^{*-}\pi^+$, $\bar{K}^{*0}\pi^0$, and non-resonant final states. As compared to a previous result [2], we observed a significantly higher non-resonant branching ratio and a significantly lower branching ratio for $K^-\rho^+$. This new $K^-\rho^+$ result is in approximate agreement with the value expected for an I=1/2 final state [3].

TABLE OF CONTENTS

I. INTRODUCTION

Before discussing the weak decays of charmed D^0 mesons, I will first say a few words about the recent history of weak interactions and the charmed quark. The Weinberg-Salam gauge theory [4, 5, 6] united weak and electromagnetic interactions by introducing three massive vector bosons (W^+, W^-, and Z^0) to go along with the photon, a massless vector boson. These massive vector bosons mediate weak interactions just as the photon mediates electromagnetic interactions. This theory is consistent with hyperon decays and nuclear β-decays. In 1973 the weak neutral currents predicted by the theory were seen [7, 8] in reactions such as $\nu p \rightarrow \nu + X$. Recently the $W^{\pm}$ and Z^0 have been found at CERN's 540 GeV $p\bar{p}$ collider with masses near 81 and 93 GeV/c^2, respectively [9, 10, 11].

In its 3 quark version, the Weinberg-Salam theory has one left handed doublet $\begin{pmatrix} u \\ d' \end{pmatrix}_L$, one left handed singlet s_L, and three right handed singlets u_R, d_R, and s_R. The weak current eigenstate d′ is related

to the mass eigenstates by $d' = \cos\theta_C d + \sin\theta_C s$, where θ_C is the Cabibbo mixing angle (experimentally ~13°). Strangeness changing neutral currents are predicted by the last term in the expression $d'\bar{d}' = \cos^2\theta_C d\bar{d} + \sin^2\theta_C s\bar{s} + \cos\theta_C \sin\theta_C (d\bar{s} + s\bar{d})$. This prediction requires a much higher rate for the reaction $K^0_L \rightarrow \mu^+\mu^-$ than is experimentally observed. In 1970 Glashow, Iliopoulos, and Maiani (GIM) [12] were able to cancel this strangness changing neutral current by adding a fourth quark with the new quantum number charm. This 4 quark version of the Weinberg-Salam theory has two left handed doublets $\begin{pmatrix} u \\ d' \end{pmatrix}_L$ and $\begin{pmatrix} c \\ s' \end{pmatrix}_L$ plus four right handed singlets u_R, d_R, c_R, and s_R. The definition of d' is the same as before and s' is $\cos\theta_C s - \sin\theta_C d$. The strangness-flavor changing neutral current cross terms now cancel because $(d'\bar{d}' + s'\bar{s}') = (d\bar{d} + s\bar{s})$. The discovery of the J/ψ and particles with observable charm has added confirmation to the GIM theory. The GIM prediction that the decay of charmed quarks into strange quarks would be Cabibbo favored by the factor $\cot^2\theta_C$ has also been confirmed [3].

We chose to produce charm with photons and a fixed target, because it has certain advantages over the more usual choice of e^+e^- colliders. Due to the Lorentz boost, less solid angle must be covered to provide almost full acceptance, and threshold Cerenkov counters can be used for particle identification. Photon reconstruction efficiencies tend to be less sensitive to the energies of decay products in the center of mass frame.

We chose a photon beam instead of a hadron beam, because photons are partially composed of virtual quark-antiquark pairs, and in particular display a sizable coupling to $c\bar{c}$ pairs, while hadronic beams must fish charm out of the quark sea. Photoproduction has an order of magnitude less hadronic background than hadroproduction. And finally, we chose photoproduction because it allowed us to study different production mechanisms.

The non-leptonic weak decays of charmed D mesons include two-body, quasi-two-body, and non-resonant three-body final states. These branching ratios are of fundamental importance in determining the

contributions of spectator quark and W-exchange diagrams to the D meson decay process [3, 13-19].

To study this question, we observed two decay cascades; $D^{*+} \to D^0\pi^+$, $D^0 \to K^-\pi^+$ and $D^{*+} \to D^0\pi^+$, $D^0 \to K^-\pi^+\pi^0$, $\pi^0 \to \gamma\gamma$. (The charge conjugate is implicitly included for all reactions.) We have measured the relative branching ratios of these two decay modes, and from the $D^0 \to K^-\pi^+\pi^0$ Dalitz plot (normalizing to the $D^0 \to K^-\pi^+$ rate) we have measured the quasi-two-body ($K^-\rho^+$, $\bar{K}^{*0}\pi^0$, and $K^{*-}\pi^+$) and non-resonant three-body branching ratios. Our results for the contributions from $K^-\rho^+$ and non-resonant three-body modes differ from those reported previously [2]; we observe a significant non-resonant branching ratio, and we observe a smaller $K^-\rho^+$ branching ratio, which is in significantly better agreement with I=1/2 dominance.

Our isospin measurement helps illuminate the nature of weak charmed meson decay. The W-exchange diagram requires an I=1/2 final state; the isospin of the spectator diagram final state is, on the other hand, an unknown mixture of I=1/2 and I=3/2.

One quark contributes to the isospin of the W-exchange diagram, while three quarks contribute to the isospin of the spectator quark diagram (see Figure 1). Our results are consistent with the W-exchange model, but do not necessarily require it.

The remaining pages of this introduction are devoted to hardware and software. The parts of the experiment necessary to produce, detect, and analyze D mesons are emphasized. This experiment (E516) was performed at the Fermi National Accelerator Laboratory located in Batavia, Illinois using the Tagged Photon Spectrometer Facility [20,21]. Physicists from the National Research Council of Canada, Carlton University, the University of Toronto, Fermilab, the University of Oklahoma, the University of Colorado, and the University of California at Santa Barbara built the spectrometer and performed the experiment. (Complementary descriptions of E516 may be found in Ph.D. theses by Bruce Denby [22] and Alan Duncan [23].)

The D*+ events were produced by colliding photons of known energies ranging from 60 to 160 GeV with

protons in a liquid hydrogen target. Thus, adequate center of mass energies ranging up to 16 GeV were available to photoproduce $c\bar{c}$ pairs. An almost full acceptance spectrometer was used to detect forward particles. Figures 2 and 3 shows the relative locations of detectors in the spectrometer. We measured charged track momenta with a system of two analyzing magnets and 29 Drift Chamber planes. Two multicell threshold Cerenkov counters were used to identify charged particles. These counters were of particular importance to the D^{*+} signal; they allowed us to tell the difference between pions and kaons in the 6 to 37 GeV/c momentum range. The Segmented Liquid Ionization Counter (SLIC) and a pair of smaller Outrigger counters were used as electromagnetic calorimeters to detect photons and to identify electrons and positrons. Thus, the π^0's which were essential to finding the $D^0 \rightarrow K^-\pi^+\pi^0$ signal, were available.

The basic trigger demanded the presence of a tagged photon and a hadronic interaction in the target. Photons are 200 times as likely to produce

e^+e^- pairs as hadrons. Therefore, the trigger was designed to reject pairs. This was achieved by requiring that 30% or more of the tagged photon energy be found in the forward electromagnetic and hadronic calorimeters, outside the SLIC pair plane. Because the opening angle of e^+e^- pairs is very small, they were spread into a horizontal plane by the magnets. The opening angle, which is dominated by multiple scattering, is given by $21\sqrt{t/E}$, where t is the thickness of the target in radiation lengths and the energy E is measured in MeV. This angle is typically one milliradian. We used recoil particles to select high missing forward mass events from the basic hadronic trigger events. This selection reduced the number of events to be recorded by an order of magnitude. These particles were measured and identified in a recoil detector consisting of three cylindrical proportional wire chambers and four layers of scintillation counters. A fast data driven trigger processor combined the tagged photon energy with the recoil information to calculate the missing mass of hadronic events. The trigger

processor was used to demand either a single recoil proton at the primary vertex with high missing mass or more than three recoil particles. In summary, our trigger preferentially selected high mass hadronic interactions, which reduced the number of hadronic events to a level which could be recorded on tape.

After building the Tagged Photon spectrometer, we produced events, reconstructed particle 4-vectors, and found the D meson signals. Approximately 18 million recoil triggers were written onto one thousand 6250 byte per inch magnetic data tapes during the months from December 1980 through June 1981. The 4-vectors of particles in these events were reconstructed using programs containing some 60000 lines of Fortran code. Five separate computer systems were used for 4-vector reconstruction, including a six IBM 370/168 emulator system built by our University of Toronto colleagues. (The computing requirements of modern multi-particle spectrometers are enormous.) With the 4-vectors in hand, we devised cuts to extract the D meson

signals, and then performed a Monte Carlo calculation to find the reconstruction efficiencies for the $K^-\pi^+\pi^+$ and $K^-\pi^+\pi^0\pi^+$ final states. A fit to the $K^-\pi^+\pi^0$ Dalitz plot yielded branching ratios for $K^-\rho^+$, $K^{*-}\pi^+$, $\bar{K}^{*0}\pi^0$, and non-resonant final states. This investigation has resulted in the largest sample of $D^0 \to K^-\pi^+\pi^0$ decays, the dominant D^0 decay mode, reported to date.

II. TAGGED PHOTON BEAM

A. ELECTRON BEAM

The tagged photon beam began one mile southwest of TPL in a cylinder of hydrogen gas. The hydrogen atoms were stripped of their electrons by an electric arc to yield protons which were accelerated to 800 keV in the Cockcroft-Walton, to 200 MeV in the LINAC, and to 8 GeV in the booster ring, before being injected into the main proton synchotron [24] (see Figures 4 through 8). Once in the main ring of magnets, 16 radio frequency cavities, at location F0, accelerated the protons to 400 GeV. The RF cavities also grouped the protons, which usually numbered somewhat fewer than 2×10^{13} per spill, into buckets two nanoseconds long and 18.5 nanoseconds apart. This acceleration cycle was repeated every 10 seconds.

The beam was then extracted from the main ring during a one second spill and split by septa into 3 beams which went to the Meson, Neutrino, and Proton

experimental areas. The Proton area beam was further split into beams for the P-West, P-Center, and P-East areas.

The P-East beam (~4×10^{12} protons/spill) was directed onto a 30 cm long beryllium target. Charged particles coming from this target were magnetically guided into a dump while neutrals such as photons from π^0 decays, neutrons, and K_L^0's continued on to a half radiation length lead target. Electrons produced by the reaction, $\gamma Z \rightarrow e^+e^-Z$, in the lead target were transported by 11 magnets away from non-negatively charged particles to a thin copper radiator. These magnets, in conjunction with 4 collimators, allowed one to tune the final electron beam momentum to any value between 5 and 300 GeV/c with a momentum resolution of ±2.5%. The π^- particles produced along with the electrons in the lead target were reduced to the 1% level in the electron beam by exploiting their production at relatively high transverse momentum. The vertical collimator, CV423, was positioned to intercept these pions. The electrons passed through this

collimator, because they had been produced virtually parallel to photons from the beryllium target and were only spread horizontally by the main bending magnets due to their differing momenta.

B. TAGGING SYSTEM

The monochromatic electron beam produced bremsstrahlung photons as it hit the 1/5 radiation length copper radiator. Three tagging magnets bent each electron to the east as shown in Figure 9. Those which radiated a high energy photon entered a scintillation strip hodoscope (H1-H13) and shower counter block (L1-L13) unit. A coincidence between a hodoscope strip and a corresponding shower counter block defined a TAG. The coincidence also demanded that the electromagnetic shower counter energy measurement (E′) and the hodoscope momentum measurement be consistent with an electron. Thus the energy of the photon which continued on to the spectrometer was

$$E_{\gamma} = E_{BEAM} - E'.$$

Tagged photons were produced virtually parallel to the electron beam. The typical divergence of a milliradian was a sum in quadrature of the electron beam divergence, the production angle ($\theta=m/E$), and multiple scattering ($\theta=21\sqrt{t}/E$, where t is in

radiation lengths and E is in MeV).

The problem of multiple bremsstrahlung in the radiator was solved by placing 3 small tungsten-scintillator shower counters in and near the beam just in front of the SLIC. The central counter in this array of electromagnetic shower detectors was called the C-Counter and was used to measure the energy of photons which did not interact in the hydrogen target. The two neighboring counters, C-East and C-West, were used to measure the energy of photons which produced high energy e^+e^- pairs in the target. Calling the energy detected in the C-Counter E_C, the tagged photon energy may be appropriately corrected.

$$E_\gamma = E_{BEAM} - E' - E_C$$

The energy spectrum of tagged photons produced by a 170 GeV electron beam is shown in Figure 10.

III. TAGGED PHOTON SPECTROMETER FACILITY HARDWARE

A. LIQUID HYDROGEN TARGET

E516 used a target consisting of a 2" diameter 5 mil mylar flask 150 centimeters long filled with liquid H_2. Hydrogen was chosen as a target material because its nucleus is simple, a single proton, and because its liquid density is low enough (ρ=0.0708 g/cm^3) to usually permit recoiling particles to escape. To provide thermal insulation with a minimum of mass a 5" outside diameter, 1/2" thick Rohacell foam vacuum jacket covered with another 5 mils of mylar was employed. The mylar and foam presented 0.103 gm/cm^2 to protons recoiling at 90°, as compared to 0.36 gm/cm^2 for 2" of liquid H_2. The length of the target was chosen to maximize the event rate while minimizing secondary interactions. Our 150 centimeter liquid H_2 target was 0.17 radiation lengths and 0.25 nuclear collision lengths long.

B. RECOIL DETECTOR

A recoil detector consisting of three cylindrical proportional wire chambers (PWC's), and four cylindrical layers of segmented scintillation counters (plastic A and B layers, liquid C and D layers) was used to find the four-vectors of particles emerging from the hydrogen target at large angles to the beam direction. The recoil detector is shown in Figure 11 and is described in Reference [25].

The main purpose of the Recoil Detector was to measure the forward missing mass (M_X) in the case of a single recoil proton.

$$M_X^2 = P_X^2 = (P_f - P_i - P_{TAG})^2$$

$$= (E - m - E_{TAG})^2 - (\vec{p} - \vec{p}_{TAG})^2$$

$$= 2E_{TAG}(p\cos\theta - T) + T^2 - p^2$$

$$= 2E_{TAG}(p\cos\theta - T) - 2mT$$

where P_{TAG}, P_i, and P_f are the 4-vectors of the incident photon, initial proton, and final proton,

respectively; and p, m, E, T, and θ are the 3-momenta, mass, energy, kinetic energy, and angle with respect to the incident photon, of the final proton, respectively.

The trajectories of charged recoil tracks were determined by the three PWC's placed concentrically around the hydrogen target. Longitudinal anode wires were used to measure the azimuthal angle φ while circumferential copper cathode strips measured the polar angle θ. The spacing of the anode wires was 4 mm and the spacing of the cathode strips was 1.52 mm. The construction of the PWC's is shown in Figures 12 and 13.

Particle energies and identities were determined by comparing energy depositions in each of the four scintillation layers with Bethe-Bloch [25] dE/dx predictions. Each scintillation layer was divided into 15 segments in φ to allow the recoil detector to reconstruct events with more than one particle. Phototubes were placed on both ends of the first layer to measure longitudinal positions with end to end timing. This also permitted the identification

of slow particles which stopped in this layer by time of flight measurements. Phototube pulse heights were digitized by 12-bit LeCroy 2280 ADC's.

The recoil information was written onto the data tape and was also sent to the trigger processor which calculated the forward missing mass in a few microseconds.

C. ANALYZING MAGNETS

Two large aperture 5 kilogauss-meter magnets called M1 and M2 were used to analyze the momenta of charged particles created in the liquid hydrogen target. Fast forward particles, which went through both magnets, were measured with the entire spectrometer. Wide angle particles were detected with less resolution by a Drift Chamber (D2) and a pair of electromagnetic calorimeters (Outriggers) placed between M1 and M2. Figures 14 and 15 picture the magnets.

Precise magnetic field measurements were needed to convert Drift Chamber track positions into accurate particle momenta. What was the precision necessary to match the Drift Chamber resolution? A Drift Chamber plane with a resolution of 200 microns placed 2 meters from the center of a magnet requires that the bend angle error($\Delta\theta$) be less than 0.1 milliradian. Thus for a typical 5 GeV/c track an error less than 0.017 kilogauss-meters or 1/3% of 5 kilogauss-meters is essential.

$$\vec{dp}/dt = (q/c)(\vec{v}\times\vec{B}), \quad dt = \vec{d\ell}/\vec{v}$$

$$\Delta\theta = \vec{dp}/\vec{p} = (q/\vec{pc})\vec{B}\cdot\vec{d\ell}$$

$$\vec{B}\cdot\vec{d\ell} = \Delta\theta(pc/q)$$

$$\Delta\int\vec{B}\cdot\vec{d\ell} = \Delta\theta(5GeV/c)/(10^{-10}c) = .0005/.03 = .017 \text{ kg-m}$$

Because the magnetic field integral was a function of particle trajectory a map was made of each magnet using the Ziptrack [26], prior to data taking. Ziptrack is a Fermilab magnet mapping machine, which used three small mutually perpendicular coils with a common center to measure the field. A miniature cart carried the coils down an aluminum rail parallel to the beam line. The changing magnetic field induced a current in the coils as predicted by Faraday's Law. The magnetic gradient integration was repeated and thus double checked on the cart's return to its origin. Two computer controlled A-frame manipulators moved the aluminum rail horizontally and vertically. Shaft encoders kept track of the X and Y coordinates set by the A-frames as well as the Z position of the cart along the aluminum rail. Each coil was

connected to its own integrator which added up the induced current. Because the cart started in a field free region the integration constant was always zero. The integrated field was digitized by a 12-bit ADC after each 0.5112" movement of the cart. A PDP-11/05 computer provided overall control through a CAMAC interface, and also wrote the coil positions and magnetic field values onto 9-track magnetic tapes. Approximately 2 million field measurements were made spaced along 4"x2"x0.5112" grids. M1 was mapped at 1800 amps and 2500 amps. M2 was mapped at 900 amps, 1800 amps, and 2500 amps. Saturation of the iron caused scaling of the M2 magnetic field with current to be about 4% non-linear by the time it reached 2500 amps.

The magnetic fields were measured to an accuracy better than the 1/3% necessary. This conclusion is based on duplicate measurements of points, comparison of nearby points, and the symmetry of the field around the beam axis.

The magnetic field maps were fit to polynomials which where used in the tracking reconstruction.

Functions [27, 28, 29] and polynomials whose divergence and curl vanish have the advantage that they constrain the magnetic field to obey Maxwell's equations in a current free region.

$$\vec{\nabla} \cdot \vec{B} = \vec{\nabla} \times \vec{B} = 0$$

Average magnetic field deviations of 0.1% were found by fitting such functions. Thus, the field measurements are consistent with Maxwell's equations. The data reduction program, however, used ordinary polynomials to save computer time.

Not only must the magnetic fields be known as a function of space, they must be known as a function (hopefully constant) of time as well. The analyzing magnets were monitored several different ways during the run to make sure that the fields remained constant($\Delta B/B < 1/3\%$).

First, the direct current supplied to each magnet was continuously measured and regulated by the beam line computer.

Second, nuclear magnetic resonance was used not only to establish the absolute central field of each

magnet but also to check that the M1 field remained constant during the data run (December 1980 through June 1981). With M1 set to 1800 amps the NMR gave readings of 3866 gauss on 11 September 1980, 3863 gauss on 29 January 1981, and 3865 gauss on 29 March 1981. The M1 field jitter is 0.04%, according to the NMR, which is well below 1/3%.

Third, each magnet's current was checked daily by measuring the voltage drop across a 10 μ ohm shunt in series with it. Typical deviations were at the 0.1% level, while the accuracy of the DVM used to read the shunt voltage was 0.03%.

Fourth, Hall probes were glued onto the pole faces of each magnet to monitor the actual magnetic fields continuously. The output voltages from the Hall probe electronics (F.W.Bell Model 620 Gaussmeters; rated accuracy 0.25%) were amplified by Precision Monolithics OP-07AJ ultra-low offset voltage operational amplifiers so as to exploit the 12 bit LeCroy 2232 ADC's capability of resolving 1/3% errors. As a precaution, the digitized voltages were written onto the data tape once per

beam spill, so that the magnetic fields could be calculated on a spill by spill basis for the offline analysis. The stability of the magnets made this unnecessary in practice. The Hall probes also allowed the online monitor program to issue warnings if the magnetic fields changed.

And finally, a monitoring system made sure that the voltage drop across each coil in a magnet was the same. Differences would have indicated turn to turn shorts between the windings in the magnets. None were detected in the period from December 1980 through June 1981.

In summary, values of the magnetic fields were understood at the one part in 500 level, enough to preserve the resolution of the spectrometer. This conclusion is further supported by the finding of the K^0_S mass at 497.85±0.29 MeV/c^2, within 0.04% of the accepted value of 497.67±0.13 MeV/c^2. This result is based on 1900 $K^0_S \rightarrow \pi^+\pi^-$ events with no adjustment to the original field maps.

TABLE 1. PROPERTIES OF THE ANALYZING MAGNETS

Magnet	M1	M2
Number	AN444C	AN445C
Name	Akhennaten	Beketaten
+X	West	West
+Y	Up	Up
+Z	Downstream	Downstream
Magnet Location	Upstream	Downstream
Pole Face Width (X)	183cm	183cm
Pole Face Gap (Y)	80.9cm	85.7cm
Pole Face Length (Z)	100cm	100cm
Total Length (Z)	165cm	208cm
Upstream Shield Plate Opening (X,Y)	(154cm, 73cm)	(154cm, 69cm)
Downstream Shield Plate Opening (X,Y)	(195cm, 97cm)	(188cm, 107cm)
Shield Plate Thickness(Z)	7.6cm	7.6cm
Number of Coils	2	4
Positive Particles Bend	West	West
12/80 → 6/81 Currents	1800 Amps	900 Amps
and Shunt Voltages	17.89 mV	9.06 mV
$\int B_y(0,0,Z)dZ$ at 900 Amps	Unknown	-5.34 kg-m
$\int B_y(0,0,Z)dZ$ at 1800 Amps	-5.01 kg-m	-10.69 kg-m
$\int B_y(0,0,Z)dZ$ at 2500 Amps	-7.08 kg-m	-14.35 kg-m
NMR B(0,0,0) at 900 Amps	1943 gauss	3680 gauss
NMR B(0,0,0) at 1800 Amps	3866 gauss	7293 gauss
NMR B(0,0,0) at 2500 Amps	5345 gauss	9751 gauss

D. DRIFT CHAMBERS

Four groups of Drift Chamber planes called D1, D2, D3, and D4 were used to find the trajectories, and in combination with the analyzing magnets the momenta of charged particles in the forward spectrometer. The Drift Chambers are illustrated in Figures 14 and 16 through 19.

Sets within each Drift Chamber consisted of U, V, and X (plus X′ in the center of D1) planes of wires. The X and X′ sense wires were both vertical, but offset one half cell spacing with respect to each other to add the redundancy of a fourth view, as well as the redundancy of an additional plane, in a highly congested area. The V and U sense wires were tilted at ±20.5° to the vertical. High voltage field wires (.005" diameter beryllium-copper) were alternated with 25 μm gold plated tungsten sense wires to form sense planes. These sense planes were sandwiched between high voltage planes to form drift cells around each sense wire (see Figure 18). By using these sets of closely spaced U, V, and X(X′)

views, physical locations in space could be found, with 2 views defining the location and the third view providing confirmation.

Two UVXX' sets formed D1. D2 and D3 each used 3 UXV sets while D4 contained a single UXV set. Thus, a charged track going from the target to the C-Counter would encounter 29 planes containing approximately 5000 sense wires. D1, D2, D3, and D4 used 0.1875", 0.375", 0.625", and 1.250" cell sizes, respectively, all cells being measured horizontally. The corresponding perpendicular distances between U and between V sense wires were 0.1756", 0.351", 0.585", and 1.171". This choice of spacing ratios allowed a constant wire crossing pattern over the entire active Drift Chamber area. Points where all three sense wires could cross, and make it difficult to tell which side of a wire a track passed, were eliminated.

The chambers were filled with equal parts argon and ethane. The drift velocity of electrons in this gas mixture is constant over a range of electric potential gradients, making it possible to easily

convert drift times into distances. A little ethanol vapor was added to D1 and D2 to increase quenching because these chambers experienced higher rates than D3 or D4.

The position of the ionization left by a charged track in a drift cell was determined by using LeCroy 2770 TDC's to digitize the time taken for primary ionization electrons to drift to a sense wire (anode) in the electric field. The drifting electron signal was amplified by avalanches of electrons caused by the high electric field next to the small 25 μm sense wires. LeCroy DC201 amplifier-discriminators were then used to further amplify the signal and send a logic pulse to the TDC's, if the discrimination level was exceeded. These times were written onto tape. Each TDC's offset with respect to its plane and each TDC's gain (nanoseconds per count) were determined and monitored with special BHD pulses [22] sent to the Drift Chambers between beam spills. The absolute timing (T_0's) of each plane was determined by looking at reconstructed data tracks.

E. CERENKOV COUNTERS

Two segmented threshold Cerenkov counters were used for charged particle identification in the forward spectrometer. The counters, called C1 and C2, are shown in Figures 15 and 20 through 23. Different thresholds for the production of Cerenkov light were achieved by using pure nitrogen in C1 and a 20% nitrogen 80% helium gas mixture in C2. The lengths of C1 and C2 were chosen to produce 15 and 16 photoelectrons respectively, under ideal conditions. Typically, we observed about half the ideal number of photoelectrons. The Cerenkov thresholds distinguished pions from kaons and protons in the momentum range from 6 to 20 GeV/c. Between 20 and 37 GeV/c all three particle types were identified and in the range from 37 to 71 GeV/c protons were distinguished from pions and kaons.

Particle identification in high multiplicity events was made possible by the segmentation of each counter into 20 cells. (Provision also was made to increase the number of cells in C1 to 28 and in C2

to 32 for a future experiment in a straightforward manner.) The central horizontal plane of C2 was shielded to contain light from e^+e^- pairs. Each cell used an aluminized slump molded acrylic mirror suspended by 7 dacron strings to focus the Cerenkov light into Winston cones (see Figures 22 and 23). The thin acrylic mirrors and dacron strings minimized secondary interactions and multiple scattering. The Cerenkov light was concentrated further by the aluminized ellipsoidal-like interiors of the Winston cones onto 5" RCA 8854 photomultiplier tubes. (The tubes were selected for their high photoelectron quantum efficiency (~18%) and high gain first dynodes.) The phototube outputs were then digitized by 10 bit LeCroy 2249 ADC's and written onto tape.

The refractive index ($\beta_{THRESH} = 1/n$) of the gas in each counter was determined from the observed pion threshold ($\beta = p/[p^2+m^2]^{1/2}$). The same pions were used to calculate the light collection efficiency of each cell. These calibrations were crucial to predicting the signal that should be

observed in each cell for a given set of tracks and mass hypotheses.

TABLE 2. CHARACTERISTICS OF THE CERENKOV COUNTERS

QUANTITY	C1	C2
Gas Mixture	100% N_2	80% He 20% N_2
Length	3.7 meters	6.6 meters
Refractive Index expected [30] 76cm-Hg 20°C λ=.35μm	1.000288	1.000084
Refractive Index from measured $\pi^{\pm}$ thresholds	1.000299	1.000088
Cerenkov Angle($\gamma\to\infty$ $\beta\to1$)	24 mrad	13 mrad
Electron Threshold	.021 GeV/c	.038 GeV/c
Muon Threshold	4.3 GeV/c	8.0 GeV/c
Pion Threshold	5.7 GeV/c	10.5 GeV/c
Kaon Threshold	20.2 GeV/c	37.1 GeV/c
Proton Threshold	38.3 GeV/c	70.6 GeV/c
Number of Cells	20	20
Cell Sizes(Width,Height)	(4",8")	(10",18")
	(8",8")	(20",18")
	(38",8")	(65",18")
	(12",16")	(30",32")
	(38",16")	(65",32")

F. OUTRIGGER ELECTROMAGNETIC CALORIMETERS

A pair of lead and plastic scintillator electromagnetic calorimeters (Outriggers) were placed above and below, and just upstream of the second analyzing magnet's entrance. These counters determined the 4-momenta of wide angle photons which would have missed the SLIC or been absorbed by M2, and also served to identify electrons and positrons seen in the Drift Chambers. The counters were skewed 3.5° to match the slope of incident particles. Thus the vertical separation between the Outriggers was 1.4" greater at the back of the counters than at the front. All structural parts of the Outriggers were made of aluminum to avoid perturbing the magnetic field maps. These calorimeters are shown in Figure 24.

The Outriggers each covered an area 57.5" wide and 18.75" high with twenty-three 2.5" wide X counters and fifteen 1.25" wide Y counters. Sixteen layers of 0.25" thick 96% lead 4% antimony plates, clad with 0.025" aluminum sheets, generated

electromagnetic showers from incident photons and electrons. Eight X layers and eight Y layers were interleaved to sample these showers and determine the energies of incident particles. Because showers were not completely contained in a single X or Y counter, neighboring energy depositions could be used to determine the position of a particle to a fraction of a counter width.

The Y counter scintillator strips were allowed to extend beyond the lead plates and were bent to guide their light to lucite mixing blocks. Each light mixing block was connected to a 2" RCA 4902 photomultiplier tube. The same RCA tube was used for the X counters.

The light from X counters passed through a UV absorbing filter (to flatten their attenuation curves) into wavebars. The light in each wavebar was reflected up into a light guide which was connected to a phototube. This rather contorted light collection scheme is illustrated in Figure 25.

During the early data runs (137 GeV), it was discovered that the excessive light collection

efficiency of the X view's seventh and eighth layers was degrading that view's electromagnetic resolution by a factor of three. Therefore, between the 137 GeV and 170 GeV runs 25% of the light coming from the seventh X layer and 90% of the light from the eighth X layer was masked to equalize the collection efficiency for each layer. A 2000 μC $_{27}Co^{60}$ β^- source was placed near each layer and photomultiplier signals were measured with a digital volt meter (1 μV resolution) to determine these efficiencies.

Magnetic fields can reduce the gain of a photomultiplier tube drastically by disturbing the trajectories of electrons between dynode, particularly in the relatively large space between the photocathode and the first dynode plate where the electron cascade begins. The field of M2, which amounted to hundreds of gauss in the vicinity of the Outriggers, had to be reduced to a small fraction of a gauss. This problem was solved by shielding the photomultiplier tubes so that the path of least resistance for the magnetic flux lines was around

rather than through the tubes. Jackson [31] shows that the field inside a spherical shell of inner radius a, outer radius b, magnetic permeability μ, and uniform external field B_0 is $-9b^3B_0/2\mu(b^3-a^3)$ in the limit that $\mu>>1$. Thus a material with a high μ was needed. The other important point to note is that the shield material's μ is a function of field density which increases to a maximum and then decreases rapidly as the material becomes saturated with magnetic flux. About twice the flux, which would have existed in the volume to be shielded, will be drawn into the shield material. The shields had to be made thick enough to avoid saturation.

Spot welded cylinders of 0.014" CO-NETIC Sheet [32] were placed around each tube. This alloy has a maximum permeability of 500000 and a saturation point of 7500 gauss. A thicker second shield made of 0.095" thick steel tubing was added to each X phototube. This outer shield had a maximum permeability of 2000 and a saturation point of 21000 gauss. The gap between the shields was made large enough so that the flux lines would go through the

steel rather than jumping to the CO-NETIC. The steel was chosen for its high saturation point and the CO-NETIC for its high permeability. The shields worked when M2 was at 900 or 1800 amps but failed at 2500 amps. The fringe fields, which grow non-linearly, increased at a faster rate than had been anticipated. However, no data was taken with M2 at 2500 amps.

The Outriggers were calibrated by moving them on their support posts into a 30 GeV electron beam. The Outriggers were calibrated twice in this manner. The resolution was found to be $20\%/\sqrt{E}$ with the masks installed. Special muon runs were taken every few weeks. These were used to determine individual attenuation lengths for each channel and also relative gain factors. This trigger used muons from the primary beryllium target and demanded a 4-fold coincidence between the Outriggers and parts of the upstream Muon Wall (see Figure 9), C2, and the downstream Muon Wall. Fiber optics [33] were used to direct short light pulses to each counter and, hence, to tell if a channel failed between muon

runs. The light came from the Nitrogen laser system shown in Figure 26. Ultraviolet light from the laser entered a piece of plastic doped with BBQ, a chemical which absorbs UV light. The BBQ molecules re-emited green light which traveled through the fiber optic cables.

TABLE 3. [34] FORWARD CALORIMETER CHARACTERISTICS

	SLIC	OUT-RIGGERS	HADRO-METER	C-EAST C-COUNTER C-WEST
Steel				
Thickness	0.20"	0"	36"	0"
Radiation Lengths	0.29		52.0	
Collision Lengths	0.05		8.96	
Interaction Lgths.	0.03		5.35	
Aluminum				
Thickness	5.72"	1.02"	0"	0"
Radiation Lengths	1.63	0.29		
Collision Lengths	0.57	0.10		
Interaction Lgths.	0.39	0.07		
Scintillator				Lucite [34]
Thickness	30.0"	5.15"	13.5"	3.75"
Radiation Lengths	2.21	0.30	0.80	0.27
Collision Lengths	1.51	0.24	0.62	0.19
Interaction Lgths.	1.13	0.19	0.50	0.15
Lead				Tungsten
Thickness	3.84"	4.00"	0"	3.75"
Radiation Lengths	17.4	18.1		27.2
Collision Lengths	0.99	1.04		1.70
Interaction Lgths.	0.52	0.55		0.92
Total Active				
Thickness	39.8"	10.17"	49.5"	7.5"
Radiation Lengths	21.5	18.7	52.8	27.5
Collision Lengths	3.12	1.38	9.58	1.89
Interaction Lgths.	2.07	0.81	5.85	1.07
Number of Layers	60	16	36	60
No. of Channels	334	76	142	3
Views	UVY	XY	XY	--
Size (X)	192"	57.5"	192"	2.62" 2.5" 2.62"
Size (Y)	96"	18.75"	108"	3.5" 4.5" 3.5"

I. SLIC ELECTROMAGNETIC CALORIMETER

The Segmented Liquid Ionization Counter (SLIC) was used in conjunction with the Outriggers to find photons and to identify electrons and positrons seen in the Drift Chambers. This provided us with the ability to reconstruct π^0's and find the $D^0 \rightarrow K^-\pi^+\pi^0$ signal. Channels filled with liquid scintillator (Nuclear Enterprises NE235A), and lined with teflon to provide total internal reflection, were used to bring light from particle showers to the U, V, and Y view readouts of the SLIC. The third view helped to resolve reconstruction ambiguities by confirming the presence of a real shower found in the first two views. This channel design provided optical attenuation lengths of almost two meters, which minimized the functional dependence of shower energies on longitudinal position. Figures 27 through 29 picture the SLIC. Reference [35] describes a prototype, while References [22] and [36] detail the SLIC itself.

The 192" wide by 96" high SLIC consisted of 60

1/2" thick layers of liquid scintillator used to sample the electromagnetic showers generated by 0.065" thick lead sheets placed between each scintillation layer. Each scintillation layer was divided into 1.25" wide light channels by 0.016" thick teflon coated aluminum bent into square wave corrugations. Typically, 60% of an electromagnetic shower was contained in a 1.25" slab parallel to the shower axis. Therefore, the energy depositions in neighboring counters could be used to find the position of a shower to a small fraction of an inch. Channels tilted at ±20.5° to the vertical formed the V and U views. Channels of the Y view were horizontal and were also divided in the middle by mirrors. Mirrors were also placed at the ends of the U and V channels to increase their optical attenuation lengths. There were 20 layers devoted to each view interleaved in the order UVY, UVY, etc.

Adhesive sheets were used to clad each lead sheet with 0.040" thick aluminum to support the lead and prevent it from poisoning the liquid scintillator. A hollow plywood vacuum table kept the metal sheets

flat during the lamination process. Next the lead-aluminum laminate was moved to the first of two 8'x16' tilting tables. Teflon tape was applied on one side and then the laminate was flipped by tilting the table 90°, picking it up with a 25 foot high crane and rotating 180°, putting it back on the table, and finally tilting the table back to its original horizontal position [37]. Teflon tape was then applied to the other side. The crane was then used to move the now teflon coated laminate to the second tilting table where the teflon coated aluminum corrugations were riveted into place to complete the light channels. Because teflon has a lower index of refraction (n=1.38) than liquid scintillator (n=1.47) the channels were totally internally reflecting for angles below 20°. Finally the completed laminate was moved into the SLIC tank by the crane. This process was repeated 59 times.

The front and back of the SLIC tank were made of Wirecomb [38] panels (see Figure 28) to provide a stiff surface to withstand the hydrostatic pressure of the liquid scintillator, while still allowing

particles to enter the SLIC without interacting. Acrylic (Rohaglas 2000), supported by 0.25" x 2" steel bars, was used for the sides of the SLIC to allow the scintillator light to reach the waveshifter bars while keeping the liquid scintillator inside the tank. The acrylic windows also absorbed UV light to increase the attenuation length of the liquid scintillator. The lucite wavebars were doped with 90 milligrams per liter of the chemical BBQ to shift the wavelength of the scintillator light from blue to green.

Channels in the middle of the SLIC were each optically connected through a small air gap to individual wavebars and then to 2" RCA 4902 photomultiplier tubes. Channels near the edges of the SLIC, where fewer particles hit, were paired together by double width wavebars epoxied to 3" RCA 4900 phototubes. There were 109 U channels (51 single and 58 double), 109 V channels (52 single and 57 double), and 116 Y counters (82 single and 34 double). The transistorized phototube base shown in Figure 30 was developed from a design by Cordon

Kerns [39]. We used these bases to supply voltages to the phototube dynode stages, which would be independent of the beam flux. The transistors kept the voltages independent of rate. The resistor values were chosen to obtain linear signal behavior up to a volt.

The dynode signals from all the Y counters not in the pair plane were summed together to form part of the TAG-H trigger (see page 49). The anode signals were digitized by LeCroy 2280 ADC's and written onto tape.

The entire SLIC was initially tested by sweeping a 5 GeV electron beam across almost every channel at several places. This allowed us to measure the optical attenuation of channels, and to match phototube gains to the 12 bit dynamic range of the ADC's. During the data taking, e^+e^- pair runs, taken every few weeks, allowed most of the U and V counters to be calibrated. The Hadrometer muon test runs were used to calibrate the Y channels. Muons left a minimum ionizing signal in the SLIC, equivalent to a 1/2 GeV shower. Wavebar shifted N_2

laser light pulses sent to each counter through DuPont PIFAX P-140 fiber optic cables were used to track gains between test runs. Because the number of laser generated photons varied from pulse to pulse, each counter was normalized to the average of all "good" counters in the SLIC. This assumes that the SLIC as a whole was not drifting significantly. The evidence from the pair runs was that the stability of the SLIC as a whole was better than 2%. The resolution of the SLIC over short periods in localized regions was $10\%/\sqrt{E}$ as determined by monochromatic electron beams on more than one occasion. Calibration uncertainties on the order of 2% and errors caused by the inability of our reconstruction program to invariably untangle overlapping showers must be added to this. The overall absolute calibration of the SLIC was adjusted slightly (~1%) to obtain the correct π^0 mass.

H. HADROMETER

A hadron calorimeter, consisting of 36 alternating layers of 1" thick steel plate and 3/8" thick by 5.7" wide scintillator strips, was used to measure the energy of hadrons with a resolution of $75\%/\sqrt{E}$. The calorimeter was divided into front and back modules of equal thickness by lucite light pipes which fed the scintillator light to upstream and downstream 5" EMI 9791KB photomultiplier tubes. Each module contained 33 vertical X strips and 19 horizontal Y strips which were divided in the middle. The Hadrometer appears in Figure 31.

The phototube anode signals were digitized by LeCroy 2280 ADC's and written onto tape. The Y dynode signals were added together to form an important part of the TAG.H trigger (see page 49).

Muon test runs were used to find an average optical attenuation length for the Hadrometer as well as relative gains of counters. A monochromatic π^- beam was used for the absolute calibration.

The Hadrometer provided the only source of

information about the energy of neutral hadrons (e.g. neutrons and K^0_L's) as well as supplementing the Drift Chamber measurements of charged hadrons. However, because of its poor resolution, the basic importance of the Hadrometer was not in precision energy measurements. Instead, we applied it to other more subtle areas such as the TAG·H trigger (see page 49), separating hadrons from muons which typically left a 2.4 GeV equivalent minimum ionizing track, and identifying neutral hadrons so they would not be labeled as photons by the SLIC.

I. MUON WALL

The last detector in the spectrometer was an 18' wide by 10' high wall of 15 scintillator strips used to detect muons (see Figures 32 and 33). Fourty inches of steel (6 interaction lengths) was placed between the Muon Wall and the Hadrometer to absorb any residual particles from showers in the Hadrometer. Thus, by the process of elimination only muons were available to create light in the scintillator. Plastic light guides connected the 18" and 24" wide scintillator strips to 5" EMI 9791KB photomultiplier tubes. Each PMT output was fed into a discriminator which set a latch bit if there was a muon. A TDC was used to determine the vertical position of the muon. Two small scintillation paddle counters were placed behind μ_{16}, the central Muon Wall counter, so that coincidences could be formed to reduce its high accidental rate. Three feet of concrete was placed between μ_{16} and the paddle counters to absorb spurious particles. The latch bits and TDC times were recorded on tape.

J. LOW LEVEL TRIGGERS

The main E516 trigger was divided into two parts. First, a low level trigger to separate hadronic interactions in the hydrogen target from e^+e^- pairs. And second, a high level missing mass trigger which separated low mass hadronic states from high mass hadronic states.

The main low level trigger was TAG·H (see Figure 34). A logical TAG signal generated by the tagging system indicated the presence of a photon. The H part of the trigger stood for HADRON. Most tagged photons deposited their energy in the C Counter without interacting in the target because it had to be made relatively short to minimize secondary interactions. Most of the photons which did interact in the target produced e^+e^- pairs and not hadrons. The logical H signal was generated when 30% or more of the energy of the tagged photon was found in the forward calorimeters outside of the SLIC pair plane. TAG·H excluded 99.5% of the e^+e^- pairs.

All the event triggers are described in Table 4 which follows. The last five triggers listed were non-beam triggers taken between beam spills to write calibration information onto the data tape.

TABLE 4. EVENT TRIGGERS

OCTAL NUMBER	DESCRIPTION
1	The DIMUON trigger (USER-1) required the Muon Wall and C2 to find two muons in coincidence with a TAG.
4	The HIGH P_T trigger (USER-3) required a TAG in coincidence with high energy in the sum of the Outriggers and the far east and west sides of the SLIC.
40	TAG·H demanded a TAG with at least 30% of the tagging energy in the forward calorimeters outside of the SLIC pair plane. TAG·H was heavily prescaled.
100	The e^+e^- PAIR trigger required a TAG in coincidence with the SLIC pair plane and a HADRON veto. During normal data taking, an additional coincidence was demanded with SLIC channel U_{37} or U_{76} which, even with heavy prescaling, provided enough events to allow these channels to absolutely calibrate the SLIC on a run by run basis. Both of these channels were two feet away from the middle of the SLIC. This was an optimum distance to minimize rate effects without excessively decreasing e^+e^- energies. During pair calibration runs two 4 foot long plastic

TABLE 4. EVENT TRIGGERS (continued)

OCTAL NUMBER	DESCRIPTION
	scintillation counters, positioned to cover the extreme east and west ends of the SLIC pair plane, were substituted in the logic for U_{37} and U_{76}. These counters allowed shorter calibration runs by equalizing the number of events in different parts of the pair plane.
200	The GAMMA trigger demanded a TAG in coincidence with energy in the C Counter. This was the most copious trigger and it was heavily prescaled.
400	RECOIL 1 required TAG·H and a single recoil proton. RECOIL 1 was prescaled by 33 so as to record fewer low mass states such as the ρ, ω, and ϕ.
1000	RECOIL 2 required TAG·H, a single recoil proton, and a missing mass between 2 and 5.5 GeV/c^2.
2000	RECOIL 3 required TAG·H, a single recoil proton, and a missing mass between 5.5 and 11 GeV/c^2.
4000	RECOIL 4 required TAG·H and 3 or more charged recoil tracks at the most upstream vertex.

TABLE 4. EVENT TRIGGERS (continued)

OCTAL NUMBER	DESCRIPTION
10000	TRIGGER 13 was used for Outrigger, Drift Chamber, and Hadrometer muon calibration runs as well as an e^- and π^- beam trigger.
40001	The UPSTREAM LASER trigger sent N_2 laser light calibration pulses through fiber optic cables to the Recoil Detector phototubes. This laser was located near the Recoil Detector and was used between beam spills.
40004	The DOWNSTREAM LASER 1 trigger sent N_2 laser calibration pulses of light to the Outriggers and Hadrometer between beam spills. This N_2 laser was located on top of the SLIC and it used fiber optic cables to distribute light.
40020	The DOWNSTREAM LASER 2 trigger sent laser light pulses to the SLIC and Cerenkov Counters. The ADC gate timing for this trigger was earlier than 40004. The laser was the same.
40100	The PEDESTAL trigger was used between beam spills to generate ADC pedestals.
40400	The Drift Chamber PULSER trigger sent calibration pulses to the Drift Chambers between beam spills.

K. RECOIL TRIGGER PROCESSOR

The Recoil Trigger Processor (see Figures 35 and 36) was used to select high missing mass TAG·H triggers for recording onto the data tape. It was a very fast data driven processor capable of executing sophisticated instructions such as nested loops, conditional branching, and subroutines. The processor was programmed by connecting various modules, which were capable of executing such functions, and by modifying the memory-look-up data.

The Trigger Processor used fast emitter coupled logic (ECL) circuits and memory-look-up (MLU) devices to reconstruct events in the Recoil Detector in an average time of 7 μsec, about 6000 times faster than a Cyber 175. PWC tracks were reconstructed and matched with end-to-end timing information to find the matching scintillation sector. Pion/proton separation was achieved by comparing energy deposits in the four scintillation layers of the Recoil Detector. When a single proton was found coming from the most upstream hadronic

vertex, a missing mass was calculated based on the tagging energy and the proton 4-vector. This allowed us to preferentially record on tape high mass hadronic states, which were elastically produced with a single recoil proton.

More information on the Trigger Processor may be found in References [40] to [43]. It is pictured on the cover of the May 1983 issue of Physics Today.

IV. TAGGED PHOTON SPECTROMETER FACILITY SOFTWARE

A. ONLINE DATA ACQUISITION SYSTEM

A PDP 11/55 computer with 248 kilobytes of regular memory and 256 kilobytes of bank-switchable bulk memory was used to monitor the experimental data and to record it onto 9 track magnetic tapes. A schematic of the on-line data acquisition system appears in Figure 37. The computer was run under DEC's RSX 11M V3.2 operating system and used Fermilab's MULTI/DA program for on-line histogramming, event displays, and data acquisition.

When prompted by the trigger logic through the Bison Box interface, a stand-alone data acquisition program read the experimental data out of all the CAMAC modules using three Jorway 411 CAMAC branch drivers. During the beam spill the data was stored in the fast bank-switchable bulk memory. It was then transferred to one of two STC 6250 bpi magnetic tape drives between beam spills. Each event written onto tape was identified by a trigger type and logical event number.

A monitoring task generated pedestal, light pulser, and Drift Chamber pulser events between beam spills which were written onto tape and also compared to benchmark values stored on disk. Scalers, such as the number of tags, and readouts, such as magnet currents and Drift Chamber voltages, were also written onto tape and compared to benchmarks. Phototube high voltages were monitored, but not written onto tape. Warning messages were generated whenever any of thousands of quantities being monitored did not match their benchmark values with sufficient accuracy.

The on-line event displays of incoming events allowed us to check the performance of the Drift Chambers and calorimeters.

B. TAGGING RECONSTRUCTION

The main purpose of the tagging reconstruction program was to find the energy of the photon which interacted hadronically in the hydrogen target. In the simplest case, the energy recorded in the lead glass blocks (the first two blocks were really interleaved lead and plastic) was subtracted from the electron beam energy to find ETAG, the tagging energy. More complicated events were also reconstructed.

Pedestals for the 2249 ADC's and gain constants for the lead glass blocks L2 through L13 were read for each run from disk files. The gain constants for the C-Counter, C-East, C-West and L1 were stored as data statements. Data statements were also used to store the energy deposit expected in each lead glass block for the different electron beam energies that we used. The tagging system was essentially self-calibrating, since the average energy that should be seen in each lead glass block was known. The average observed signals were compared to the

expected energy deposits to determine gain constants on a run by run basis.

After getting the calibration constants necessary for a run, the reconstruction began. The 2249 ADC's, which contained the C-Counter, C-East, C-West, and lead glass block information were unpacked. Pedestals were subtracted and the resulting values were translated into GeV with the gain constants. The latch bits were also unpacked so that the Hodoscope and Anti-Counter (see Figure 9) information would be available.

Electrons were searched for in the hodoscope counters and in the corresponding lead glass blocks. About 70% of the events have single electron showers. The shower energy found was compared to the momentum expected, given the magnetic field of the tagging magnet and the position of the lead glass block. Single electrons were allowed to share adjacent blocks and hodoscope elements, if geometrically possible. If two showers were found and the positron Anti-Counter (A10) bit was off, it was assumed that there were two interacting

electrons in one RF bucket; the beam energy was doubled in subsequent calculations to correct for this. If two showers were found and and the positron Anti-Counter bit was on, it was assumed that there was a single electron in the RF bucket and that one of the bremsstrahlung photons pair produced. The beam energy was left alone in this case.

At this point the total energy of all the bremsstrahlung photons hitting the hydrogen target was known. It remained to find the energy of the photon which interacted hadronically and caused the event trigger to fire. Bremsstrahlung photons which pass through the target shower in the C-Counter. This energy was subtracted from the total energy of all photons entering TPL. If a photon produced an e^+e^- pair in the hydrogen target, most or all of the energy would be deposited in C-East, C-West, or the C-Counter itself. Again this energy was subtracted. Studies have shown that one-fourth of the energy deposited by a photon in the C-Counter from the RF bucket immediately preceding the event was picked up

by the C-Counter ADC. A second ADC was used to record this energy so that one-fourth of it can be subtracted from the C-Counter energy before the C-Counter energy was subtracted from ETAG.

After saying all this, I should point out that a single energetic bremsstrahlung photon was the most usual occurrence. But regardless of the event complexity, whenever the 2249 ADC and latch bit data was present, the tagging energy was calculated as well as an error on ETAG. Bits were set in the flag word, JTGFLG, for the various conditions found during the tagging reconstruction.

C. RECOIL RECONSTRUCTION

Three data types had to be present to reconstruct recoil tracks. First, the 2280A ADC pulse heights were needed to find the energy deposits in each of the four scintillator layers, which were labeled from "A" on the inside to "D" on the outside of the Recoil Detector. Pedestals were subtracted from the 2280A ADC's and then energy deposits were found by taking the product of the pedestal-subtracted pulse heights and gain constants stored on disk. Second, PWC cathode hits were needed to make θ measurements and to correct the energy deposits in the scintillator for attenuation. Third, the End-to-End Timing (EET) measurements were needed to correlate PWC tracks with energy deposits in the scintillator layers. Each of the 15 EET values was converted to a Z position using two calibration constants, "a" and "b", stored on disk and the formula $z = a + b$ EET.

Two additional data types were very helpful but not absolutely essential. PWC anode hits allowed ϕ

measurements to an accuracy of ±1.26° instead of the ±11.05° provided by the the scintillator layers, which were divided into 15 φ sectors. Time of Flight (TOF) TDC values allowed the identification of slow electrons, pions, and protons. The TOF values were combined with the TAG time, the vertex determined by cathode tracks and beam axis, and the energy deposit in the "A" layer of the scintillator, where these slow particles range out. The TOF system had a resolution of one nanosecond and the slow pions and protons, which range out in the "A" layer, were separated by several nanoseconds.

PWC cathode hits and cluster widths were found and converted to z values. A hit array was filled for the middle PWC. Next, all pairs of hits for the inner and outer PWC's were considered to see if there was a matching hit in the middle PWC array. The cluster widths of all three chambers were used to set the θ and z errors of tracks. Finally, tracks were matched to sector windows, determined by end-to-end timing. At most, the best three matches were saved.

Now 2-point cathode tracks were searched for. At least one of the hits must not have been used in a 3-point track. To provide some further redundancy, at least one EET window has to agree with 2-point tracks and at least one 3-point track has to intersect the target near the place where the 2-point track intersected the target.

Three-point and two-point anode (ϕ) tracks were found in much the same manner, except that both hits of a two-point track cannot have been used before.

With these preliminary calculations out of the way, the real work of matching PWC tracks to energy deposits in the scintillator and separating pions from protons began. Cathode tracks were ordered by increasing z; this was useful later in defining the most upstream interaction.

Then, a loop was made over all sectors with EET windows and all PWC cathode tracks. For each track-sector combination, both proton and pion mass hypotheses, penetrating and stopping trajectory hypotheses, inclusion and deletion of the outermost layers, and various kinetic energies were tried to

get the best x^2 fit. Saturation corrections for the stopping hypothesis and attenuation corrections were made to each sector energy. The number of degrees of freedom (NDOF) in the fit were equal to the number of layers included minus one. The x^2 was defined as

$$x^2 = \sum_i [(E_i - X_i)/\sigma_i]^2/NDOF \ ,$$

where the index i was over all included layers, E_i was the energy deposit observed, X_i was the predicted energy deposit, and σ_i was the error on E_i. The variable, X_i, was a function of whether the particle stops or penetrates a layer, the particle type, polar angle θ, and the particle kinetic energy. This information was combined with Bethe-Bloch predictions to yield X_i. For each hypotheses, the expression $dx^2/d(KE) = 0$ was solved to find the kinetic energy which minimizes the x^2. The solution of this equation, which was done numerically, consumes most of the computer time in the recoil analysis.

The final set of recoil 4-vectors was subject to

the constraints that no track or sector may be used more than once and that as many tracks and sectors as possible must be used. If more than one set of matches between tracks and sectors satisfied these criteria, the set with the lowest total χ^2 was chosen.

D. DRIFT CHAMBER RECONSTRUCTION

The Exhaustive Search Track Reconstruction (ESTR) program was used to turn Drift Chamber TDC times into reconstructed charged tracks. With an average of six tracks per event, the Drift Chambers posed a difficult reconstruction problem which had to be solved with a limited amount of computer time and memory. First the TDC times of hits were transformed into U, V, and X coordinates using various calibration algorithms. The distance from a hit to a Drift Chamber sense wire was now known but whether the track passed on the left or right side of a sense wire remained ambiguous. Then, track segments were found in the separate groups of Drift Chamber planes. The array JCATSG was used to store track categories. The first four bits of JCATSG were used to tell which of the four Drift Chamber groups contributed to a track. For example only D1 and D2 would contribute to a category 3 track. The fifth bit was used to mark spurious tracks. (Figure 19 shows a layout of the Drift Chambers and

analyzing magnets.)

We began looking for track segments in D3 because tracks reaching it had been spread by both analyzing magnets and because D3 had the fewest spurious hits. All UVX triplets in each of D3's three modules were first found. A UVX triplet consisted of one hit on each of the U, V, and X wire planes contained in each module. The third hit had to be consistent with the physical location in space predicted by the first two. Then three dimensional line segments were constructed in D3 whenever 4 to 6 more hits (other UVX triplets were tried first) could be matched to a UVX triplet with loose cuts. Thus at least 7 out of 9 possible hits were required. Line segments were required to point towards the target in the vertical Y coordinate. Because the magnets deflected the tracks horizontally, the X coordinate was uncertain at this stage. Physical tracks often generated several nearly duplicate line segments.

Next the D3 line segments were projected through M2 into D2. If any of the UVX triplets in D2 matched a D3 line segment projection in the Y

coordinate, which was momentum independent, a quick calculation was performed to see if the D2 X coordinate of this combination was consistent with a track coming from the hydrogen target. A box field approximation was used for the magnets in this calculation. If at least 3 more hits were found in D2 in addition to the UVX triplet, this D2-D3 combination was stored as a track candidate. The process was repeated until all possible track candidates, including close duplicates, had been found. The requirement that D2-D3 line segments point to the target did eliminate some real tracks which were unrelated to photoproduction such as muons from the primary proton target.

The D2-D3 track candidates were then projected upstream into D1 and downstream into D4. At least 3 out of 8 possible hits were required to add D1 to the D2-D3 track candidate. Two out of three possible hits were required to add D4. D4 was rather noisy due to splashback from the C Counter and SLIC, large cross section for stray muons, and its relatively long drift time. If all four Drift

Chamber groups contributed to a track it was defined as a category (JCATSG) 15 track.

The next step was to group the track candidates into bundles of tracks with each bundle corresponding to a "real" track. The best track was then chosen out of a bundle which typically contained 20 candidates due to crosstalk, right-left ambiguities, primary target muons, and particles from other events inside the TDC gate. The choice was based on the number of hits contributing to each candidate, the χ^2 of line segments in D2 and D3, the match in the center of M2, and the quality of hits. D4 hits were weighted lower than D3 hits. The end result of this process was a list of real category 7, 14, and 15 tracks. Category 7 tracks (D1-D2-D3) either missed D4 or could not be matched to hits in D4. Similarly category 14 tracks (D2-D3-D4) might not have appeared above the noise in D1 or might have been tracks from Λ's or K^0_S's which decayed too far downstream to be found in D1. Category 15 (D1-D2-D3-D4) tracks were the most useful kind for finding D mesons. An efficient bookeeping system,

employing pointers to identify track candidates, was used throughout ESTR to minimize the computer time and memory space required.

At this stage, we searched for Category 3 tracks (D1-D2). The search was complicated by the magnetic bending of D1 track segments. First, we looked for all three dimensional line segments in D2, which had at least one UVX triplet not connected to an accepted category 7, 14, or 15 track. Just as in D3, seven out of nine possible hits were required to form a line segment. A UVX triplet was considered to have been used if any of the other physically nearby UVX triplets created by left-right ambiguities were used. The D2 segments were then projected into D1. All D1 X hits were combined with each D2 line segment, and a calculation was made, using a rough approximation of the M1 magnetic field, to see if this combination pointed to a position less than 20 cm away from the center of the target. If the combination came from the target and 3 out of 8 possible D1 hits could be found, pointers for this D1-D2 combination were stored on

a candidate list. When all these category 3 candidates were found, they were grouped into bundles just as in the case of category 15 candidates. The "physical" track was then picked out of each bundle with a heavy emphasis being placed on each candidate's number of hits. As a failsafe measure, D2 segments were projected back into D3. Once every hundred events or so a connection was made in this manner; the cuts going upstream and downstream were not exactly symmetrical. Also, sometimes the candidate arrays reached their limits and caused missing connections. Finally, we searched for category 28 tracks (D3-D4). Leftover D3 segments were projected into D4 and linked up if at least two out of three possible hits were found. These candidates were then grouped into bundles of tracks and the best track was picked out of each bundle. These tracks were labelled category 28 (D3-D4 plus the spurious fifth bit on). Occasionally very good segments in D3 with all 9 hits were labeled category 28 even if they could not be matched up in D4.

All the tracks found up to this point, except the category 28 tracks, were used to determine the primary vertex of the event in the target. The track trajectories through the magnetic fields were accurately calculated [23] to determine their momenta and the vertex. This vertex was used to find D1 only tracks (category 1). The first demand on D1 only tracks was that they be 20 cm away from the center of D1 in X and 10 cm away in Y. This wide angle cut eliminated the hopelessly congested central region of D1. Because the X' planes only covered the middle of D1 they did not contribute very much to category 1 tracks. Five hits that pointed to the vertex were demanded for these tracks. A crude estimate of momenta was made and candidates with momenta below 200 MeV/c were excluded. Again the best candidates were chosen out of bundles.

Finally, a cleanup phase was entered to tag spurious tracks. This usually changed a few category 3 tracks (D1-D2) into category 19 tracks (spurious D1-D2). All the tracks were ordered based

on how many hits they shared with other tracks. (A single hit could be used repeatedly.) If a track consisted mostly of hits used by tracks which did not share very many hits with other tracks, the fifth bit in JCATSG was set on, labeling the track as spurious. The final output arrays provided for the storage of a maximum of 20 tracks with fitted parameters and hits for up to 30 tracks. In the rare cases when more than 20 final tracks were found the fitted parameter list was arbitrarily cut off at twenty. Nevertheless, category 15, 14, and 7 tracks tended to be kept, because they were stored at the top of the list.

We had to contend with numerous false hits. The TDC window was 300 ns wide for the first 3 Drift Chambers and 500 ns wide for D4. The beam flux was such that out-of-time e^+e^- events could enter these windows. Primary target muons and crosstalk also caused many false hits. This all added to the problem of left-right ambiguity. Thus it was imperative to have a program that was able to make lists of all possibilities quickly, using a small

amount of computer memory, and then pick the best tracks using the maximum available information. Numerous early tests of track candidates can prove as time consuming as one final test, while being forced to make decisions based on less information. The track projection algorithms were straight forward. The bookeeping and the pointer schemes were the crucial elements of the ESTR Exhaustive Search Track Reconstruction program.

E. VERTEX RECONSTRUCTION

Recoil and Drift Chamber tracks were used to find the primary vertex of each event, as well as neutral secondary vertices from $\gamma \to e^+e^-$ conversions and $K^0_S \to \pi^+\pi^-$ and $\Lambda \to p\pi^-$ decays.

The first step was to group the Recoil tracks into sets coming from the same place in the target. In the simplest non-trivial case one Recoil track determined one Recoil vertex, given the location of the photon beam. Next, forward tracks were matched with the most upstream recoil vertex. If no forward tracks were close, and a more downstream recoil vertex existed, a search was made to see if any forward tracks were close to it. When a primary vertex was found, its optimum location, with errors, was chosen to minimize the weighted sum of the squares of the distance of closest approach of each track associated with it. To weight the least squares fit, the unit vector momentum components of each track were assigned errors, σ_x, σ_y, and σ_z. The use of three separate errors was very helpful,

particularly in finding Z positions. The errors depended on whether the track was seen in the Recoil Detector or the Drift Chambers, the angle of Recoil tracks with respect to the beam line, the track momentum, and how many magnets the track passed through. For a typical primary vertex, the average position error was 0.2 mm in X and Y and 4 mm in Z.

Finally a search for two-prong neutral secondary vertices was performed downstream of the primary vertex. Pairs of positive and negative particles were required to pass several tests if their distance of closest approach was small. At least one of these two particles could not point to the primary vertex. The 3-vector constructed out of these two particles must point to the primary vertex. The primary and secondary vertices had to be significantly separated, and no more than two tracks could come from the secondary vertex. The final requirement was that the mass of the two tracks be consistent with either $\gamma \rightarrow e^+e^-$, $K^0_S \rightarrow \pi^+\pi^-$, or $\Lambda \rightarrow p\pi^-$.

F. CERENKOV RECONSTRUCTION

The two Cerenkov counters allowed us to partially distinguish between five possible mass hypotheses; electron, muon, pion, kaon, and proton.

First, the trajectories of the charged tracks were used to calculate how much light would fall on each Cerenkov mirror, for each of the five mass hypotheses. Track trajectories inside each Cerenkov counter were each divided into steps (12 in C1, 10 in C2) and the average number of photons contributed to each mirror by each step for each mass hypothesis was calculated. Whenever a track was outside a Cerenkov counter or inside the pair plane shields in C2, radiation was not allowed to reach the mirrors. The light from each step appeared as a slightly elliptical annulus at the mirror plane of each Cerenkov counter. The mean number of photoelectrons from each mirror-phototube combination was adjusted for the real individual channel efficiencies.

At the end of this first Cerenkov pass, we decided to use parallel programs by Gerd Hartner and

Jim Elliott to calculate particle type probabilities. I will start by discussing Jim Elliott's program.

Electron identification by the SLIC and muon identification by the Hadrometer and Muon Wall were used to eliminate certain mass hypotheses. The mass hypotheses of tracks were then raised (to higher masses) in various combinations until further increases would lead to mirrors with unexplained light. At this point mirrors sharing light from more than one track were eliminated from consideration. The light predictions for the remaining mirrors were then summed for each track to form predicted mean numbers of photoelectrons for the mass hypotheses. The number of photoelectrons observed from the summed mirrors was compared to a Poisson like probability distribution generated from the predicted mean of the summed mirrors. This gave a consistency probability; that is a probability that a particle of a hypothesized mass would lead to the observed light.

Now consider Gerd Hartner's program. First, the tracks were grouped into possibly coupled subsets by assuming that each track was an electron and seeing if mirrors were shared. (Electrons produce the largest Cerenkov light cones.) Sometimes common mirrors were discarded to make the subsets smaller. Next, all combinations of mass hypotheses were tested in each subset to see which best explained the light observed on the Cerenkov mirrors. A two track subset would, for example, have 25 combinations (five hypotheses for the first track times five hypotheses for the second track). The number of combinations was reduced when two or more mass hypotheses all produced no light in one or both Cerenkov Counters. Electron identification from the SLIC and muon identificaton from the Muon Wall and the Hadrometer were next used to weight or exclude possibilities. The most important effect of the lepton identification was to exclude the large electron light cones and hence decrease the number of tracks in subsets. The end result of this program was a consistency probability, that a

particle of a hypothesized mass would lead to the observed light.

The final probability for each track's five possible masses was found by taking the product of the consistency probability and an a priori probability for each particle type. The electron, muon, pion, kaon, and proton a priori probabilities were 0.12, 0.08, 0.65, 0.11, and 0.04, respectively. This technique follows from Bayes's theorem [44].

G. OUTRIGGER AND SLIC ALGORITHMS

The Outrigger and SLIC programs were used to reconstruct photons and, from the photons, π^0's. We also used the programs to distinguish electrons from hadrons by comparing drift chamber determined momenta to calorimeter energy deposits. The Outrigger and SLIC algorithms were virtually identical, up to the point where energy deposits seen in the separate views were put together to yield particle 3-momenta.

The programs combined the one dimensional views of the calorimeters together to find the X and Y positions of particles, as well as their energies. Several problems had to be addressed. Large showers often formed smaller satellite showers, which were hard to distinguish from real particles. This problem was particularly acute for the wide hadronic showers in the SLIC. A typical event contained eleven particles, and it was extremely common for two physically separated particles to overlap in a particular view. Figure 38 shows a simple example

of this sort of ambiguity in the SLIC. Particles E_1 and E_3 must be real, but either E_2 or E_4 may be phantoms. Muons from the the primary proton target appeared as 1/2 GeV equivalent showers. The muon problem was compounded by their lack of Drift Chamber tracking, higher energy deposits from the Landau tail, and the use of scintillator for the Y counter Outrigger light guides. And finally, due to finite detector resolution and calibration errors, the energy measurements in the different views do not exactly match. The algorithms outlined below address these problems. Hadronic satellite showers in the SLIC and particles which overlapped in the one dimensional views were the most serious problems. The reconstruction of the SLIC was quite difficult, while the Outrigger reconstruction was quite a bit simpler due to fewer particles.

First, the 2280B ADC's were unpacked and pedestals were subtracted from the raw ADC values. Because the pedestals drifted significantly during data runs, they were updated during the analysis whenever 10 of the pedestal events, written between

beam spills, were read and averaged. Initial pedestals were determined by delaying the analysis until ten pedestal events had been read from a data tape, and then rewinding the tape to begin analyzing beam events.

The pedestal-subtracted pulse heights were multiplied by gain factors to convert them into GeV. Gains drifted to a small extent, and our calibration procedures were designed to correct these drifts. The gain factors were stored in data statements within the body of the Fortran code. In the case of the SLIC, the gain factors were based on e^+e^- and muon calibration runs, as well as adjustments from the requirement that particles must, on the average, deposit the same energy in all three views of the SLIC. This master set of gain factors was updated on a run by run basis with light pulser disk files. The light pulser was normalized to the sum of "stable" counters, a large subset of all SLIC counters. Eight sets of Outrigger gains were stored as data statements. Each set represented an Outrigger muon calibration run taken during the six

month data run. The set of gains closest to a data run was selected to transform the Outrigger pulse heights into GeV.

With the calibration process complete, each electromagnetic calorimeter view was divided into cells. A cell was defined as a contiguous group of counters above an energy threshold. Counters below the energy threshold formed boundaries. A cell was subdivided into sectors, if more than one counter in a cell contained an energy signal with more significance than its two nearest neighbors. Cells could also become single sectors. The majority of sectors corresponded to single particles. Array space was provided for a total of 80 sectors in the SLIC and Outriggers. For a sector to be formed, its central counter also had to pass an energy significance cut, which was lowered if a Drift Chamber track landed closer than one counter width. A record was kept of which sector a charged track landed in. If the track landed between two sectors, both of them were associated with the track. Sometimes, small candidate sectors were rejected if

they were close to a sector with a lot more energy. These were typically satellites of hadronic showers.

The center of gravity of each sector was determined from three counters. This position was then adjusted for the known transverse shape of electromagnetic showers to yield sector locations. Next, a stepwise regression fit [45,46] was used to find which of the candidate sectors were significant and how to divide the total cell energy among the significant sectors. The transverse energy distribution of each sector was fit to an electromagnetic shower shape plus a broader version of this shape used to approximate hadronic showers. Fitting to a linear combination of a wide and narrow shower shape had much the same effect as varying the widths of showers, while providing the computational advantage of keeping the fit linear. More weight was given to a counter if it had more photoelectrons per unit energy, if its 10 event pedestal width was small, if the detector in question had better shower statistics, if a charged track was within one counter width of it, or if it contained more energy.

This fit is mathematically very similar to the one described later, which combines the U, V, and Y SLIC sectors to form particles.

After the fit, each sector energy error (σ) and weight (w) was calculated. ($w = 1/\sigma^2$.) The errors depended on shower statistics, photoelectron statistics, whether the incident particle was thought to be electromagnetic or hadronic, and the energy deposited.

At this point the Outrigger and SLIC reconstruction programs diverged. In the Outriggers, charged track information was used to remove sectors from consideration as possible contributors to photons. All possible XY combinations of sectors were then considered to see which set of combinations did the best job of matching Outrigger X and Y sector energies. Because the positions of candidate particles were known, an optical attenuation correction was applied. Only sets of XY combinations with the minimum number of photons needed to explain the presence of all the sectors were considered. Therefore, the number of

photons was equal to the number of sectors in the view with the most sectors. A maximum of five sectors per view was allowed. It was rare for more than two photons to hit one of the Outriggers.

Now consider the SLIC, which presented a far more complex reconstruction problem than the Outriggers. A candidate list of particles was made of all UVY sector triplets whose V and Y sector positions predicted the U sector position. If the same charged particle could be in all three sectors, the required accuracy of this prediction was decreased because charged tracks were almost always real. We used stepwise multiple regression [45,46], a linear least squares fitting technique, to find the best set of candidate particles along with their energies and energy errors.

The first goal was to find a formula to relate how well any particular choice of candidate particle energies matched the observed sector energies. Let e_i be the energy measured in sector i, with weight w_i. Let ε_j be the energy which candidate particle j deposited in the SLIC. Let α_{ij}

be an energy correction factor which depends on the known position of the candidate. This includes an optical attenuation factor and corrections for physical and optical shower leakage between the right and left Y views. If sector i does not contribute to candidate j, then $\alpha_{ij} = 0$. With this framework in hand, the x^2 for any given choice of candidate energies is:

$$x^2 = \sum_i (e_i - \sum_j \alpha_{ij}\varepsilon_j)^2 w_i \ .$$

This x^2 was minimized by setting its derivative with respect to the candidate energies equal to zero.

$$\partial x^2/\partial \varepsilon_K = 0 = 2\sum_i w_i (e_i - \sum_j \alpha_{ij}\varepsilon_j)\alpha_{iK} = 2(S_K - \sum_j C_{jK}\varepsilon_j)$$

where $S_K = \sum_i w_i e_i \alpha_{iK}$ and $C_{jK} = \sum_i w_i \alpha_{ij}\alpha_{iK}$

One could just invert the correlation matrix C to solve for the candidate energies.

$$\varepsilon_j = \sum_k C^{-1}_{jK} S_K$$

But, even for a simple 12 candidate event, over four thousand matrix inversions would have to be

performed to find the optimal combination of candidates. Futhermore, in cases with more candidates than sectors, the matrices can't be inverted.

Instead, candidates were added to and subtracted from the fit one at a time. Hence, the name stepwise regression. This may be done without having to invert the entire correlation matrix for each step. For N candidates, only 1/N times as many calculations were required for each step.

A sweep operator, described by Jennrich [45], was used to add candidates to the fit. For convenience, the sector energy vector S was added to the correlation matrix C to form an additional row and column in a new square matrix A. The diagonal elements of A were preserved in a vector D for future use, since the sweep operator changes the elements of A. The size of A was equal to the number of candidates plus one, and was not changed by the sweep operator.

$$A = \begin{pmatrix} C & S \\ S & B \end{pmatrix} \qquad \text{where } B = \sum_i w_i e_i e_i$$

We exploited the symmetry of A by storing it as a triangular matrix. This reduced the array space needed to store 80 candidates, the maximum allowed, from 6561 to 3321. The sweep operator to add candidate k to the fit performed the following operations to update A.

$$\bar{A}_{kk} = -1/A_{kk}$$

$$\bar{A}_{ik} = A_{ik}/A_{kk} \qquad \text{where } i \neq k$$

$$\bar{A}_{kj} = A_{kj}/A_{kk} \qquad \text{where } j \neq k$$

$$\bar{A}_{ij} = A_{ij} - \sum_k A_{ik}A_{kj}/A_{kk} \qquad \text{where } i \neq k \text{ and } j \neq k$$

The inverse sweep operator, used to remove candidate k from the fit, performed the following operations.

$$\bar{A}_{kk} = -1/A_{kk}$$

$$\bar{A}_{ik} = -A_{ik}/A_{kk} \qquad \text{where } i \neq k$$

$$\bar{A}_{kj} = -A_{kj}/A_{kk} \qquad \text{where } j \neq k$$

$$\bar{A}_{ij} = A_{ij} - \sum_k A_{ik}A_{kj}/A_{kk} \qquad \text{where } i \neq k \text{ and } j \neq k$$

Because any given pair of candidates i and j were usually uncorrelated, the sums involved in both the

sweep operator and its inverse could usually be skipped to save computer time.

At each stage, the matrix A contained quantities which guided the stepping. In particular, the F test was used to tell when a candidate energy was significantly different from zero. I will define six generally useful quantities first.

N = number of candidates
m = N + 1 = size of matrix A
NSECT = number of sectors
VARIN = Number of Candidates in the Fit
DOF = Degrees of Freedom = NSECT - VARIN - 1
$\chi^2 = A_{mm}$

The energies, energy errors, and F tests of candidates, which had been brought into the fit, were as follows.

$ENERGY = A_{im}$

$ERROR = (-A_{ii}\chi^2/DOF)^{1/2}$

$FTEST = (ENERGY/ERROR)^2$

The energies and F tests which candidates would have had if brought into the fit, as well as the tolerance of the fit for their entry, were as

follows.

$$ENERGY = A_{im}/A_{ii}$$

$$FTEST = \frac{[DOF-1.][A_{im}/(\chi^2 A_{ii})]}{1. - [A_{im}/(\chi^2 A_{ii})]}$$

$$TOL = \text{Tolerance} = A_{ii}/D_i$$

We used several criteria to tell when to add and subtract candidates. First, no candidate was added to the fit if it was a close linear combination of candidates already in the fit, i.e. a tolerance test had to be passed (TOL > 0.1). Next, candidates associated most closely in space with charged tracks were added, because it was almost certain that these candidates were real. Futhermore, these candidates could not be removed unless another candidate associated with the track in question had been brought into the fit. With the charged tracks mostly out of the way, we started looking for the photons. The candidate with the highest FTEST was brought in first, and then less significant candidates, until a F test cut of 20.0 was reached.

The cut was lowered to 5.0 for candidates which had at least one unique sector; that is at least one sector which was not used by a candidate already in the fit. The majority of candidates had at least one unique sector. Photons which would have negative energies were not brought into the fit. As more candidates were brought in with the sweep operator, the energies and FTEST's of the previously entered candidates changed. If the FTEST of one of these previously entered candidates fell below 4.0, it was removed with the inverse sweep operator. The F test cut (4.0) to remove candidates was made lower than the F test cut (5.0) to enter candidates, to help avoid repeatedly entering and removing a pathological series of candidates. Photons whose energies became negative were also removed. When no more candidates remained to be added to the fit or subtracted from the fit, the photon finding was complete.

At this point, π^0's were reconstructed from SLIC and Outrigger photons. Particles not associated with charged tracks and not matched to neutrals in

the Hadrometer were called photons. Also, at this stage non pair plane e^+e^- pairs, which usually come from interactions of π^0 photons in the target, were recombined into photons. Energy cuts were used to eliminate untracked muons and satellite showers masquerading as photons. A large majority of these low energy particles were hadronic shower satellites in the SLIC. A minimum photon energy cut of 2 GeV (1.6 GeV for low energy error photons) was used in the SLIC. A cut of 1 GeV was used for Outrigger photons.

The π^0 reconstruction algorithm began by combining all pairs of photons above the energy cuts and calculating the mass of each combination. For each combination, the agreement between the $\gamma\gamma$ mass and the π^0 mass was parameterized with the number $\chi^2 = [(M^2_{\gamma\gamma} - M^2_{\pi^0}) / \delta M^2]^2$, where δM^2 is the error on the $\gamma\gamma$ mass squared. The quantity, δM^2, depends on the photon energy errors and the opening angle error, which was insignificant for all except the highest energy π^0's. The χ^2 provided the likelihood that the difference between the $\gamma\gamma$ mass and the π^0

mass was consistent with the photon 4-momenta errors. To facilitate the transformation of each χ^2 into a probability that the photons came from a π^0, photon pairs were divided into four categories based on the origin of their photons. The four categories are SLIC-SLIC, SLIC-Outrigger, Outrigger-Outrigger, and SLIC-Pair. Figures 39 through 42 show mass plots of these four types of π^0's from a typical 15000 event 170 GeV tape segment. All "unique" photon pairs are included. If neither photon formed a π^0 with any other photon in the event using a liberal χ^2 cut, the photon pair was defined as "unique" and included in the plot. (Most π^0's which we accepted were unique.) Plots like these were used to calculate the amount of background and signal for any given $\gamma\gamma$ mass in each of the four π^0 categories. Each plot was fit to a gaussian signal shape on a flat background. SLIC-SLIC plots were also subdivided according to the π^0 energy. A probability, PRPIZ, was calculated for each π^0 candidate based on the $\gamma\gamma$ mass, χ^2, and the background underneath the appropriate π^0 peak.

A second probability, PRPIZ2, was calculated whenever one or both photons in one π^0 could be used in another π^0 with a probability greater than 5%. PRPIZ2 was used to recognize that a single photon cannot come from more than one π^0 and was an appropriate adjustment of PRPIZ.

Two final adjustments were made in the π^0 reconstruction. In calculating a π^0 4-momentum, the energies of both photons were adjusted to make the $\gamma\gamma$ mass equal to the π^0 mass, which is 134.96 MeV/c^2. The accuracy of PRPIZ2 was studied by looking at our very strong $\omega \rightarrow \pi^+\pi^-\pi^0$ signal. From this study of the ω signal and background a more refined probability, PIZPRB, was determined. An ω plot for PRPIZ2 > 0.9 appears in Figure 43. See Table 5 for the function which generated the final π^0 probability, PIZPRB, from PRPIZ2.

In summary, shower energies were used like an extra view to correctly combine the physical views of the electromagnetic calorimeters together to find photons, and other particles. The problems of hadronic satellites, finite detector resolution,

calibration errors, showers which overlapped in the one dimensional views, and limited computer time were dealt with. The efficiency of these programs for detecting π^0's in D^0 meson decays is discussed in the π^0 Monte Carlo section.

TABLE 5. π^0 PROBABILITIES FROM $\omega \to \pi^+\pi^-\pi^0$ DECAYS

PRPIZ2 (OLD)		PIZPRB (NEW)
0.00	→ 0.05	0.0028
0.05	→ 0.10	0.0085
0.10	→ 0.15	0.0142
0.15	→ 0.20	0.0199
0.20	→ 0.25	0.0256
0.25	→ 0.30	0.0313
0.30	→ 0.35	0.0369
0.35	→ 0.40	0.0426
0.40	→ 0.45	0.0483
0.45	→ 0.50	0.0540
0.50	→ 0.55	0.0596
0.55	→ 0.60	0.0758
0.60	→ 0.65	0.0909
0.65	→ 0.70	0.1212
0.70	→ 0.75	0.182
0.75	→ 0.80	0.227
0.80	→ 0.8375	0.379
0.8375	→ 0.8625	0.51
0.85	→ 0.8875	0.667
0.8875	→ 0.9125	0.84
0.9125	→ 0.95	0.92
0.95	→ 1.00	0.99

H. HADROMETER RECONSTRUCTION

The Hadrometer reconstruction program was used to match energy deposits in the Hadrometer to charged particles found in the Drift Chambers and then, after subtracting these deposits out, to find neutral hadrons.

The first step was to make a list of all "bumps" found in the upstream and downstream halves of the Hadrometer and in the sum of these halves. As may be recalled from the Hadrometer hardware section, each upstream and downstream half of the Hadrometer has right and left Y views and one X view. A "bump" is defined as as a counter in a view with a pulse height significantly greater than its neighbors.

The position of each charged track was projected to the Hadrometer to see if an XY pair of bumps could be associated with it. If the association was successful, an average hadronic shower shape was used to subtract out the charged particle. The energy subtracted was that provided by the Drift Chambers and corrected for the energy deposited in

the SLIC. The energy subtracted was constrained not to exceed that appearing in the Hadrometer. Also, because the position was known, a correction was made for the attenuation of the scintillator light as a function of the distance to photomultiplier tubes.

After the subtraction process was complete a search for significant bumps was made in the sum of the upstream and downstream halves of the Hadrometer. These X and Y neutral bumps were matched together according to their energies. Again corrections were made to the energies for attenuation. Provision was made to find a maximum of two neutral hadrons on each side of the Hadrometer.

Neutral hadrons from this reconstruction program have been successfully used to find the signal $\phi \rightarrow K^0_S K^0_L$ (see Figure 44).

I. MUON IDENTIFICATION

Charged tracks were identified as muons by the Hadrometer and Muon Wall. The muon identification program did not distinguish between muons from the primary vertex and muons created by pions and kaons decaying in flight. The output of the muon routines was a definitive yes or no rather than a probability.

The definition of a muon was determined from a study of 130 $\psi \rightarrow \mu^+\mu^-$ decays [22,47]. A muon counter which could have been hit by a projected track must have had a TDC time consistent with the vertical position of the track. The muon counter latch bit was not used as it proved to be less reliable than the TDC time. The track must have deposited between 1 and 5.5 GeV in either the X or Y view of the Hadrometer. A minimum ionizing track typically left 2.4 GeV in the Hadrometer. The width of the energy deposit in the Hadrometer must have been less than 10" in Y or 12" in X. The ratio of the energy seen in the front half of the Hadrometer for the muon candidate to its total Hadrometer energy must have

been between 0.16 and 0.87 in either the X or the Y view.

These cuts were based on the ψ study (95% of the ψ muons passed the cuts). Studies of non-dimuon triggers showed that a few per cent of the particles identified as muons were really hadrons. Muons with energies below a few GeV ranged out before they reached the Muon Wall. About 5% of the non-dimuon trigger events had a muon, which was about the number expected from pions and kaons decaying in flight.

Neutral particles found in the Hadrometer were identified as untracked muons if the energy they deposited was between 1.6 and 3.7 GeV and two of the following three conditions were satisfied. The ratio of the energy seen in the front half of the Hadrometer to total energy was between 0.2 and 0.8 in the X and/or Y views. The particle was located more than one meter east of the middle of the Hadrometer where a high flux of muons from the primary proton target existed. Most untracked muons originated in the primary proton target.

V. DATA RUNS

A. EVENT PRODUCTION

Data taking commenced in December 1980 and was completed on 1 June 1981 when the Proton Beam Line caught fire. Radiation prevented the fire from being immediately extinguished, so we lost the last six hours of our run.

The energy of the beam was 137 GeV during the first four months of the run and 170 GeV during the final two months. We used one thousand 6250 byte per inch magnetic data tapes to record 12.1 million 137 GeV and 4.87 million 170 GeV Recoil 2 and 3 triggers. At about the same time as the beam energy increase, two other changes were made to the spectrometer. Muon counters were added to increase the acceptance of the dimuon trigger for asymmetrical ψ decays. Masks were added to the seventh and eighth layers of the Outrigger X views to improve resolution. Soon after beginning 170 GeV data taking, some Drift Chamber thresholds were increased to reduce the number of false hits.

B. EVENT RECONSTRUCTION

The first step of the event reconstruction was concurrent with the event production. Each tape generated at the Tagged Photon Lab was run through a monitor program on one of the three Fermilab Cyber 175 computers. The purpose of the monitor program was to insure that all the individual Drift Chamber, Calorimeter and other detector channels were producing data signals. It also used scaler, pedestal, light pulser, and Drift Chamber pulser events to make calibration disk files. No reconstruction was done at this time because the programs were not ready.

Actual reconstruction commenced in December 1981 and was essentially completed in June 1983. The reconstruction programs were divided into two passes.

The Drift Chamber and Recoil Detector reconstruction were unique to Pass 1. Because the Pass 1 programs exceeded the 304000_8 60-bit words available to users on the Fermilab Cyber 175

computers, a segmented load was used in which each subroutine and common block had to be explicitly moved in and out of core during program execution. Typically, Pass 1 required 1/2 second of Cyber 175 CPU time per event. To decrease the number of years necessary to analyze this experiment, the Pass 1 code was also converted to run on two other computer systems: an IBM 3033N in Ottawa and six IBM 370/168 emulators built with AMD 2902 bit slice chips by our colleagues at the University of Toronto.

The final version of the Pass 2 reconstruction program analyzed the Tagging System, Cerenkov Counters, Outriggers, SLIC, Hadrometer, and Muon Wall. Pass 2 was run with a segmented load on the Fermilab Cyber 175 computers and also on VAX 11/780 computers, equipped with floating point accelerators, at UCSB and the University of Colorado. The Pass 2 Fortran code was written to minimize the differences between Cyber Fortran 4 and VAX Fortran. On several occasions, new versions of Pass 2 were brought up on the Cyber and were then transfered to and executed on a VAX in a matter of

hours. The final Pass 2 programs typically required 1/6 second of Cyber CPU time to reconstruct an event. This represented a 30% speed improvement over the original Pass 2. This optimization made use of the Fermilab HOTSPOT program, which recorded how long each line of the Pass 2 code spent in execution. HOTSPOT allowed us to concentrate on improving the most time consuming sections. Pass 2 ran 6.7 times faster on a Cyber 175 than on a VAX 11/780. Table 6 tells how much Cyber 175 time each part of the Pass 2 consumed analyzing events.

Particle four-vectors, four-vector errors, and particle identification were then extracted from the Pass 2 output tapes and condensed onto data summary tapes. Events from these data summary tapes were then stripped with broad cuts to supply a handful of tapes for looking at each specific signal. Only the strips of 170 GeV data are used in this thesis to find D mesons since the tracking resolution of the 137 GeV data is much poorer for an unknown reason. Also, Gerd Hartner's Cerenkov results are used for particle identification.

Reliable high speed data links between Fermilab and other sites, such as Santa Barbara, were an essential part of the data analysis. UCSB used a pair of 8 channel MICOM Micro 800/2 data concentrators with two Paradyne T-96 9600 baud modems, and a dedicated 4-wire RCA satellite link, to communicate with Fermilab. A Printronix P300 printer run at 4800 baud was attached to one of the 8 statistically multiplexed channels to provide printout. A four PROM chip set called Scientific Super-Sub Script (Printronix Part Number 104883 -- $150) was installed to provide 64 alternate characters. The normal ASCII characters and their corresponding alternates follow.

```
 !"#$%&'()*+,-./0123456789:;<=>?
o1234567890*+ħ_αβo1234567890∞+←−→±

@ABCDEFGHIJKLMNOPQRSTUVWXYZ[\]^_
ϰabcΔδΕΦΓijκΛγκλΠΨξΣθμνπxyzψρωσ
```

These special characters are used extensively throughout this thesis.

TABLE 6. PASS 2 TIMING IN CYBER MS PER EVENT

	TIME	% PASS 2
Calorimeter Calibration	8 ms	5%
Data Unpacking	10 ms	6%
Data Packing	21 ms	13%
Cerenkov (First Pass)	32 ms	21%
Cerenkov (Jim Elliott)	12 ms	8%
Cerenkov (Gerd Hartner)	6 ms	4%
Tagging Reconstruction	1 ms	1%
Vertex Finding	15 ms	10%
SLIC Analysis	45 ms	29%
Outrigger Reconstruction	2 ms	1%
Hadrometer Reconstruction	7 ms	4%
π^0 Reconstruction	3 ms	2%
Total	162 ms	

VI. D^{*+} MONTE CARLO

A. GENERATION AND CHARGED TRACK RECONSTRUCTION

A Monte Carlo simulation was used to generate events with charmed D mesons. The goal was to determine the efficiency of the spectrometer for reconstructing this sort of event so we could translate the observed D meson signals into a branching ratio quotient; $B(D^0 \to K^-\pi^+\pi^0) \;/\; B(D^0 \to K^-\pi^+)$. To find this quotient, 4988 $D^0 \to K^-\pi^+\pi^0$ and 4983 $D^0 \to K^-\pi^+$ events were generated and reconstructed. The required features of the Monte Carlo were the event generation, and the Drift Chamber, Cerenkov Counter, and π^0 reconstruction efficiencies.

Each Monte Carlo event began by simulating the bremsstrahlung production of a tagged photon in the copper radiator. A pseudo-random number generator was used to determine how many interactions took place in the radiator based on the radiation probabilities. The Monte Carlo was adjusted to match the observed photon beam energy spectrum and

the relative frequency of multiple bremsstrahlung and pair production in the radiator. A recoil proton and a heavy forward photon with mass ranging from the D^{*+} D^{*-} threshold (4.02 GeV/c^2) to 12 GeV/c^2 were generated. The generated mass squared distribution was flat to match our data. The invariant momentum transfer to the proton, t, was generated using $d\sigma/dt \propto e^{-3.5t}$. If the momentum transfer generated by this formula was kinematically impossible, another pseudo-random number was chosen.

A D^{*+} D^{*-} pair, accompanied by a few extra charged and neutral pions, was then produced out of the heavy photon using a pure phase space distribution. To match our data, the D^{*+} was preferentially aligned with direction of the heavy photon according to a $\cos^4\theta$ distribution in the heavy photon's center of mass frame. Both D^*'s were then taken to decay via $D^{*+}\rightarrow\pi^+D^0$ and $D^{*-}\rightarrow\pi^-\bar{D}^0$. The $\bar{D}^0$ decay multiplicity was then chosen based on SPEAR data.

The D^0 was then decayed either into $K^-\pi^+$ or $K^-\pi^+\pi^0$ depending on which of the two Monte Carlo

runs was being taken. The X-Y coordinates of tracks thus generated were then calculated for the position at each Drift Chamber plane and calorimeter. The magnetic fields bent the charged particles appropriately. Particles which collided with magnets stopped. Multiple scattering was added. The CERN Monte Carlo support package, GEANT, was used extensively throughout this process.

A resolution error was associated with each Drift Chamber wire. The error was usually the same throughout a plane. The U, V, or X position at a wire was generated by adding a pseudo-random gaussian resolution error in quadrature with a wire laying error. An overlay of crosstalk, false hits, and clusters was then provided to match the real data. With all these errors taken into account, TDC times were written onto tape just as in a real event. In addition a new data type containing the real 4-momenta, type, and decay history of all the Monte Carlo particles was added.

Each Monte Carlo track which was above threshold generated light in the Cerenkov Counters. A Poisson

like distribution, which matched the data, was used with pseudo-random numbers to pick exactly how many photoelectrons each track generated in each mirror. The number of photoelectrons per mirror was written onto tape. This procedure gave a good match to real data except for the four central mirrors in C1 which were on about 10% more often than than indicated by the Monte Carlo. This small correction was added directly to C1.

The Drift Chamber and Cerenkov data were reconstructed by the standard reconstruction program and an output tape was generated from the Monte Carlo input tape. The π^0 reconstruction efficiency, which is the major difference between the $D^0 \to K^-\pi^+$ and $D^0 \to K^-\pi^+\pi^0$ modes, is discussed in the next section.

The D^{*+} resolution generated by this Monte Carlo agrees with the real data. The Monte Carlo also has been used to generate $K^0_S \to \pi^+\pi^-$ peaks which look like the real ones.

B. π^0 RECONSTRUCTION EFFICIENCY

As mentioned in the previous section, the efficiency for finding the π^0 in each $D^0 \rightarrow K^-\pi^+\pi^0$ Monte Carlo event was needed. We constructed an efficiency lookup table to meet this need, by adding simulated electromagnetic showers to the showers already present in real events and then running these events through the usual calorimeter reconstruction program. The efficiency lookup table was constructed as a function of the π^0 probability (PRPIZ2), the number of particles hitting the calorimeters (multiplicity), π^0 momentum, and the angle of the π^0 with respect to the beam line. Generally, the π^0 reconstruction efficiency increased with momenta and angle, and decreased with multiplicity. In other words, it was easy to reconstruct large isolated photon showers. The efficiency lookup table was checked over a range of momenta by observing real $K^{*0}(899) \rightarrow K^+\pi^-$, $K^{*+}(892) \rightarrow K^+\pi^0$, $K^{*+}(892) \rightarrow K^0\pi^+$, and $K^{*0}(899) \rightarrow K^0\pi^0$ decays.

We chose the efficiency lookup table approach rather than trying to simulate the signals which would actually have been seen in the calorimeters for a particular D*+ Monte Carlo event. This approach avoided the difficult task of realistically modeling the energy deposits of hadronic showers.

I will first explain how the efficiency lookup table was generated, and then how it was used in the D*+ Monte Carlo. We could realistically simulate electron gamma showers with a program called EGS [48,49]. To determine the efficiency lookup table, EGS showers were added to real events. The events consisted of 100714 Recoil 2, 3, and 4 triggers from ten tape segments selected randomly throughout the 170 GeV data. The tapes were TM5024, TM5150, TM5093, TM4926, TM4919, TM4929, TM5060, TM4955, TM4853, and TM5109. Each event was assigned to one of five multiplicity ranges; 1→6, 7→9, 10→12, 13→15, and 16→36 particles. Two photons from one π^0 were added with EGS to each event. The π^0 momentum and angle with respect to the beam axis were randomly chosen from a selection of 24 momentum-angle

combinations. The six momenta were 7.5, 10.5, 14, 18, 26, and 40 GeV/c. The four angles pointed to circles on the face of the SLIC with radii of 1, 2, 3.5, and 5 feet. The π^0's were randomly distributed around the circles.

The decay of each π^0 was simulated to yield the 4-momenta of the two photons. If the photons both hit an electromagnetic calorimeter, were separated by a counter width, and exceeded the standard SLIC and Outrigger energy cuts of 2 and 1 GeV, EGS showers were used to add them to the real showers already in the calorimeters. If either photon failed to pass the geometry and energy cuts, the π^0 was decayed again. For the SLIC composition and geometry, forty EGS showers were stored on disk with ten each at energies of 0.2, 1, 5, and 25 GeV. For the geometry and composition of the Outriggers thirty EGS showers were stored on disk with ten each at the energies 0.2, 1, and 5 GeV. The EGS showers were thrown at any of six equally spaced locations in an $1^1/_4$" wide channel, i. e. the locations were approximately 1/5" apart. Once the the closest

available energy was determined, one of the ten showers at that energy was randomly chosen. The EGS shower energy was appropriately scaled before landing the shower in the calorimeter. The energy resolution of the SLIC as determined by EGS was $0.07/\sqrt{E}$. The Outrigger resolution from EGS was $0.14/\sqrt{E}$. In addition to the shower statistics already contained in EGS showers, the real photostatistic errors for each counter were added randomly with a gaussian function, as well as a randomized gaussian 2% calibration error.

Once the EGS showers had been added to the real showers and sufficiently scrambled, the event was run through the usual reconstruction program. If both photons were found within $1^{7}/_{8}$" of the thrown location and if they were reconstructed as a π^{o}, then the reconstruction was considered successful. We used the PRPIZ2 value assigned to each Monte Carlo π^{o} by the reconstruction program to generate the efficiency lookup table. The difference between the Monte Carlo π^{o} momentum and the reconstructed π^{o} momentum was used to generate a momentum resolution

lookup table. And finally, a position error lookup table was determined from a study of the difference between the Monte Carlo thrown and found locations.

Table 7 shows the π^0 efficiency for the geometry and energy cuts alone and the combination of these cuts with a PRPIZ2 cut of 0.8 plus a typical multiplicity of 7 to 9. Tables 8 through 13 are the actual lookup tables for reconstruction efficiency, momentum resolution, and position resolution. To get a feel for the tables, consider a typical 14 GeV/c π^0 pointing at a two foot radius circle on the face of the SLIC in an event with 7 to 9 particles hitting the calorimeters. This typical π^0 has a p_T of 460 MeV/c. We find that 72% of these π^0's pass the geometry and energy cuts. A PRPIZ2 cut of 0.8 reduces the overall reconstruction efficiency to 24%. The energy resolution for this π^0 is $0.14/\sqrt{E}$ and the position resolution is 1.5 cm.

With the π^0 reconstruction efficiency for any given π^0 4-momentum and for any given event multiplicity in hand, we weighted each Monte Carlo $D^0 \rightarrow K^-\pi^+\pi^0$ event from 0.0 to 1.0 depending on the

probability that the π^0 was found above a PRPIZ2 cut of 0.8, as determined by the efficiency lookup table. To determine this weight, we simulated each π^0 decay 200 times. Whenever both Monte Carlo photons hit an electromagnetic calorimeter, were separated by a counter width, and exceeded the standard SLIC and Outrigger energy cuts of 2 and 1 GeV, a pseudo-random number was used with the efficiency lookup table and linear interpolation. If the 0.8 PRPIZ2 cut was exceeded, the weight was incremented by 1/200. The PRPIZ2 value of the last accepted event was used to lookup gaussian errors for transforming the Monte Carlo π^0 4-momentum into a "reconstructed" π^0 4-momentum. The philosophy was to separate the geometry and energy cuts from the reconstruction efficiency.

With the weight for each $D^0 \rightarrow K^-\pi^+\pi^0$ event determined, we generated $D^{*+-}-D^0$ mass difference plots for the $D^0 \rightarrow K^-\pi^+$ and the $D^0 \rightarrow K^-\pi^+\pi^0$ Monte Carlo runs, using the data signal cuts discussed later. The $K^-\pi^+$ plot (Figure 45) has 451 signal events above background. The $K^-\pi^+\pi^0$ plot (Figure

46) has 111 signal events above background. Combining these signals with the number of original Monte Carlo events for each run we find that:

$$\frac{\varepsilon(K^-\pi^+\pi^0)}{\varepsilon(K^-\pi^+)} = \frac{(111/4983)}{(451/4988)} = \frac{0.022}{0.090} = 0.25\pm0.04$$

Finally, to check the π^0 efficiency lookup table, we found the ratio of charged to neutral pion reconstruction efficiencies by observing real K* decays. By comparing the number of observed K*'s in four channels a quantity can be found, which is independent of K^{*0} and K^{*+} production rates. The ratio of charged to neutral pion reconstruction efficiencies is thus given by:

$$\frac{\varepsilon(\pi^0)}{\varepsilon(\pi^+)} = 2\left[\frac{N(K^{*+} \to K^+\pi^0)}{N(K^{*0} \to K^+\pi^-)}\ \frac{N(K^{*0} \to K^0\pi^0)}{N(K^{*+} \to K^0\pi^+)}\right]^{1/2}$$

The factor of 2 comes from isospin conservation and Clebsch-Gordon coefficients.

$$|K^{*+}\rangle = |I, I_3\rangle = |1/2,\ 1/2\rangle = \sqrt{2/3}|\pi^+K^0\rangle - \sqrt{1/3}|\pi^0K^+\rangle$$
$$|\bar{K}^{*0}\rangle = |I, I_3\rangle = |1/2,\ 1/2\rangle = \sqrt{2/3}|\pi^+K^-\rangle - \sqrt{1/3}|\pi^0\bar{K}^0\rangle$$
$$|K^{*0}\rangle = |I, I_3\rangle = |1/2,-1/2\rangle = \sqrt{1/3}|\pi^0K^0\rangle - \sqrt{2/3}|\pi^-K^+\rangle$$
$$|K^{*-}\rangle = |I, I_3\rangle = |1/2,-1/2\rangle = \sqrt{1/3}|\pi^0K^-\rangle - \sqrt{2/3}|\pi^-\bar{K}^0\rangle$$

The results of this K* study are presented in Table 14 as a function of pion momentum. The final entries in the table compare the K* study π^0 reconstruction efficiency to the Monte Carlo π^0 reconstruction efficiency. The charged pion efficiency of 0.75±0.06 used to calculate the $\varepsilon(\pi^0)$ column is from a charged track Monte Carlo study and from observed $\rho^0 \rightarrow \pi^+\pi^-$ decays. The $\varepsilon(\pi^0$ Monte Carlo) column is for a multiplicity of 7 to 9 and a π^0 pointing at a two foot radius circle on the face of the SLIC. A PRPIZ2 cut of 0.8 was used throughout the table.

TABLE 7. π^0 MONTE CARLO EFFICIENCY

ENERGY AND GEOMETRY CUTS ONLY

MOMENTUM	1′	2′	3.5′	5′	RADIUS
7.5 GeV/c	.440	.495	.547	.561	
10.5 GeV/c	.583	.638	.669	.636	
14.0 GeV/c	.690	.716	.749	.628	
18.0 GeV/c	.763	.782	.797	.595	
26.0 GeV/c	.839	.843	.821	.511	
40.0 GeV/c	.881	.888	.714	.359	

COMBINED RECONSTRUCTION, ENERGY CUT,
AND GEOMETRY CUT EFFICIENCY
(PRPIZ2=0.8 and Multiplicity=7→9)

MOMENTUM	1′	2′	3.5′	5′	RADIUS
7.5 GeV/c	.046	.068	.147	.200	
10.5 GeV/c	.098	.177	.260	.231	
14.0 GeV/c	.134	.240	.353	.222	
18.0 GeV/c	.172	.318	.398	.216	
26.0 GeV/c	.230	.375	.430	.173	
40.0 GeV/c	.279	.434	.288	.071	

TABLE 8. 1′ AND 2′ π^0 FRACTIONS ABOVE PRPIZ2 CUTS

MULTIPLICITY	MOMENTUM	CASES	PRPIZ2 0.3	0.4	0.5	0.6	0.7	0.8	0.9
	R=1′								
M= 1→ 6	p= 7.5	706	.463	.429	.384	.340	.293	.177	.027p
M= 7→ 9		1038	.308	.255	.216	.193	.165	.104	.012
M=10→12		1075	.253	.203	.160	.139	.105	.062	.005
M=13→15		777	.216	.163	.120	.099	.075	.049	.005
M=16→36		537	.140	.104	.071	.060	.052	.026	.004
M= 1→ 6	p=10.5	723	.454	.412	.373	.350	.318	.246	.071p
M= 7→ 9		1093	.384	.341	.294	.259	.226	.168	.034
M=10→12		1143	.294	.246	.194	.164	.136	.097	.023
M=13→15		763	.248	.206	.169	.123	.107	.075	.013
M=16→36		579	.242	.190	.140	.111	.088	.054	.007
M= 1→ 6	p=14.0	770	.484	.447	.410	.381	.356	.286	.101p
M= 7→ 9		1079	.409	.357	.308	.272	.244	.195	.065
M=10→12		1120	.350	.297	.253	.217	.195	.154	.056
M=13→15		734	.317	.267	.215	.161	.140	.105	.038
M=16→36		565	.285	.232	.184	.140	.117	.083	.028
M= 1→ 6	p=18.0	783	.538	.503	.470	.444	.411	.361	.143p
M= 7→ 9		1119	.440	.397	.349	.316	.281	.226	.086
M=10→12		1058	.408	.366	.319	.273	.236	.185	.075
M=13→15		803	.347	.295	.247	.212	.179	.147	.072
M=16→36		495	.349	.295	.251	.192	.168	.121	.053
M= 1→ 6	p=26.0	739	.505	.484	.463	.437	.417	.368	.180p
M= 7→ 9		1063	.468	.437	.395	.347	.316	.274	.149
M=10→12		1077	.418	.383	.342	.297	.263	.230	.110
M=13→15		709	.412	.378	.343	.286	.261	.243	.111
M=16→36		515	.421	.384	.336	.256	.221	.200	.097
M= 1→ 6	p=40.0	834	.500	.477	.460	.438	.424	.388	.198p
M= 7→ 9		1102	.487	.454	.414	.372	.347	.317	.176
M=10→12		1070	.469	.427	.385	.335	.309	.293	.154
M=13→15		678	.451	.425	.383	.317	.301	.282	.147
M=16→36		529	.469	.435	.395	.316	.302	.263	.157
	R=2′								
M= 1→ 6	p= 7.5	630	.570	.532	.500	.462	.387	.248	.037p
M= 7→ 9		1005	.423	.372	.331	.293	.230	.137	.024
M=10→12		1146	.327	.249	.216	.186	.160	.094	.008
M=13→15		782	.249	.183	.141	.121	.092	.055	.003
M=16→36		589	.226	.168	.127	.104	.073	.044	.002
M= 1→ 6	p=10.5	679	.627	.579	.555	.530	.492	.376	.102p
M= 7→ 9		935	.534	.486	.448	.400	.354	.277	.080
M=10→12		1204	.436	.377	.321	.279	.235	.174	.031
M=13→15		869	.349	.290	.249	.209	.178	.125	.023
M=16→36		582	.337	.275	.199	.149	.131	.084	.015
M= 1→ 6	p=14.0	674	.712	.690	.665	.631	.599	.500	.196p
M= 7→ 9		1059	.598	.544	.499	.448	.415	.335	.130
M=10→12		1150	.503	.448	.383	.336	.299	.233	.079
M=13→15		783	.451	.396	.355	.292	.254	.190	.055
M=16→36		581	.399	.341	.279	.229	.194	.169	.046
M= 1→ 6	p=18.0	641	.736	.716	.686	.657	.633	.555	.243p
M= 7→ 9		1048	.625	.594	.551	.504	.468	.406	.180
M=10→12		1134	.538	.505	.448	.403	.358	.311	.145
M=13→15		775	.499	.435	.391	.325	.292	.246	.111
M=16→36		560	.429	.368	.316	.257	.220	.173	.091
M= 1→ 6	p=26.0	691	.729	.719	.700	.677	.657	.602	.362p
M= 7→ 9		1032	.639	.606	.577	.532	.498	.445	.254
M=10→12		1104	.629	.591	.551	.495	.453	.405	.226
M=13→15		790	.571	.515	.465	.406	.363	.323	.175
M=16→36		593	.509	.444	.403	.320	.280	.241	.121
M= 1→ 6	p=40.0	635	.694	.694	.685	.668	.657	.614	.356p
M= 7→ 9		1070	.645	.630	.602	.555	.539	.489	.290
M=10→12		1203	.609	.584	.559	.503	.480	.429	.266
M=13→15		755	.583	.552	.522	.468	.438	.403	.204
M=16→36		531	.601	.573	.529	.465	.435	.405	.241

TABLE 9. 3.5′ AND 5′ π^0 FRACTIONS ABOVE PRPIZ2 CUTS

MULTIPLICITY	RADIUS MOMENTUM	CASES	PRPIZ2 0.3	0.4	0.5	0.6	0.7	0.8	0.9
	R=3.5′								
M= 1→ 6	p= 7.5	673	.713	.675	.655	.633	.577	.327	.033p
M= 7→ 9		997	.595	.544	.517	.480	.414	.268	.013
M=10→12		1123	.540	.475	.436	.415	.359	.227	.013
M=13→15		833	.437	.361	.323	.295	.253	.156	.004
M=16→36		679	.302	.244	.214	.193	.155	.090	.004
M= 1→ 6	p=10.5	648	.779	.755	.739	.721	.696	.520	.097p
M= 7→ 9		1009	.695	.653	.618	.593	.551	.388	.047
M=10→12		1077	.568	.505	.466	.433	.398	.284	.049
M=13→15		825	.484	.427	.381	.358	.327	.250	.038
M=16→36		586	.403	.343	.305	.271	.241	.166	.027
M= 1→ 6	p=14.0	628	.787	.774	.763	.747	.705	.580	.150p
M= 7→ 9		991	.665	.643	.616	.582	.555	.471	.112
M=10→12		1084	.621	.560	.513	.487	.451	.367	.100
M=13→15		837	.532	.496	.454	.424	.393	.331	.086
M=16→36		625	.504	.448	.403	.365	.334	.266	.086
M= 1→ 6	p=18.0	670	.737	.727	.716	.701	.672	.597	.243p
M= 7→ 9		964	.692	.667	.641	.619	.581	.500	.170
M=10→12		1054	.627	.590	.546	.519	.484	.419	.147
M=13→15		733	.570	.543	.503	.471	.441	.379	.151
M=16→36		602	.527	.485	.440	.415	.382	.321	.111
M= 1→ 6	p=26.0	695	.735	.731	.718	.708	.672	.583	.269p
M= 7→ 9		975	.688	.672	.644	.615	.592	.524	.224
M=10→12		1089	.637	.616	.593	.556	.518	.462	.202
M=13→15		790	.595	.566	.516	.473	.447	.385	.186
M=16→36		592	.544	.515	.476	.436	.410	.350	.157
M= 1→ 6	p=40.0	714	.560	.541	.529	.508	.482	.405	.154p
M= 7→ 9		1048	.562	.553	.536	.510	.481	.404	.154
M=10→12		1124	.527	.505	.476	.455	.421	.362	.157
M=13→15		784	.532	.508	.469	.431	.402	.349	.159
M=16→36		553	.445	.427	.391	.365	.349	.282	.105
	R=5′								
M= 1→ 6	p= 7.5	688	.641	.632	.619	.606	.564	.390	.015p
M= 7→ 9		1052	.594	.576	.553	.534	.493	.356	.019
M=10→12		1113	.537	.503	.485	.463	.420	.287	.011
M=13→15		789	.471	.425	.401	.371	.332	.208	.005
M=16→36		621	.357	.317	.300	.280	.245	.169	.006
M= 1→ 6	p=10.5	658	.605	.591	.581	.559	.533	.397	.043p
M= 7→ 9		1021	.587	.568	.547	.536	.497	.363	.035
M=10→12		1080	.525	.505	.481	.463	.429	.324	.041
M=13→15		773	.444	.419	.395	.373	.340	.242	.028
M=16→36		575	.438	.402	.365	.346	.292	.217	.030
M= 1→ 6	p=14.0	754	.533	.523	.513	.507	.481	.377	.076p
M= 7→ 9		981	.520	.512	.491	.479	.460	.353	.090
M=10→12		1064	.521	.502	.480	.463	.435	.338	.085
M=13→15		772	.466	.444	.420	.402	.377	.291	.065
M=16→36		578	.386	.358	.343	.317	.284	.220	.048
M= 1→ 6	p=18.0	787	.471	.468	.459	.443	.422	.341	.093p
M= 7→ 9		1004	.528	.507	.493	.478	.450	.363	.127
M=10→12		1112	.486	.472	.459	.446	.421	.339	.112
M=13→15		727	.453	.436	.417	.400	.374	.314	.124
M=16→36		597	.404	.375	.350	.333	.320	.251	.102
M= 1→ 6	p=26.0	811	.390	.387	.383	.369	.350	.289	.110p
M= 7→ 9		1024	.450	.442	.431	.417	.396	.338	.129
M=10→12		1083	.441	.432	.422	.405	.385	.320	.137
M=13→15		750	.447	.432	.412	.388	.367	.309	.141
M=16→36		545	.424	.400	.378	.356	.332	.279	.116
M= 1→ 6	p=40.0	835	.275	.273	.268	.260	.240	.193	.069p
M= 7→ 9		1049	.285	.276	.269	.257	.231	.197	.078
M=10→12		1092	.320	.306	.298	.284	.260	.213	.080
M=13→15		718	.291	.276	.263	.251	.235	.195	.071
M=16→36		553	.297	.282	.260	.250	.230	.199	.063

TABLE 10. 1′ AND 2′ π^0 ENERGY ERRORS DIVIDED BY $\sqrt{E}$

MULTIPLICITY	RADIUS MOMENTUM	PRPIZ2 0.3	0.4	0.5	0.6	0.7	0.8	0.9
	R=1′							
M= 1→ 6	p= 7.5	.150	.116	.102	.189	.078	.062	.046p
M= 7→ 9		.108	.072	.080	.088	.084	.070	.026
M=10→12		.105	.071	.115	.093	.089	.067	.067
M=13→15		.094	.067	.046	.077	.087	.100	.032
M=16→36		.124	.037	.056	.024	.045	.076	.050
M= 1→ 6	p=10.5	.170	.153	.224	.138	.133	.095	.073p
M= 7→ 9		.162	.173	.098	.117	.133	.107	.081
M=10→12		.167	.154	.095	.157	.118	.112	.068
M=13→15		.162	.118	.107	.125	.108	.094	.172
M=16→36		.113	.118	.187	.065	.157	.095	.112
M= 1→ 6	p=14.0	.223	.195	.138	.263	.164	.166	.094p
M= 7→ 9		.260	.197	.157	.157	.195	.139	.103
M=10→12		.244	.198	.193	.161	.242	.162	.089
M=13→15		.178	.174	.177	.165	.215	.125	.105
M=16→36		.198	.188	.116	.082	.147	.123	.097
M= 1→ 6	p=18.0	.294	.351	.148	.182	.245	.189	.130p
M= 7→ 9		.185	.176	.233	.177	.213	.220	.102
M=10→12		.202	.157	.234	.205	.251	.178	.173
M=13→15		.214	.209	.137	.215	.255	.231	.154
M=16→36		.201	.177	.142	.146	.177	.200	.100
M= 1→ 6	p=26.0	.213	.411	.402	.284	.365	.363	.192p
M= 7→ 9		.438	.360	.259	.273	.458	.260	.207
M=10→12		.542	.362	.376	.348	.277	.313	.191
M=13→15		.336	.230	.392	.331	.548	.302	.220
M=16→36		.350	.343	.378	.284	.210	.351	.220
M= 1→ 6	p=40.0	.447	.674	.356	.485	.870	.433	.281p
M= 7→ 9		.615	.689	.676	.539	.588	.496	.313
M=10→12		.864	.560	.344	.396	.501	.591	.322
M=13→15		.470	.392	.427	.308	.962	.467	.345
M=16→36		.471	.518	.620	.227	.388	.467	.265
	R=2′							
M= 1→ 6	p= 7.5	.081	.091	.099	.115	.092	.063	.041p
M= 7→ 9		.120	.115	.103	.130	.088	.064	.043
M=10→12		.094	.095	.142	.084	.093	.064	.053
M=13→15		.084	.109	.119	.120	.133	.054	.013
M=16→36		.087	.079	.071	.121	.085	.093	.001
M= 1→ 6	p=10.5	.152	.130	.115	.110	.098	.100	.061p
M= 7→ 9		.148	.122	.160	.119	.128	.104	.078
M=10→12		.129	.127	.093	.155	.129	.120	.071
M=13→15		.118	.133	.146	.169	.124	.090	.093
M=16→36		.114	.130	.193	.114	.113	.150	.072
M= 1→ 6	p=14.0	.135	.214	.190	.158	.173	.133	.082p
M= 7→ 9		.188	.188	.128	.159	.186	.143	.088
M=10→12		.153	.172	.127	.216	.154	.147	.104
M=13→15		.163	.193	.186	.180	.167	.157	.107
M=16→36		.188	.207	.180	.287	.179	.170	.158
M= 1→ 6	p=18.0	.145	.206	.145	.200	.180	.174	.112p
M= 7→ 9		.187	.294	.267	.203	.197	.179	.138
M=10→12		.242	.187	.203	.246	.232	.165	.150
M=13→15		.173	.230	.209	.243	.239	.169	.150
M=16→36		.244	.353	.186	.226	.185	.187	.161
M= 1→ 6	p=26.0	.256	.271	.218	.237	.337	.233	.171p
M= 7→ 9		.337	.263	.245	.242	.265	.246	.179
M=10→12		.301	.294	.303	.272	.305	.304	.224
M=13→15		.302	.292	.273	.235	.371	.294	.209
M=16→36		.349	.218	.435	.251	.365	.246	.217
M= 1→ 6	p=40.0	1.000	.587	.353	1.064	.589	.440	.290p
M= 7→ 9		.358	.649	.340	.477	.645	.441	.308
M=10→12		.482	.389	.748	.679	.625	.435	.313
M=13→15		.686	.634	.360	.693	.513	.475	.284
M=16→36		.353	.426	.323	.426	.541	.392	.334

TABLE 11. 3.5′ AND 5′ π^0 ENERGY ERRORS DIVIDED BY $\sqrt{E}$

MULTIPLICITY	RADIUS MOMENTUM	PRPIZ2 0.3	0.4	0.5	0.6	0.7	0.8	0.9
	R=3.5′							
M= 1→ 6	p= 7.5	.108	.181	.210	.161	.165	.098	.056p
M= 7→ 9		.123	.171	.149	.166	.162	.126	.065
M=10→12		.133	.133	.141	.143	.166	.143	.033
M=13→15		.154	.077	.132	.146	.126	.137	.054
M=16→36		.135	.081	.115	.147	.128	.126	.069
M= 1→ 6	p=10.5	.216	.227	.245	.281	.225	.141	.095p
M= 7→ 9		.251	.169	.239	.281	.191	.194	.075
M=10→12		.214	.328	.144	.171	.200	.170	.076
M=13→15		.169	.222	.115	.189	.173	.196	.109
M=16→36		.200	.141	.102	.184	.205	.201	.092
M= 1→ 6	p=14.0	.281	.253	.225	.332	.275	.239	.122p
M= 7→ 9		.253	.216	.196	.266	.350	.258	.151
M=10→12		.245	.370	.157	.290	.321	.220	.113
M=13→15		.337	.167	.222	.390	.254	.246	.160
M=16→36		.362	.262	.130	.281	.214	.232	.133
M= 1→ 6	p=18.0	.246	.309	.244	.525	.340	.289	.165p
M= 7→ 9		.352	.313	.310	.467	.384	.321	.179
M=10→12		.293	.273	.362	.330	.421	.315	.177
M=13→15		.492	.301	.316	.483	.280	.354	.191
M=16→36		.337	.310	.248	.358	.401	.287	.168
M= 1→ 6	p=26.0	.191	.215	.493	.622	.663	.547	.318p
M= 7→ 9		.677	.628	.600	.723	.711	.485	.298
M=10→12		.747	.526	.492	.634	.664	.523	.324
M=13→15		.528	.420	.657	.569	.496	.500	.280
M=16→36		.622	.444	.757	.585	.729	.591	.337
M= 1→ 6	p=40.0	1.406	1.248	1.781	1.392	1.213	.785	.518p
M= 7→ 9		1.909	1.513	1.303	1.536	1.301	.930	.488
M=10→12		1.806	1.498	1.604	1.410	1.201	.879	.563
M=13→15		1.288	1.444	1.053	1.398	1.146	.879	.569
M=16→36		.639	.925	1.004	1.194	1.307	.797	.494
	R=5′							
M= 1→ 6	p= 7.5	.332	.151	.557	.209	.137	.147	.049p
M= 7→ 9		.241	.268	.260	.219	.183	.156	.066
M=10→12		.139	.231	.303	.134	.136	.149	.039
M=13→15		.139	.122	.184	.213	.147	.162	.027
M=16→36		.167	.171	.138	.182	.179	.163	.059
M= 1→ 6	p=10.5	.673	.472	.453	.337	.249	.197	.069p
M= 7→ 9		.195	.719	.168	.370	.257	.206	.089
M=10→12		.495	.469	.259	.409	.261	.214	.092
M=13→15		.647	.252	.368	.231	.299	.211	.085
M=16→36		.193	.399	.195	.294	.411	.235	.063
M= 1→ 6	p=14.0	.575	.559	.675	.583	.389	.262	.121p
M= 7→ 9		.202	.956	.454	.459	.407	.255	.122
M=10→12		.493	.479	.454	.592	.375	.269	.132
M=13→15		.675	.452	.336	.337	.493	.293	.137
M=16→36		.189	.320	.218	.392	.414	.294	.094
M= 1→ 6	p=18.0	1.024	1.216	.674	.651	.542	.353	.179p
M= 7→ 9		.400	.748	1.054	.747	.554	.354	.183
M=10→12		.850	.296	1.024	.754	.512	.367	.207
M=13→15		.530	.594	.324	.617	.591	.337	.175
M=16→36		.889	.496	.753	.617	.583	.434	.178
M= 1→ 6	p=26.0	1.479	.941	1.002	.707	.661	.503	.294p
M= 7→ 9		.727	1.340	.990	1.103	.821	.531	.375
M=10→12		.654	.509	.714	.846	.782	.583	.297
M=13→15		.632	.828	.636	.945	.652	.554	.384
M=16→36		.744	.617	.440	.628	.943	.495	.239
M= 1→ 6	p=40.0	1.838	1.084	1.101	1.136	1.204	.871	.557p
M= 7→ 9		1.756	1.805	1.252	1.429	1.176	.827	.565
M=10→12		1.313	1.497	1.368	1.387	1.139	.857	.632
M=13→15		1.157	1.119	1.056	1.227	1.026	.768	.715
M=16→36		1.344	1.564	1.138	1.587	1.365	.789	.442

TABLE 12. 1′ AND 2′ π^0 POSITION ERRORS IN CM

MULTIPLICITY	MOMENTUM	RADIUS PRPIZ2 0.3	0.4	0.5	0.6	0.7	0.8	0.9
	R=1′							
M= 1→ 6	p= 7.5	4.24	3.44	3.48	3.77	2.86	2.29	1.85p
M= 7→ 9		3.54	2.92	3.84	3.71	2.90	2.72	1.45
M=10→12		3.99	2.39	3.57	3.63	3.89	2.96	1.40
M=13→15		3.18	3.08	2.85	3.49	2.99	3.30	2.01
M=16→36		4.51	2.89	3.64	1.44	3.05	2.67	3.73
M= 1→ 6	p=10.5	2.28	2.36	2.84	2.38	2.69	1.97	1.72p
M= 7→ 9		2.48	2.35	2.57	2.13	2.37	2.13	1.52
M=10→12		2.81	2.42	1.92	2.68	2.51	1.75	1.63
M=13→15		2.72	1.67	2.23	2.22	2.03	2.11	2.82
M=16→36		2.75	2.34	2.26	3.67	2.84	1.75	1.97
M= 1→ 6	p=14.0	2.08	1.96	1.97	2.96	1.92	1.42	1.19p
M= 7→ 9		2.56	2.01	1.85	1.76	1.57	1.48	1.36
M=10→12		2.04	1.61	1.90	1.91	1.84	1.76	1.16
M=13→15		1.49	1.46	2.20	1.62	1.72	1.48	1.66
M=16→36		1.66	2.13	1.72	2.14	1.44	1.79	1.69
M= 1→ 6	p=18.0	1.39	1.65	.94	1.07	1.18	1.31	.90p
M= 7→ 9		1.24	1.20	1.14	1.23	1.50	1.27	1.05
M=10→12		1.56	1.17	1.40	1.47	1.79	1.27	1.33
M=13→15		1.17	1.82	1.42	1.42	1.69	1.35	1.26
M=16→36		1.31	2.66	1.74	1.01	1.41	1.29	1.16
M= 1→ 6	p=26.0	1.12	1.19	1.30	1.25	1.20	1.02	.87p
M= 7→ 9		1.24	1.07	1.17	1.14	1.17	.97	.88
M=10→12		1.29	1.17	1.17	1.13	1.06	1.01	.90
M=13→15		1.56	1.50	1.24	1.12	1.36	1.21	.89
M=16→36		1.49	.98	1.36	1.17	1.17	1.03	1.00
M= 1→ 6	p=40.0	.95	1.12	.88	1.13	1.48	.78	.73p
M= 7→ 9		.95	1.11	.86	1.04	1.28	.98	.74
M=10→12		.97	.92	.77	1.01	.88	.92	.80
M=13→15		.94	1.28	.82	1.58	.98	.89	.71
M=16→36		1.08	.91	.68	.83	1.24	1.03	.83
	R=2′							
M= 1→ 6	p= 7.5	3.33	3.39	3.11	3.13	3.11	2.24	1.85p
M= 7→ 9		4.44	3.20	3.44	3.56	3.12	2.63	2.08
M=10→12		3.68	2.66	3.61	3.46	3.17	2.54	2.53
M=13→15		3.63	4.01	3.92	3.67	3.19	2.88	.74
M=16→36		3.45	2.66	3.55	5.57	3.45	3.72	4.12
M= 1→ 6	p=10.5	2.26	2.03	3.10	1.38	1.90	1.71	1.55p
M= 7→ 9		2.38	2.35	2.47	2.56	2.00	1.89	1.67
M=10→12		3.06	2.66	1.55	2.54	2.31	2.14	1.40
M=13→15		1.96	2.15	2.36	2.66	2.46	1.89	2.12
M=16→36		2.19	2.46	2.50	1.58	2.01	2.54	1.92
M= 1→ 6	p=14.0	1.61	1.88	2.07	1.76	1.78	1.44	1.19p
M= 7→ 9		2.09	1.90	1.43	1.56	1.37	1.46	1.20
M=10→12		1.93	1.64	1.84	1.75	1.85	1.71	1.27
M=13→15		1.53	1.70	1.80	2.09	1.84	1.76	1.23
M=16→36		2.26	2.23	1.47	2.14	1.57	1.78	1.25
M= 1→ 6	p=18.0	1.53	1.72	1.16	1.47	1.33	1.12	1.10p
M= 7→ 9		1.20	1.58	1.36	1.31	1.34	1.17	1.09
M=10→12		1.56	1.31	1.45	1.14	1.30	1.26	1.25
M=13→15		1.40	1.47	1.40	1.29	1.38	1.31	1.21
M=16→36		1.62	2.06	1.44	1.55	1.41	1.42	1.31
M= 1→ 6	p=26.0	.87	1.22	1.15	1.09	1.07	1.13	.89p
M= 7→ 9		1.42	.96	.94	.97	1.24	1.01	1.01
M=10→12		1.28	1.12	1.14	.86	1.05	1.12	.98
M=13→15		1.06	1.38	1.08	1.09	1.05	1.01	1.01
M=16→36		1.09	.89	1.27	1.00	1.23	1.14	1.08
M= 1→ 6	p=40.0	.00	.79	.99	.88	.85	.95	.90p
M= 7→ 9		.95	1.03	.84	1.03	.98	.96	.85
M=10→12		.87	.76	.98	1.04	.98	1.02	.87
M=13→15		.98	.94	1.01	1.09	1.19	.92	.89
M=16→36		1.04	.89	.98	1.07	.99	.97	.94

TABLE 13. 3.5′ AND 5′ π^0 POSITION ERRORS IN CM

MULTIPLICITY	MOMENTUM	RADIUS PRPIZ2 0.3	0.4	0.5	0.6	0.7	0.8	0.9
	R=3.5′							
M= 1→ 6	p= 7.5	5.46	5.75	3.55	4.12	4.20	2.86	1.98p
M= 7→ 9		3.83	4.24	3.55	3.54	3.27	3.31	2.54
M=10→12		3.47	4.03	2.64	4.00	3.99	3.50	1.77
M=13→15		3.92	3.93	2.53	3.84	4.52	3.89	1.90
M=16→36		3.11	4.71	2.66	3.65	4.07	4.78	1.83
M= 1→ 6	p=10.5	4.13	2.36	4.40	3.80	3.43	2.67	1.55p
M= 7→ 9		3.58	3.81	2.91	5.20	3.61	2.88	1.76
M=10→12		3.72	3.24	2.22	2.41	3.17	2.91	1.60
M=13→15		3.16	3.85	2.57	3.86	3.34	3.32	1.86
M=16→36		3.38	1.90	2.80	3.10	3.32	3.18	1.34
M= 1→ 6	p=14.0	4.35	2.97	3.83	3.73	3.68	2.58	1.61p
M= 7→ 9		3.03	3.09	2.48	2.48	2.72	2.72	1.68
M=10→12		2.95	3.38	2.25	3.86	2.89	2.67	1.62
M=13→15		2.89	2.53	1.97	4.58	2.91	2.73	1.78
M=16→36		2.85	2.78	1.55	3.54	2.90	2.50	1.79
M= 1→ 6	p=18.0	3.22	2.81	1.65	4.75	2.89	2.67	1.72p
M= 7→ 9		2.02	2.88	2.23	3.36	3.06	2.53	1.65
M=10→12		2.24	2.96	3.31	2.70	3.83	2.47	1.69
M=13→15		3.64	2.34	2.11	3.22	2.03	2.49	1.68
M=16→36		2.33	3.04	1.72	2.42	2.65	2.26	1.93
M= 1→ 6	p=26.0	2.19	1.45	1.99	3.51	3.07	2.63	1.86p
M= 7→ 9		2.31	2.15	3.08	3.26	2.87	2.40	1.64
M=10→12		3.17	2.81	1.54	3.16	3.51	2.61	1.66
M=13→15		3.23	2.27	2.57	2.21	2.53	2.48	1.82
M=16→36		2.13	2.93	2.59	2.23	2.88	2.15	2.11
M= 1→ 6	p=40.0	3.24	5.07	3.58	5.25	3.40	2.26	2.30p
M= 7→ 9		3.45	2.76	2.77	2.94	3.45	2.80	2.02
M=10→12		2.37	2.82	3.90	3.60	2.73	2.41	2.23
M=13→15		2.82	3.21	1.76	3.28	2.70	2.04	2.02
M=16→36		1.95	1.63	1.46	3.26	2.21	2.34	1.62
	R=5′							
M= 1→ 6	p= 7.5	8.09	5.49	5.14	6.50	4.80	5.07	2.75p
M= 7→ 9		6.17	5.75	4.68	4.95	4.91	5.28	2.34
M=10→12		4.49	6.23	5.62	5.72	4.85	5.23	2.05
M=13→15		5.65	2.88	5.40	6.54	5.22	4.61	2.61
M=16→36		4.89	6.26	4.46	5.50	4.91	5.26	1.59
M= 1→ 6	p=10.5	5.81	4.70	6.49	5.18	4.66	4.03	1.93p
M= 7→ 9		3.88	4.75	5.26	5.48	5.10	4.03	1.90
M=10→12		3.52	3.89	3.96	5.21	4.42	3.96	2.15
M=13→15		3.74	4.87	4.80	4.73	5.21	4.14	2.43
M=16→36		3.89	4.83	3.96	5.93	4.20	3.85	1.97
M= 1→ 6	p=14.0	3.35	5.73	5.49	5.36	4.98	3.78	1.88p
M= 7→ 9		2.98	4.88	5.56	5.30	4.79	3.86	1.87
M=10→12		2.74	3.02	3.63	4.39	4.05	3.68	2.13
M=13→15		3.21	2.59	3.91	3.90	4.52	3.43	1.56
M=16→36		2.72	3.07	2.39	3.37	3.41	3.29	1.71
M= 1→ 6	p=18.0	6.73	5.22	4.31	5.01	5.54	2.98	2.03p
M= 7→ 9		5.42	3.84	4.52	4.64	4.60	3.73	1.81
M=10→12		4.17	2.43	4.71	4.64	4.19	3.55	1.91
M=13→15		2.82	3.19	5.34	4.47	4.74	3.61	1.82
M=16→36		3.32	2.14	5.35	5.54	4.76	3.85	1.61
M= 1→ 6	p=26.0	6.91	4.71	3.14	4.86	4.49	3.16	2.04p
M= 7→ 9		4.24	4.40	4.13	4.65	4.41	3.04	2.37
M=10→12		4.45	2.54	3.00	3.44	4.13	3.01	2.27
M=13→15		2.05	3.75	2.87	3.10	3.94	3.08	1.94
M=16→36		2.68	3.36	3.08	3.26	4.20	2.90	1.70
M= 1→ 6	p=40.0	5.38	2.00	3.17	3.49	3.49	3.07	2.71p
M= 7→ 9		3.59	2.84	2.83	3.31	3.07	2.82	2.50
M=10→12		1.68	3.96	3.77	3.86	3.34	3.02	2.41
M=13→15		3.67	2.40	1.65	2.90	3.74	2.54	2.26
M=16→36		4.65	4.35	2.87	3.37	2.36	2.25	1.85

TABLE 14. K* DECAYS AND π^0 RECONSTRUCTION EFFICIENCIES

P(PION) GeV/c	$K^{*0}\to K^+\pi^-$	$K^{*+}\to K^+\pi^0$	$2K^+\pi^0/K^+\pi^-$
6→ 8	1109±115	25±25	.05±.05
8→10	738±100	43±32	.12±.09
10→12	580±85	91±31	.31±.10
12→16	660±130	176±65	.54±.17
16→22	700±125	230±50	.60±.20
>22	554±120	200±80	.70±.30

GeV/c	$K^{*+}\to K^0\pi^+$	$K^{*0}\to K^0\pi^0$	$2K^0\pi^0/K^0\pi^+$	$\varepsilon(\pi^0)/\varepsilon(\pi^+)$
6→ 9	935±100	84±27	.18±.06	.13±.05
9→12	734± 75	85±27	.18±.08	.21±.07
12→16	608± 75	104±30	.33±.10	.40±.08
16→20	416± 70	90±25	.43±.12	.46±.10
20→32	434± 75	105±26	.48±.12	.50±.12
>32	80± 40	30±14	.75±.50	

GeV/c	$\varepsilon(\pi^0)$	$\varepsilon(\pi^0$ Monte Carlo)
6→ 9	.10±.04	.07±.01
9→12	.16±.05	.18±.01
12→16	.30±.06	.24±.01
16→20	.34±.08	.32±.02
20→32	.38±.10	.38±.02

Note that

$$\frac{\varepsilon(\pi^0)}{\varepsilon(\pi^+)} = 2\left[\frac{N(K^{*+}\to K^+\pi^0)}{N(K^{*0}\to K^+\pi^-)}\ \frac{N(K^{*0}\to K^0\pi^0)}{N(K^{*+}\to K^0\pi^+)}\right]^{1/2}$$

The factor of 2 comes from isospin conservation.

$$|K^{*+}\rangle = |I, I_3\rangle = |1/2,\ 1/2\rangle = \sqrt{2/3}|\pi^+K^0\rangle - \sqrt{1/3}|\pi^0K^+\rangle$$
$$|\bar{K}^{*0}\rangle = |I, I_3\rangle = |1/2,\ 1/2\rangle = \sqrt{2/3}|\pi^+K^-\rangle - \sqrt{1/3}|\pi^0\bar{K}^0\rangle$$
$$|K^{*0}\rangle = |I, I_3\rangle = |1/2,-1/2\rangle = \sqrt{1/3}|\pi^0K^0\rangle - \sqrt{2/3}|\pi^-K^+\rangle$$
$$|K^{*-}\rangle = |I, I_3\rangle = |1/2,-1/2\rangle = \sqrt{1/3}|\pi^0K^-\rangle - \sqrt{2/3}|\pi^-\bar{K}^0\rangle$$

VII. $D^0 \to K^-\pi^+\pi^0$ BRANCHING RATIO

A. $D^0 \to K^-\pi^+$ AND $D^0 \to K^-\pi^+\pi^0$ SIGNALS

We have observed two decay cascades [50,51]; $D^{*+} \to D^0\pi^+$, $D^0 \to K^-\pi^+$ and $D^{*+} \to D^0\pi^+$, $D^0 \to K^-\pi^+\pi^0$, $\pi^0 \to \gamma\gamma$. (The charge conjugate is implicitly included for all reactions.)

The $D^{*+} - D^0$ mass difference of 145.4 ± 0.2 MeV/c^2 makes the Q value for the decay $D^{*+} \to D^0\pi^+$ quite small (5.8 MeV) [1]. Our mass difference resolution was 30 times better than the resolution of the D^{*+} or D^0 masses alone because the low Q value ($M(D^{*+}) - M(D^0) - M(\pi^+)$) allowed the subtraction to cancel most of the measurement errors. The mass difference resolution is proportional to $Q^{1/2}$. The background is proportional to the phase space accepted within our resolution in Q. This is small both because the resolution width is small and because the phase space is proportional to $Q^{1/2}$, as discussed below. Both the good mass difference resolution and small amount of background allowed by phase space were

needed to find significant D^0 signals. Our background in the region of the D^0 mass was too large to find the D^0 directly.

The following cuts were used to obtain signals. The first six cuts were used to reject poor quality tracks which had not contributed to other signals such as the decays $K^0_S \rightarrow \pi^+\pi^-$, $\Lambda \rightarrow p\pi^-$, and $\phi \rightarrow K^+K^-$. These poor quality tracks only added background to these signals.

1) Each track had to have at least 8 degrees of freedom; that is it had to be seen in enough Drift Chamber planes to be believable.

2) We rejected tracks seen only in D1 for the same reason.

3) We rejected spurious tracks.

4) The fit of each track to the primary vertex had to pass a CHTSQ<3.8 cut, because the D^{*+} and D^0 both decay at the primary vertex within the limits of our resolution.

5) The Cerenkov probabilities were divided by two for category 3 tracks (D1-D2). These tracks were less reliable than those seen in all four sets of Drift Chamber planes.

6) We rejected tracks with energies exceeding ETAG as unphysical.

7) We rejected runs determined by Jim Pinfold to have too few K^0_S's, which indicated that the Drift Chambers were not working properly.

8) The kaon Cerenkov probability had to be above above .29 and both charged pion Cerenkov probabilities had to be above .39 . These rather minimal cuts were used to reduce the number of events under consideration to a more manageable level.

9) We demanded that the π^0 probability, PRPIZ2, be greater than 0.8 . This cut was determined from a study of the decay $\omega \to \pi^+\pi^-\pi^0$.

10) We required that the joint 3-fold probability, $PR(K^-,\pi^+,\pi^+) = PR(K^-)\cdot PR(\pi^+)\cdot PR(\pi^+)$, be greater than 0.20 . Cutting on a joint probability distribution [52] provided an unbiased way to produce a larger signal than individual cuts. For example, an event with a well identified kaon and two below average charged pions might be rejected with individual cuts for each particle. But such an event is just as good as an event with three medium quality charged tracks, and should be accepted.

11) The $K^-\pi^+(\pi^0)$ mass had to be within 60 Mev/c^2 of D^0 mass. This relatively large mass cut minimized systematic errors arising from possible differences in the resolution of the D^0 mass for the two decay modes.

12) Finally, we used a cut on the D*+ energy, E(D*+)/ETAG > 0.35, to reduce background.

For each $K^-\pi^+\pi^+$ and $K^-\pi^+\pi^0\pi^+$ combination passing these cuts, the mass difference $\Delta M = M(K^-\pi^+(\pi^0)\pi^+) - M(K^-\pi^+(\pi^0))$ is plotted in Figures 47 and 48. The data set was fit to a background shape $aQ^{1/2}(1-bQ)$ (where $Q/c^2 = \Delta M - M_{\pi^+}$ and a and b are constants) plus a Gaussian centered at $\Delta M = 145.4$ MeV/c^2 with σ = 1.2 Mev/c^2. The background shape is the product of a phase space factor times an acceptance correction. In the non-relativistic limit, $Q=p^2/2m$, where p is the pion momentum in the rest frame of the D^{*+}. A volume element in momentum space is as follows.

$$(2\pi\hbar)^{-3}p^2dpd\Omega = (2\pi\hbar)^{-3}2mQd(2mQ)^{1/2}d\Omega$$

$$= (2\pi\hbar)^{-3}(2m^3Q)^{1/2}dQd\Omega$$

Thus the background density of states increases as $aQ^{1/2}$. The 1-bQ term allows a small correction to the shape of the background for acceptance. No terms of higher order were needed to give good fits to the background. The background shape also fits the Cabibbo suppressed (e. g. $D^0\rightarrow K^+\pi^-$) mass difference plots quite well. These Cabibbo suppressed plots show little or no signal. For our

Cabibbo favored signals, the fit gives 39±8 $D^0 \to K^-\pi^+$ events and 41±9 $D^0 \to K^-\pi^+\pi^0$ events. These signals are used to derive the $D^0 \to K^-\pi^+\pi^0$ branching ratio calculated in the next section. The branching ratio analysis used exactly the same cuts on the three charged particles for both modes. The efficiency for detecting the two modes thus depended mainly on the π^0 Monte Carlo and possible tracking Monte Carlo errors tended to cancel.

To obtain a more statistically significant signal for the $K^-\pi^+\pi^0$ Dalitz plot, which is described later, we used a 50 MeV/c^2 D^0 mass cut and a 4-fold probability cut, instead of the 60 MeV/c^2 D^0 mass cut and the separate cuts on π^0 probability and charged track Cerenkov probabilities (3-fold cut) discussed earlier. The 4-fold cut demanded that PR(K^-, π^+, π^0, π^+) = PR(K^-)·PR(π^+)·PIZPRB(PRPIZ2)·PR(π^+) be greater than 0.11 . This mass difference plot is shown in Figure 49 and contains 54 ± 12 events. Figure 50 shows the effect of removing the E(D*+)/ETAG cut. Figures 51 and 52 show mass difference plots equivalent to Figures 49 and 50,

when at least one of the π^0 photons was found in the Outriggers.

Figures 53 through 56 show D^0 and D^{*+} peaks obtained by choosing $D^{*+} - D^0$ mass difference events between 144 MeV/c^2 and 147 MeV/c^2 and then looking back to find the D mesons. All the cuts are the same for the lookback plots as for the mass difference plots with the exception of the D^0 mass cut, which was not required. The $K^-\pi^+\pi^0$ lookback plots come from the 4-fold probability mass difference plot (Figure 49). The lookback plots confirm the authenticity of the $D^{*+} - D^0$ mass difference peaks and show the effect of the D^0 mass cut.

B. EVENT DETECTION EFFICIENCY

To determine the quotient of branching fractions $B(D^0 \to K^-\pi^+\pi^0)/B(D^0 \to K^-\pi^+)$, the relative efficiency for detecting the two modes is needed. Most factors, such as the beam flux and spectrum, trigger efficiencies, and target size, are common to both modes. The relative reconstruction and identification efficiencies are the only factors to be calculated from Monte Carlo studies.

The biggest difference between the two modes is the necessity to reconstruct the π^0 for the $K^-\pi^+\pi^0$ decay. As previously described, the π^0 Monte Carlo added simulated photon showers to real events and then reconstructed these events with the usual π^0 finding programs. These π^0 efficiencies were then combined with the D*+ Monte Carlo to yield the ratio $\varepsilon(K^-\pi^+\pi^0)/\varepsilon(K^-\pi^+) = 0.25\pm0.04$, for our D^0 energy spectrum. Taking the number of events observed in each decay mode with the relative detection efficiency, we deduce that $B(D^0\to K^-\pi^+\pi^0)/B(D^0\to K^-\pi^+) = 4.3\pm1.4$. Combining this with the currently accepted value for

the $K^-\pi^+$ mode of 2.4±0.4% [1], yields a measurement of

$B(D^0 \to K^-\pi^+\pi^0) = 10.3 \pm 3.7\%$.

VIII. $K^-\rho^+$, $\bar{K}^{*0}\pi^0$, $K^{*-}\pi^+$, AND NON-RESONANT FRACTIONS

A. DALITZ PLOTS

Dalitz plots are useful for finding resonant contributions to three-body decays. If a particle decays according to phase space, the density of events per unit area will be uniform. Resonances show up as a non-uniform density.

Two Dalitz plots are shown in Figure 57. The square of the $K^-\pi^+$ mass is plotted against the square of the $\pi^+\pi^0$ mass in both cases. The first plot shows the D^0 signal and was obtained by chosing the 82 events with a $D^{*+} - D^0$ mass difference between 0.1440 and 0.1470 GeV/c^2. All other cuts are the same as for the 4-fold probability mass difference peak discussed previously. The fit described in the previous chapter yields 45 signal events (55%) and 37 background events (45%) in this mass difference range. The error on the background fraction of events is estimated to be ±5%. There are 31 $D^0 \rightarrow K^-\pi^+\pi^0$ decays and 51 $\bar{D}^0 \rightarrow K^+\pi^-\pi^0$ decays.

The second Dalitz plot is of the background. For this plot the $K^-\pi^+\pi^0\pi^+ - K^-\pi^+\pi^0$ mass difference was chosen to lie below 0.143 GeV/c^2, or between 0.148 and 0.170 GeV/c^2, to exclude the real charm signal.

A few points are outside the kinematic boundaries drawn on both Dalitz plots, because we did not constrain the $K^-\pi^+\pi^0$ mass to exactly equal the D^0 mass.

B. MAXIMUM LIKELIHOOD FITS TO THE DALITZ PLOTS

The density of the background Dalitz plot varies linearly with $M^2(K^-\pi^+)$ ($E(\pi^0)$ in the D^0 center-of-mass), as expected for uniform phase space, given the energy dependence of our π^0 efficiency in the lab. The background density gave a good fit to the equation to $1 - X_2(M^2(K^-\pi^+)-1.5)$, where the value of X_2 was found to be 0.58. If our π^0 reconstruction efficiency were independent of energy, X_2 would equal zero. The ρ and K^* contributions to this background-estimate are observed to be negligible.

Adjusting for the relative π^0 efficiency measured in the background Dalitz plot, we performed a maximum likelihood fit [53] to the $D^0 \to K^-\pi^+\pi^0$ Dalitz plot allowing background, non-resonant, $K^-\rho^+$, $K^*-\pi^+$, and $\bar{K}^{*0}\pi^0$ contributions. Each vector meson contribution was described by a Breit-Wigner plus the appropriate decay angular distribution. The results are shown in Table 9, as are the corresponding MARK II results [2]. Interference

effects are small compared to the quoted errors, and are neglected.

We find that half of our $D^0 \to K^-\pi^+\pi^0$ decays are into non-resonant $K^-\pi^+\pi^0$, one third are into $K^-\rho^+$, and little is into $K^*\pi$. The relative non-resonant and $K^-\rho^+$ contributions are most easily seen in the projection of the Dalitz plot onto the $M^2_{\pi^+\pi^0}$ axis. In Figure 58 we plot that distribution for $|\cos\theta| > 0.5$, where θ is the angle of either pion relative to the kaon direction in the $\pi\pi$ center-of-mass. For $D^0 \to K^-\rho^+$, one expects a $\cos^2\theta$ dependence, because the ρ^+ spin is 1 and the D^0, K^- and pion spins are 0. Therefore, the sample with $|\cos\theta| > 0.5$ should contain 7/8 of the $K^-\rho^+$ signal but only 1/2 of the non-resonant contribution (signal plus background). The upper curve in Figure 58 represents the fit to the entire Dalitz plot with the $|\cos\theta| > 0.5$ cut. The lower curve is also for $|\cos\theta| > 0.5$, but excludes the ρ term in the fit.

TABLE 16. $D^0 \to K^-\pi^+\pi^0$ DECAY CONTRIBUTIONS

Channel	Fraction of $D^0 \to K^-\pi^+\pi^0$ Decays		Branching Ratio	
	E516	MARK II	E516	MARK II
$K^-\rho^+$	$0.31^{+.20}_{-.14}$	$0.85^{+.11(.09)}_{-.15(.10)}$	$3.2^{+2.3}_{-1.8}$%	$7.2^{+3.0}_{-3.1}$%
$\bar{K}^{*0}\pi^0$	$0.06^{+.09}_{-.06}$	$0.11^{+.14(.10)}_{-0.9(.10)}$	$0.9^{+1.4}_{-0.9}$%	$1.4^{+2.3}_{-1.4}$%
$K^{*-}\pi^+$	$0.11^{+.12}_{-.08}$	$0.07^{+.07(.05)}_{-.06(.02)}$	$3.4^{+3.9}_{-2.8}$%	$1.8^{+2.3}_{-1.8}$%
Non-Resonant Decays	$0.51 \pm .22$	$0.00^{+.21(.05)}_{-.00(.00)}$	5.2 ± 2.9%	<2.4%
Total $K^-\pi^+\pi^0$	1.00	1.00	10.3 ± 3.7%	8.5 ± 3.2%

Note that the 45% background contribution determined in the $D^{*+}-D^0$ mass plot has been excluded from the Non-Resonant Decay category. Also observe that the K* channel branching ratios have been adjusted for $K^* \to K\pi$ branching ratios, which are derived from isospin conservation and Clebsch-Gordon coefficients on page 120. In places where an error is quoted in parentheses, the first error is statistical and the second error is systematic.

IX. DISCUSSION OF RESULTS

One of the fundamental problems in the study of D decays is to determine the relative importance of the decay mode in which the light quark is a spectator and the mode in which a W boson is exchanged between the light and charmed quarks. (D^0 decay diagrams appear in Figure 1.) If the W-exchange decay mode dominates, the D^0 lifetime is shorter than the D^+, because the D^+ would have to decay by annihilation, which is Cabibbo-suppressed, or by the non-dominant spectator mode. (W-exchange is completely ruled out for the D^+ by charge conservation.) The W-exchange diagram requires an I=1/2 final state; the isospin of the spectator diagram final state is an unknown mixture of I=1/2 and I=3/2. One I=1/2 quark contributes to the isospin of the W-exchange diagram, while three I=1/2 quarks contribute to the isospin of the spectator quark diagram. A dominant I=1/2 final state leads to D^0 branching ratio predictions which follow from isospin and the fact that kaons and K*'s are I=1/2

states and pions and rhos are I=1 states. If the final state of the D^0 decay is I=1/2, its isospin decomposition is:

$$|I, I_3\rangle = |1/2, 1/2\rangle = \sqrt{2/3}|K^-\pi^+\rangle - \sqrt{1/3}|\bar{K}^0\pi^0\rangle$$

$$|I, I_3\rangle = |1/2, 1/2\rangle = \sqrt{2/3}|K^{*-}\pi^+\rangle - \sqrt{1/3}|\bar{K}^{*0}\pi^0\rangle$$

$$|I, I_3\rangle = |1/2, 1/2\rangle = \sqrt{2/3}|K^-\rho^+\rangle - \sqrt{1/3}|\bar{K}^0\rho^0\rangle$$

Dividing the squares of the appropriate Clebsch-Gordon coefficients leads to the expectation that:

$$\frac{B(D^0 \to K^-\pi^+)}{B(D^0 \to \bar{K}^0\pi^0)} = \frac{B(D^0 \to K^{*-}\pi^+)}{B(D^0 \to \bar{K}^{*0}\pi^0)} = \frac{B(D^0 \to K^-\rho^+)}{B(D^0 \to \bar{K}^0\rho^0)} = 2.$$

Existing data for the first two channels are consistent with this hypothesis, but the measurements for the last ratio are $B(D^0 \to K^-\rho^0) = 7.2^{+3.0}_{-3.1}\%$ and $B(D^0 \to K^0\rho^0) = 0.1^{+0.6}_{-0.1}\%$ Combining our $K^-\rho^+$ fraction with our $D^0 \to K^-\pi^+\pi^0$ branching ratio gives $B(D^0 \to K^-\rho^+) = 3.2^{+2.3}_{-1.8}\%$. This is about half the MARK II value and is 1.4 standard deviations away from $2 \cdot B(D^0 \to \bar{K}^0\rho^0)$, the I=1/2 expectation.

In summary, we have observed $D^0 \to K^-\pi^+\pi^0$ and $K^-\pi^+$ in D^{*+} events. From these we have measured the

quotient of branching ratios to be 4.3 ± 1.4, which leads to a $K^-\pi^+\pi^0$ branching ratio of $10.3 \pm 3.7\%$. From the Dalitz plot analysis we have measured the quasi-two-body and non-resonant three-body contributions to $D^0 \to K^-\pi^+\pi^0$. The fractions and branching ratios are given in Table 9. We see a large non-resonant decay fraction (51%), and a $K^-\rho^+$ branching ratio which is compatible with I=1/2 dominance.

APPENDIX -- FIGURES

Figure 40. Mass of All Photon Pairs in Which Each Photon Can Be Used to Form at Most One π^0 and One Photon is from the SLIC and One From the Outriggers. The Data is from a Typical 15000 Event 170 GeV Tape Segment.

Figure 41. Mass of All Photon Pairs in Which Each Photon Can Be Used to Form at Most One π^0 and Both Photons are from the Outriggers. The Data is from a Typical 15000 Event 170 GeV Tape Segment.

Figure 42. Mass of All Photon Pairs in Which Each Photon Can Be Used to Form at Most One π^0 and One Photon is from the SLIC and One from a e^+e^- pair. The Data is from a Typical 15000 Event 170 GeV Tape Segment.

Figure 43. $\omega(783) \rightarrow \pi^+\pi^-\pi^0$

Figure 44. $\phi(1020) \rightarrow K^0_L K^0_S$

Figure 45. Monte Carlo $D^{*+}-D^0$ Mass Plot ($D^0 \rightarrow K^-\pi^+$)

Figure 46. Monte Carlo $D^{*+}-D^0$ Mass Plot ($D^0 \rightarrow K^-\pi^+\pi^0$)

Figure 47. $D^{*+}-D^0$ Mass Plot ($D^0 \rightarrow K^-\pi^+$)

Figure 48. $D^{*+}-D^0$ Mass Plot ($D^0 \rightarrow K^-\pi^+\pi^0$, PRPIZ2 $>$ 0.8)

Figure 49. $D^{*+}-D^0$ Mass Plot ($D^0 \rightarrow K^-\pi^+\pi^0$)

Figure 50. $D^{*+}-D^0$ Mass Plot ($D^0 \rightarrow K^-\pi^+\pi^0$, No E($D^{*+}$) Cut)

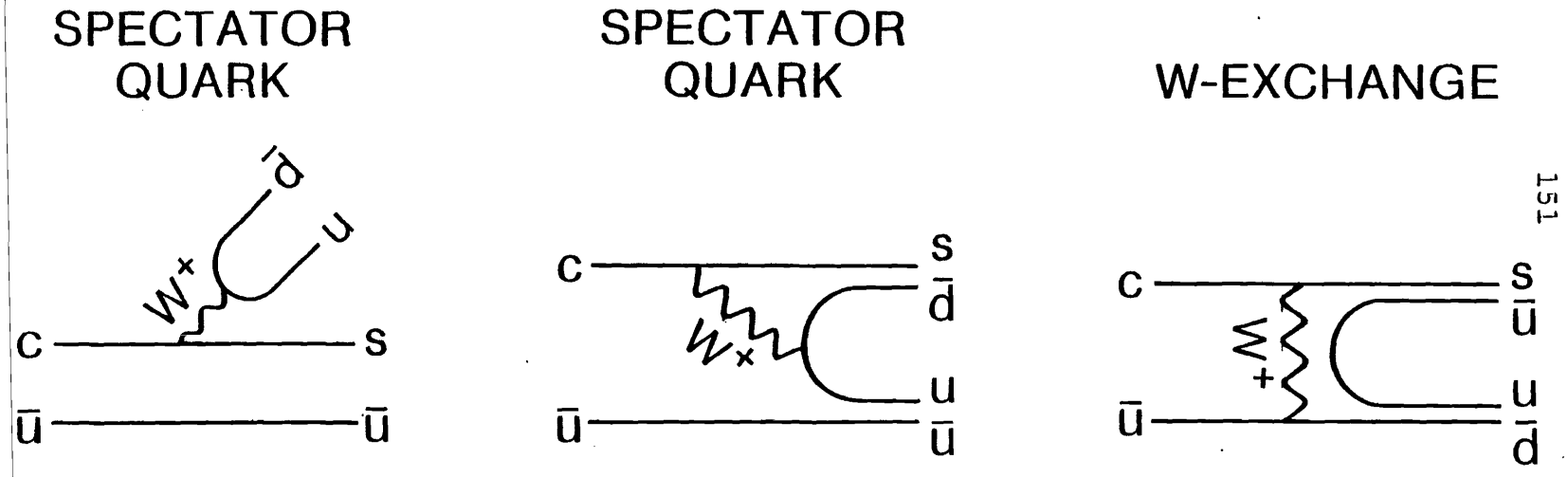

Figure 1. D^{O} Decay Diagrams

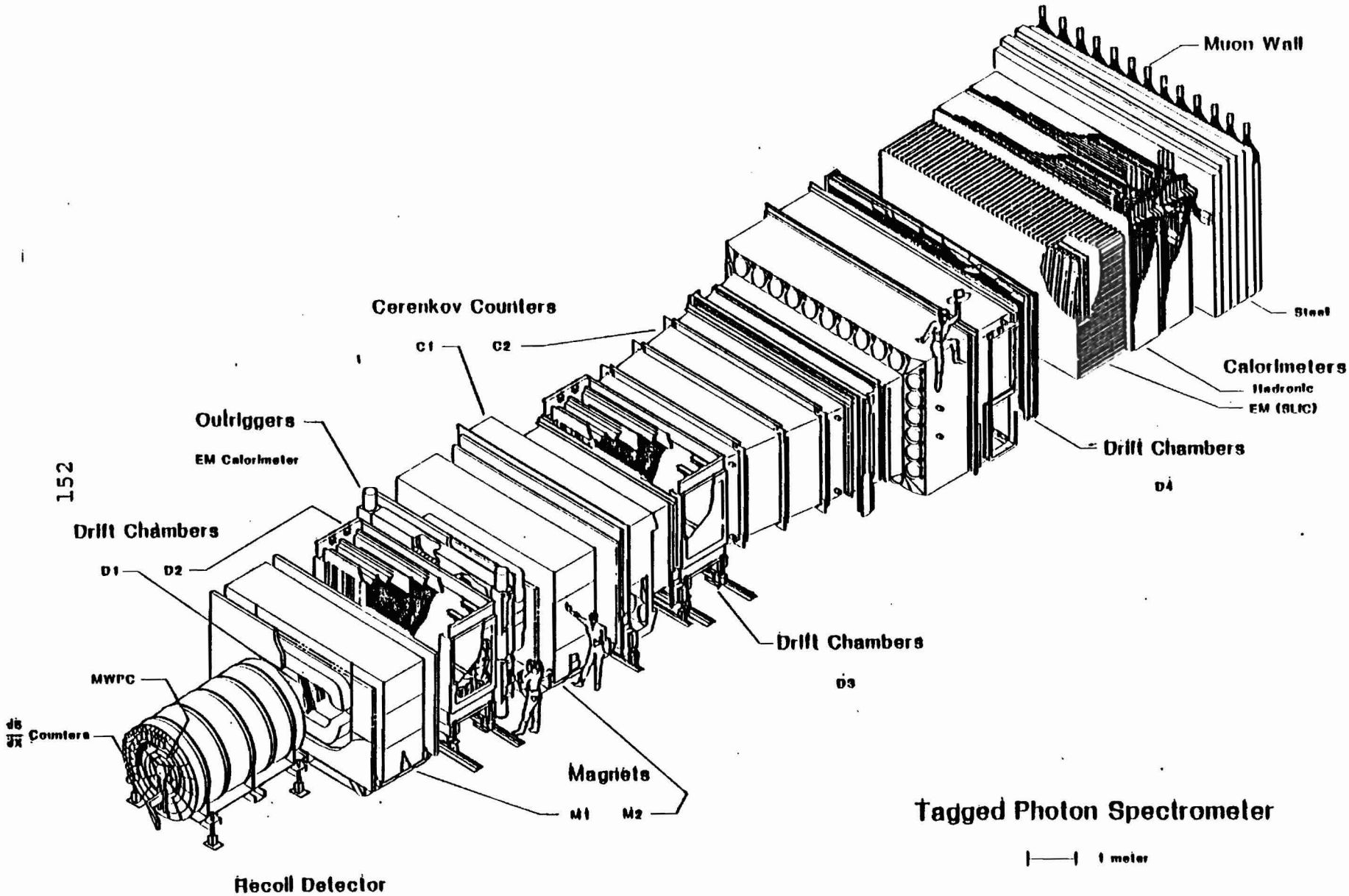
Muon Wall
Steel
Calorimeters
Hadronic
EM (SLIC)
Cerenkov Counters
C1
C2
Outriggers
EM Calorimeter
Drift Chambers
D4
Drift Chambers
D1
D2
Drift Chambers
D3
MWPC
dE/dx Counters
Magnets
M1
M2
Recoil Detector
Tagged Photon Spectrometer
1 meter

Figure 2

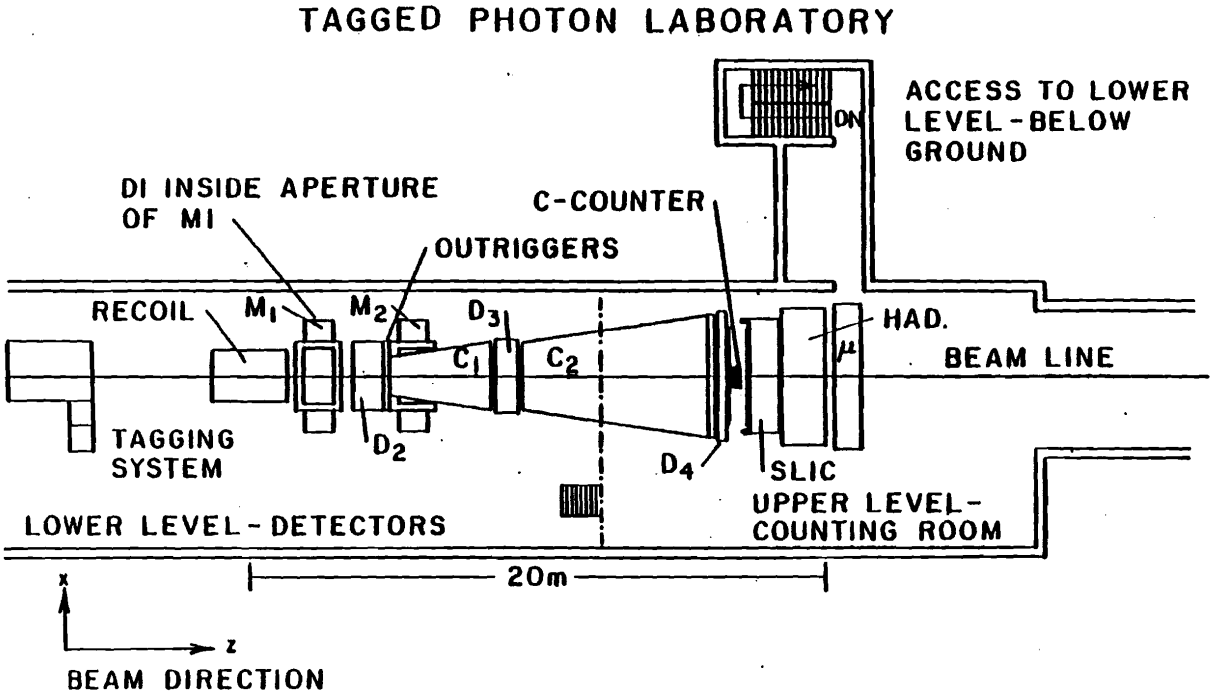
TAGGED PHOTON LABORATORY
ACCESS TO LOWER LEVEL - BELOW GROUND
ON
DI INSIDE APERTURE OF MI
C-COUNTER
OUTRIGGERS
RECOIL
M_1
M_2
D_3
C_1
C_2
HAD.
μ
BEAM LINE
TAGGING SYSTEM
D_2
D_4
SLIC
LOWER LEVEL - DETECTORS
UPPER LEVEL - COUNTING ROOM
20m
x
z
BEAM DIRECTION

Figure 3

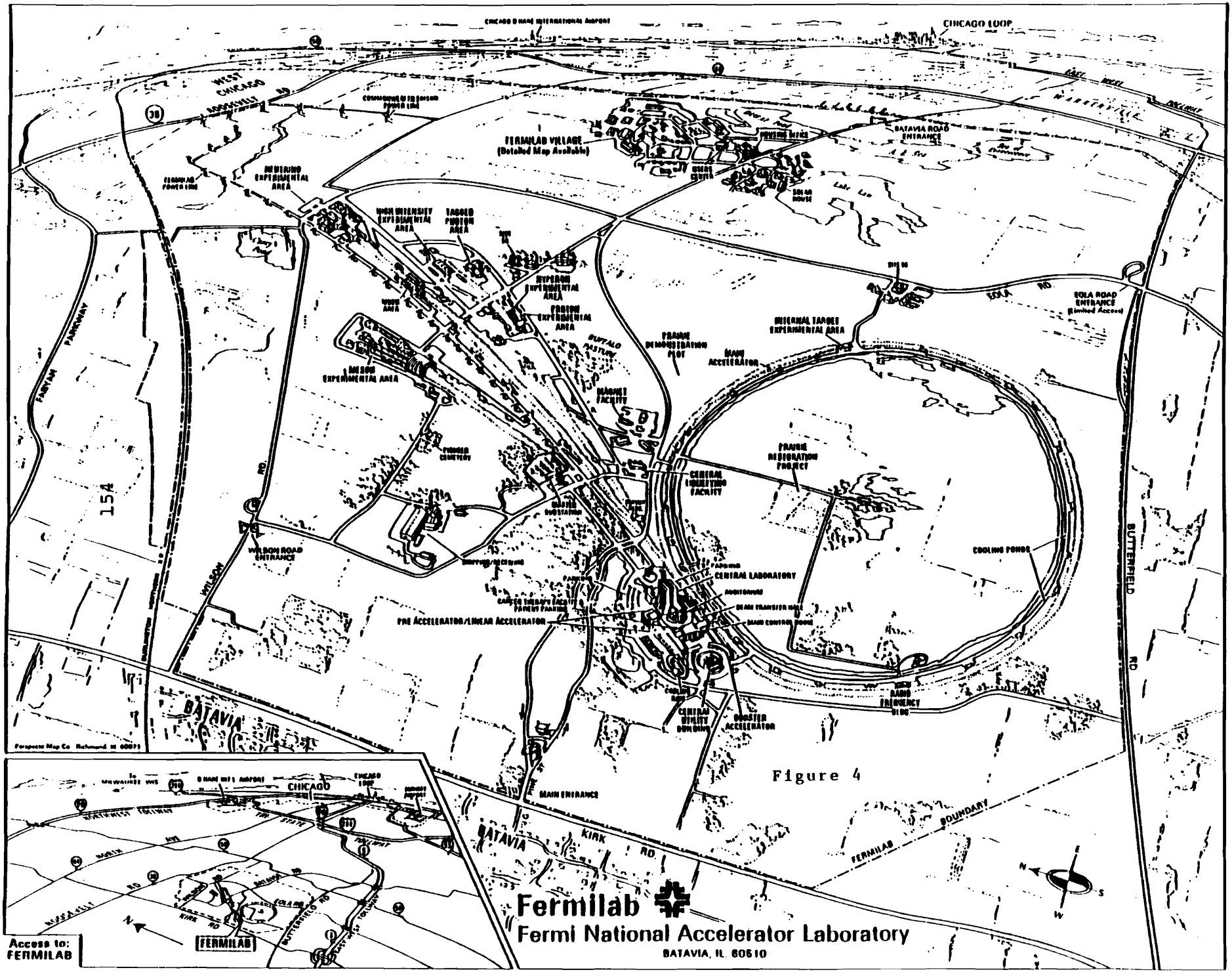
CHICAGO LOOP
FERMILAB VILLAGE
(Detailed Map Available)
BATAVIA ROAD ENTRANCE
MUON EXPERIMENTAL AREA
HIGH INTENSITY EXPERIMENTAL AREA
TAGGED PHOTON AREA
DIFFRACTION EXPERIMENTAL AREA
PROTON EXPERIMENTAL AREA
BUFFALO PASTURE
MUON EXPERIMENTAL AREA
MAGNET FACILITY
PRAIRIE DEMONSTRATION PLOT
MAIN ACCELERATOR
ELEVATED TARGET EXPERIMENTAL AREA
SOLA ROAD ENTRANCE
(Limited Access)
PRAIRIE RESTORATION PROJECT
GENERAL EQUIPMENT FACILITY
PRAIRIE CEMETERY
WILSON ROAD ENTRANCE
CENTRAL LABORATORY
COOLING PONDS
PRE ACCELERATOR/LINEAR ACCELERATOR
BEAM TRANSFER HALL
MAIN CONTROL ROOM
CENTRAL UTILITY BUILDING
BOOSTER ACCELERATOR
RADIO FREQUENCY BLDG
MAIN ENTRANCE
FABIAN PARKWAY
WILSON
154
RD.
BUTTERFIELD RD
BATAVIA
KIRK RD
FERMILAB BOUNDARY
CHICAGO
FERMILAB
Access to:
FERMILAB
Fermilab
Fermi National Accelerator Laboratory
BATAVIA, IL 60510

Figure 4

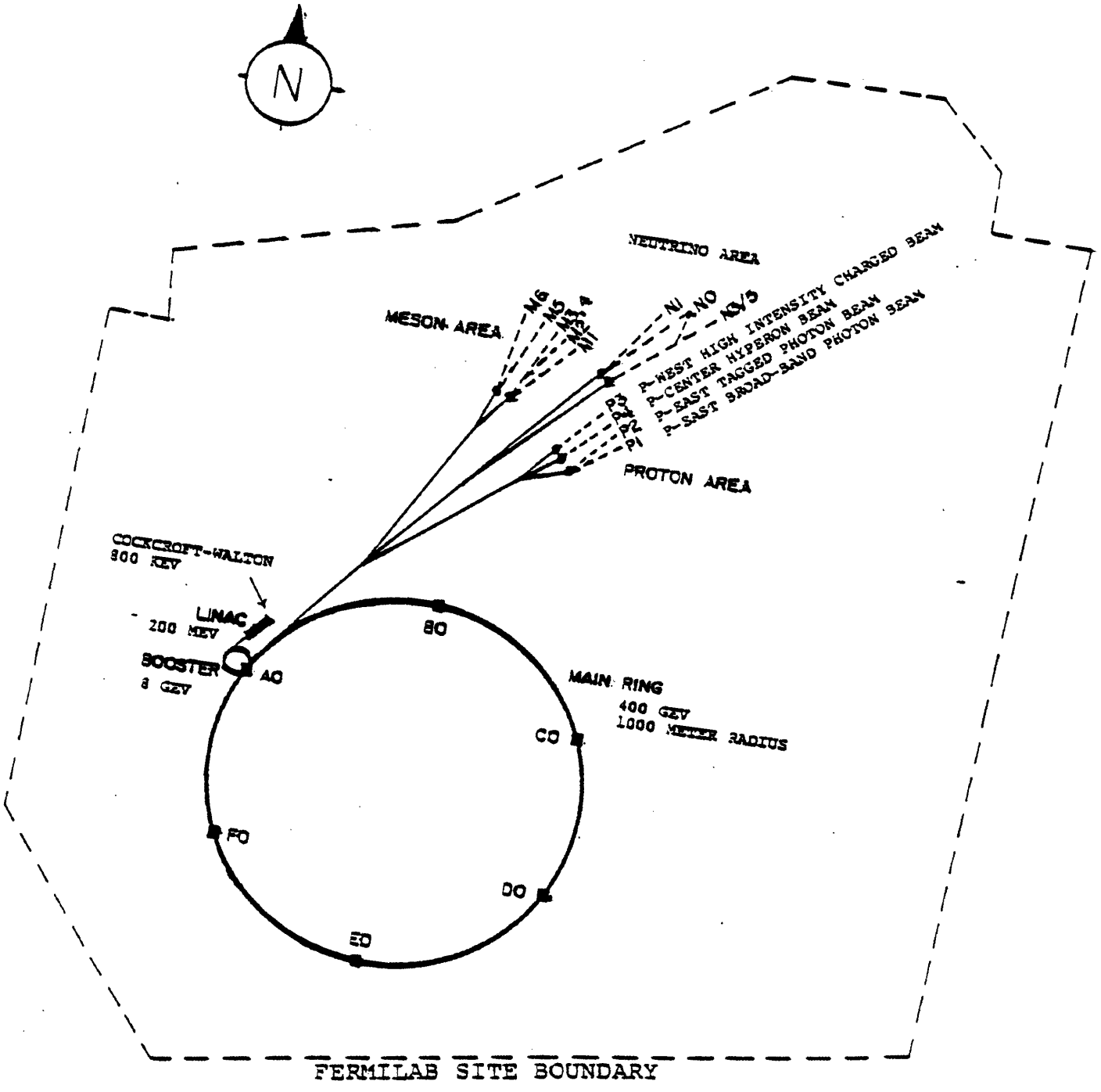
N
NEUTRINO AREA
MESON AREA
M6
M5
M3, 4
M2
M1
N1
NO
N3/5
P-WEST HIGH INTENSITY CHARGED BEAM
P-CENTER HYPERON BEAM
P-EAST TAGGED PHOTON BEAM
P-EAST BROAD-BAND PHOTON BEAM
P3
P4
P2
P1
PROTON AREA
COCKCROFT-WALTON
900 KEV
LINAC
200 MEV
BOOSTER
8 GEV
AO
BO
CO
DO
EO
FO
MAIN RING
400 GEV
1000 METER RADIUS
FERMILAB SITE BOUNDARY

Figure 5

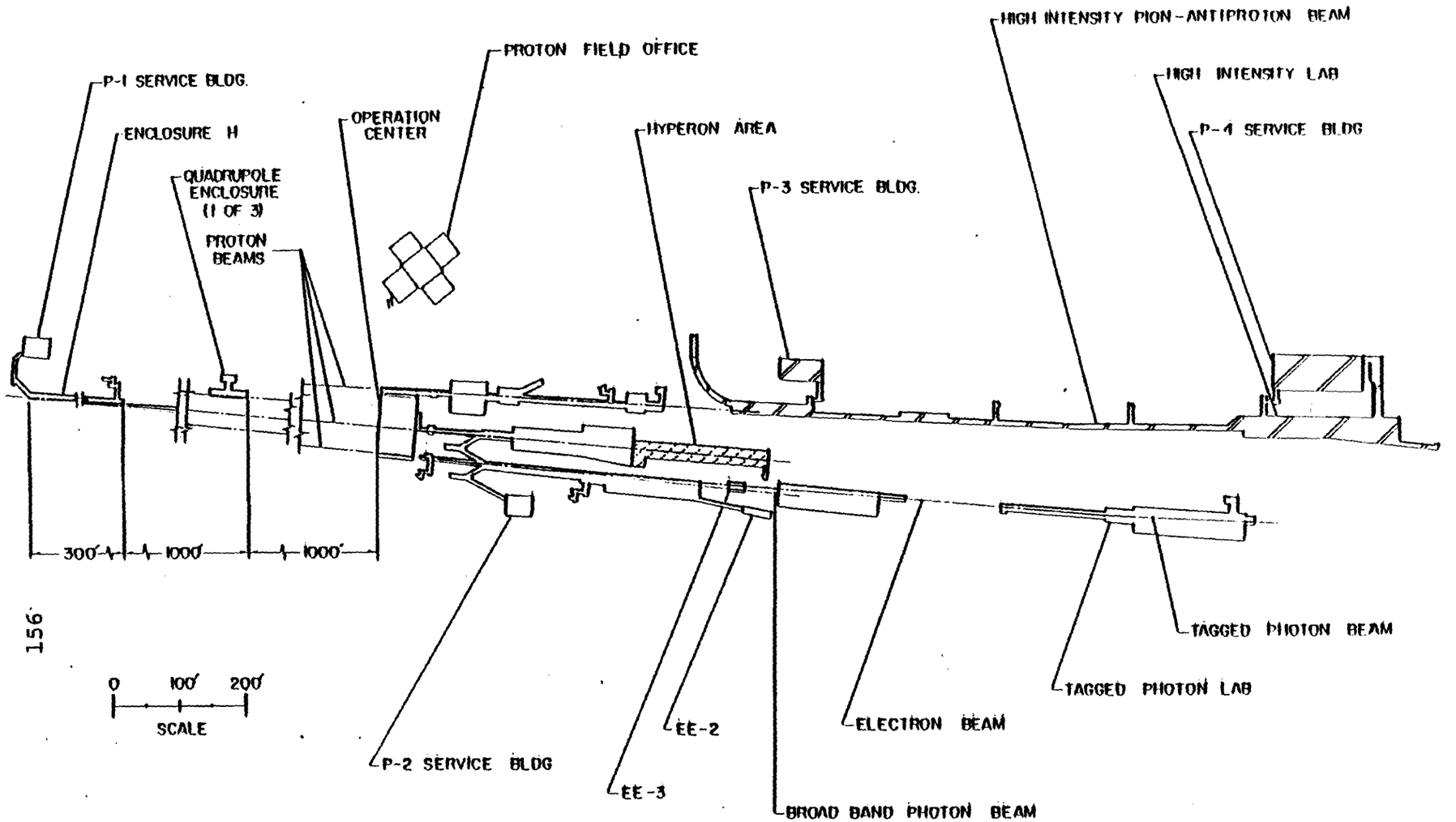

Figure 6. The Proton Experimental Area

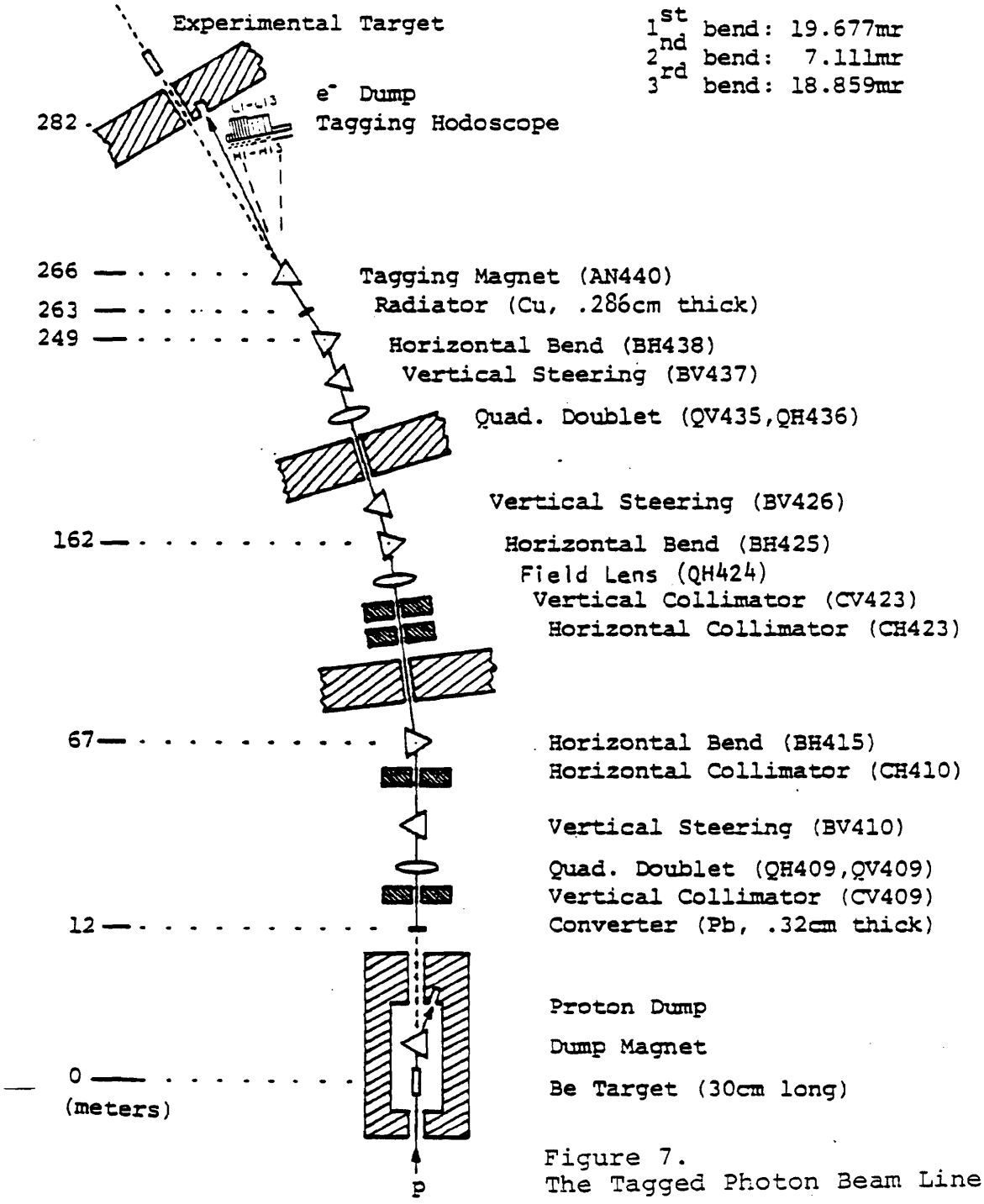

Figure 7.
The Tagged Photon Beam Line

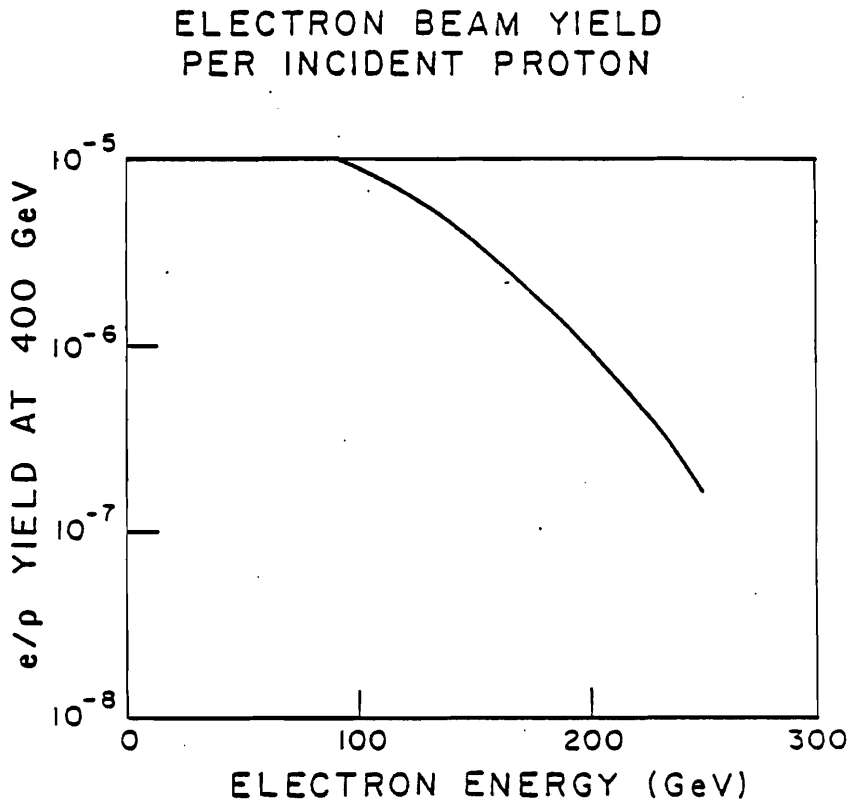
ELECTRON BEAM YIELD
PER INCIDENT PROTON
e/p YIELD AT 400 GeV
10^-5
10^-6
10^-7
10^-8
0
100
200
300
ELECTRON ENERGY (GeV)

Figure 8

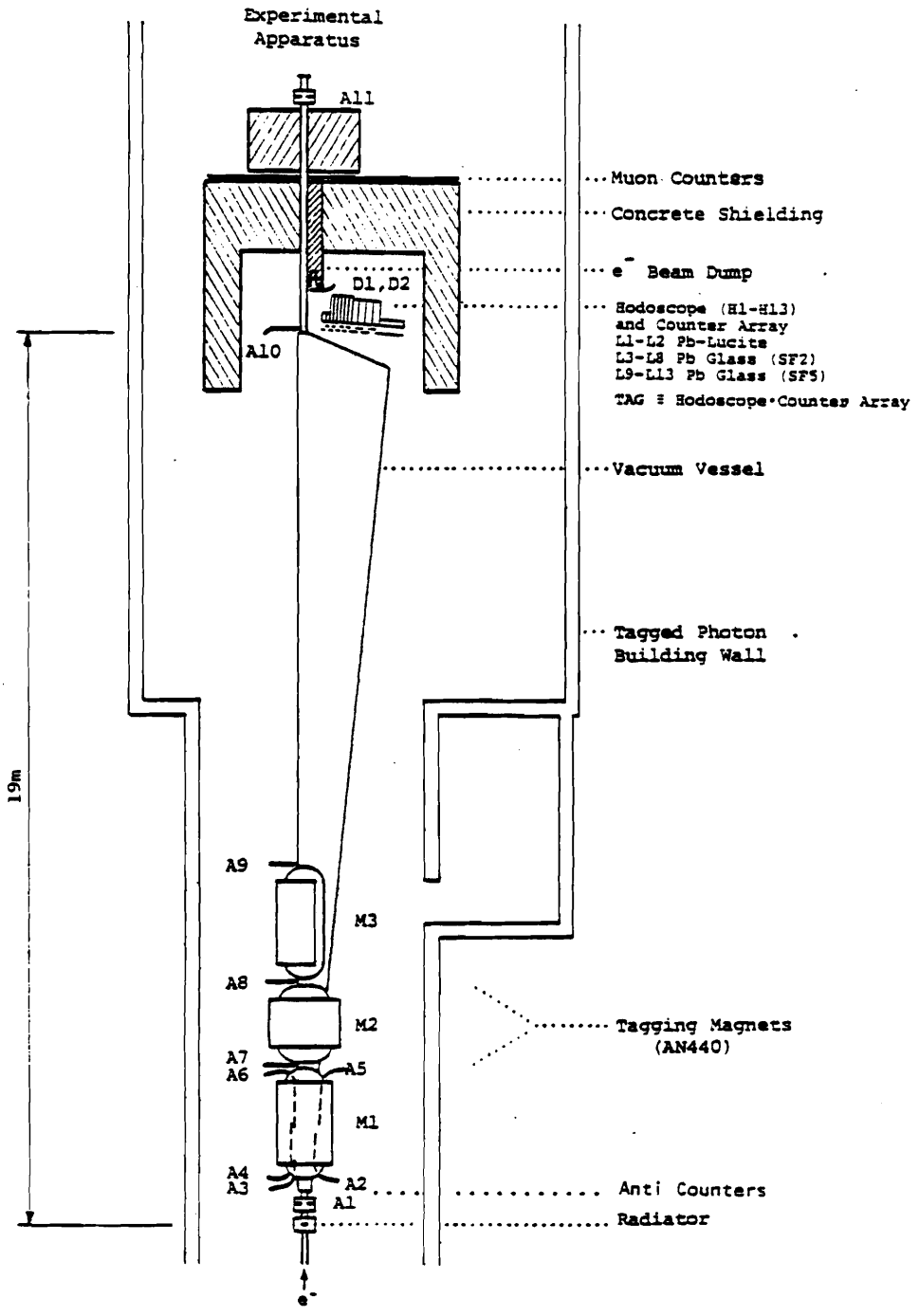

Figure 9. System for Tagging Photon Energies

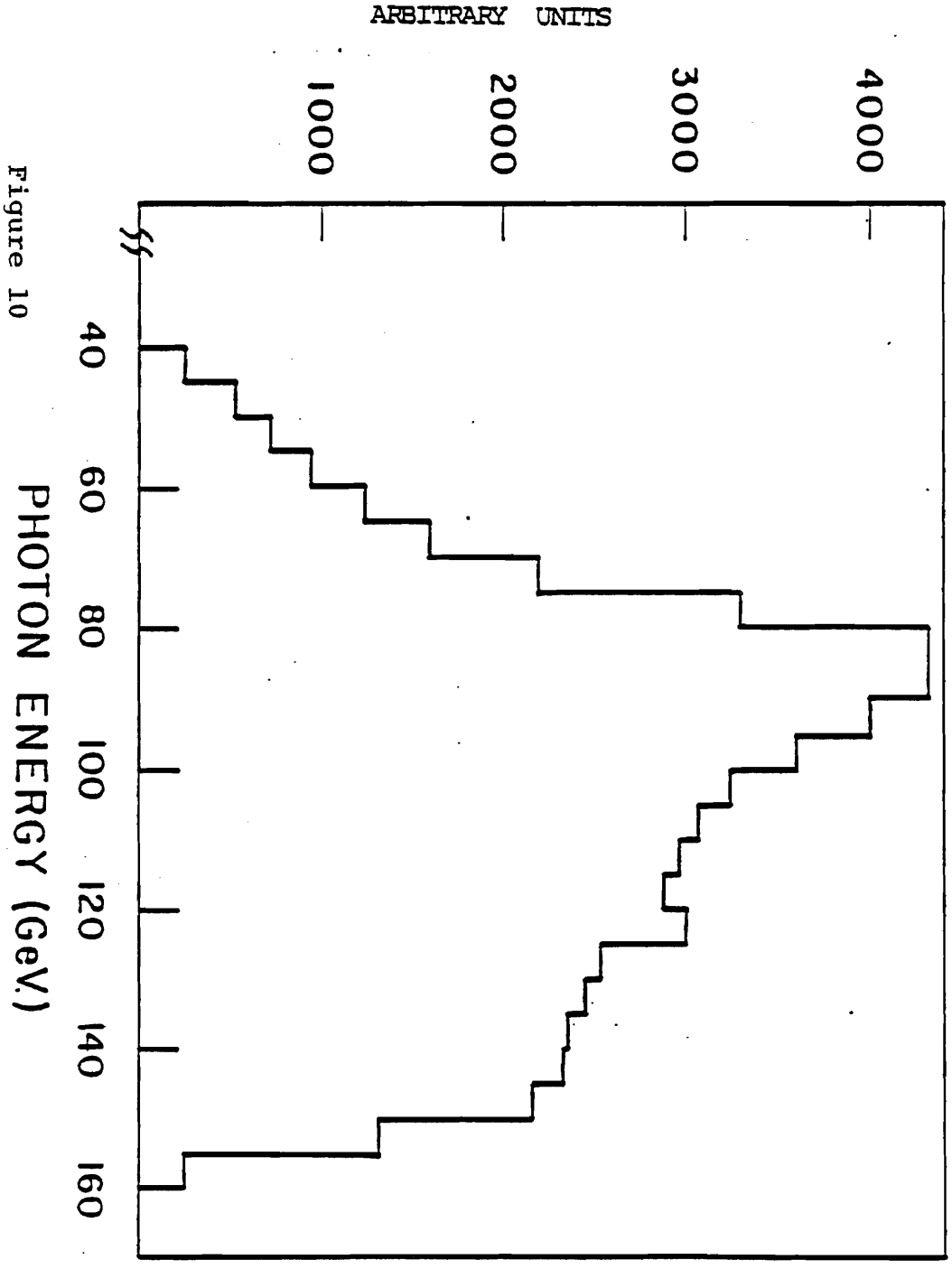
ARBITRARY UNITS
1000
2000
3000
4000
40
60
80
100
120
140
160
PHOTON ENERGY (GeV.)

Figure 10

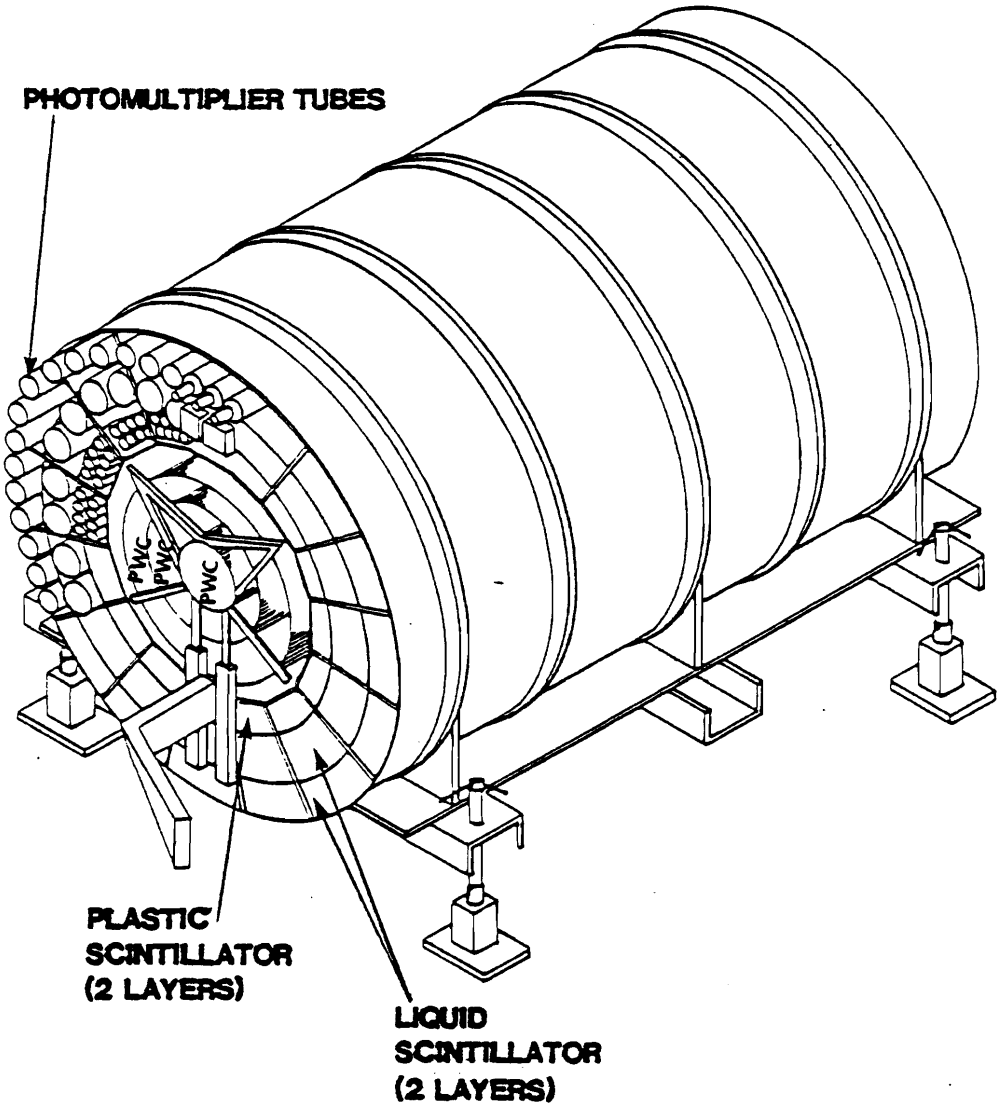

RECOIL DETECTOR

Figure 11

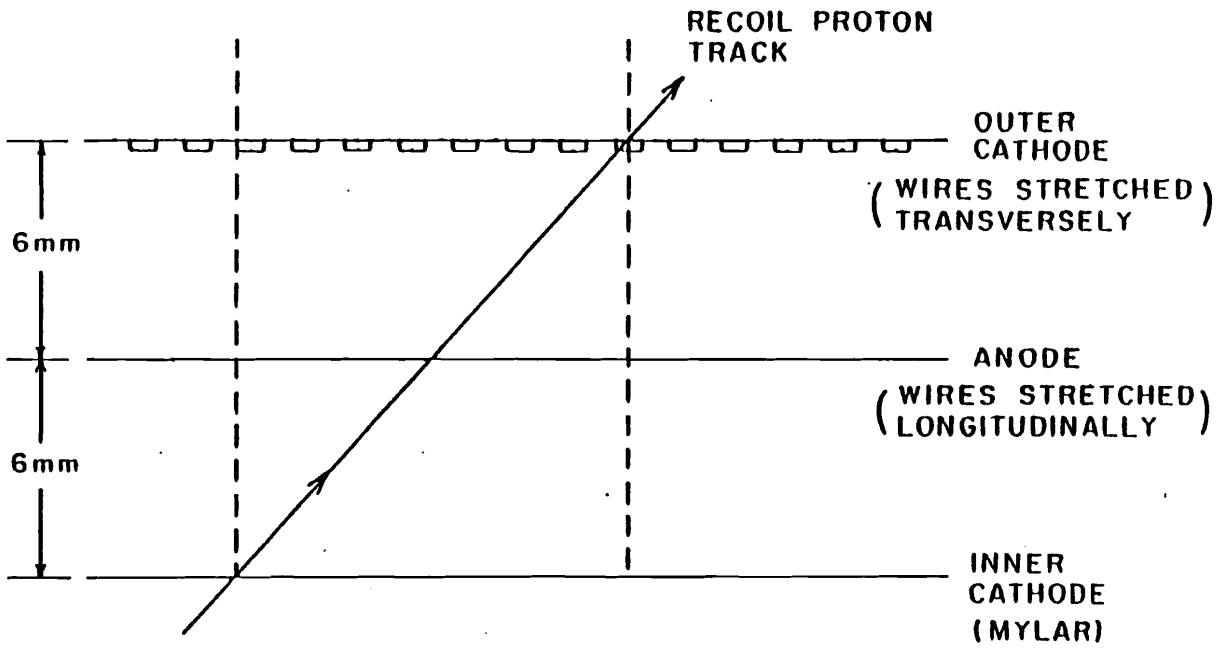
RECOIL PROTON
TRACK
OUTER
CATHODE
(WIRES STRETCHED
TRANSVERSELY)
6mm
ANODE
(WIRES STRETCHED
LONGITUDINALLY)
6mm
INNER
CATHODE
(MYLAR)
PWC CHAMBER
LONGITUDINAL CROSS SECTION

Figure 12

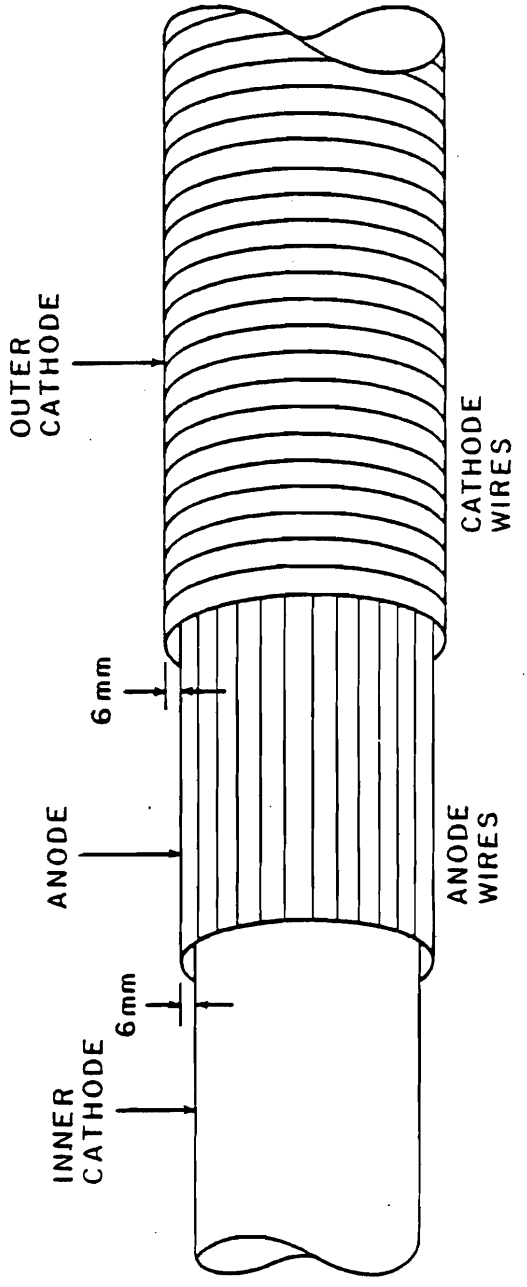

CUTAWAY VIEW OF PWC CHAMBER

Figure 13

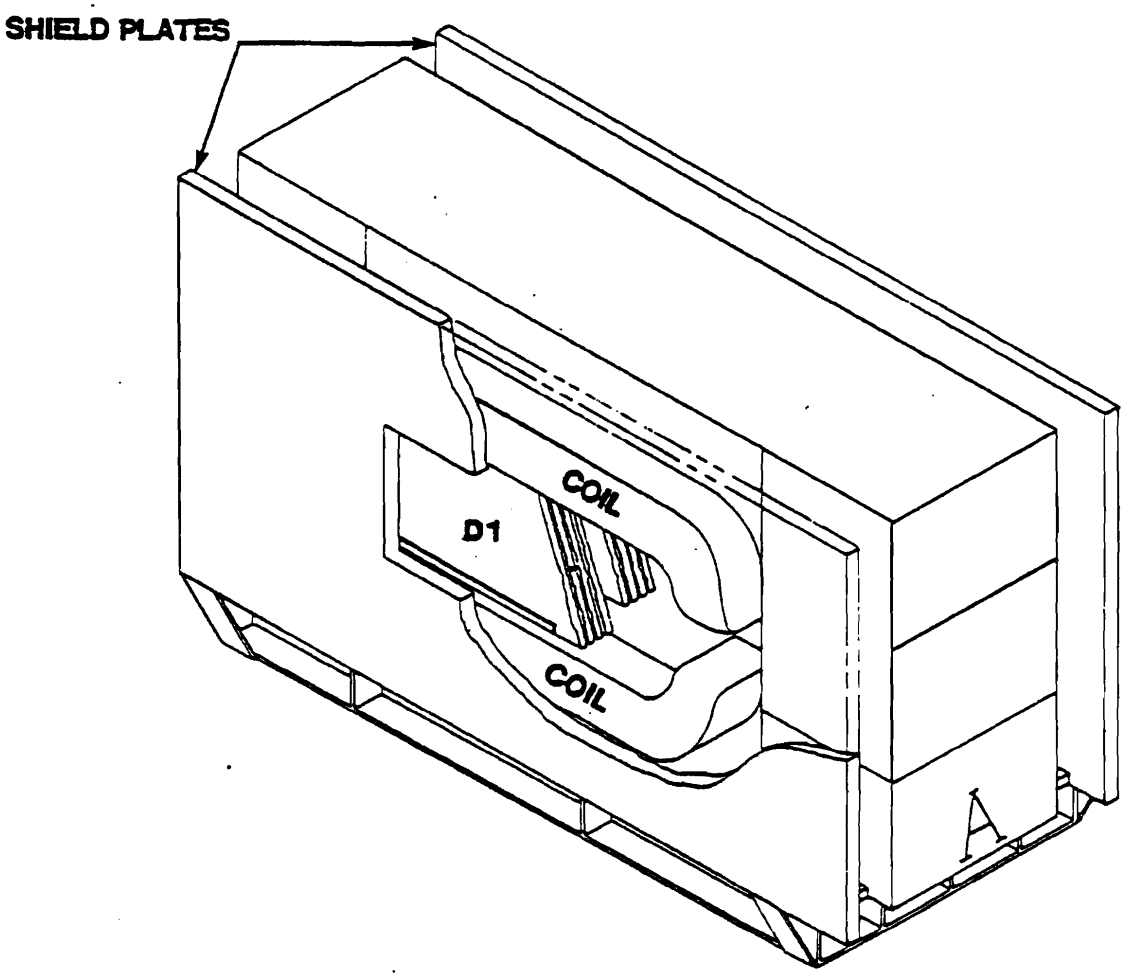

**ANALYZING MAGNET M1
AND DRIFT CHAMBER D1**

Figure 14. Akhennaten

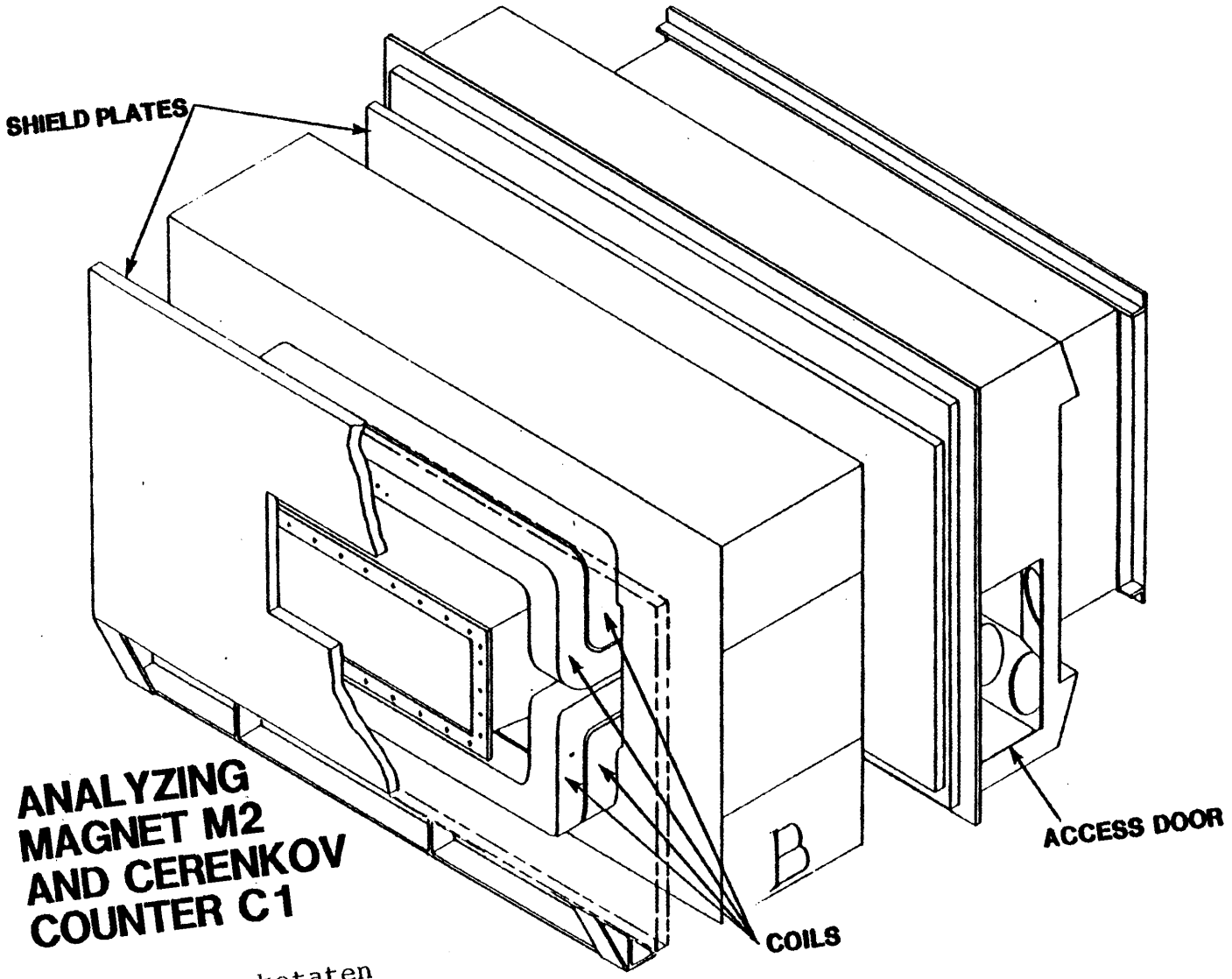

Figure 15. Beketaten

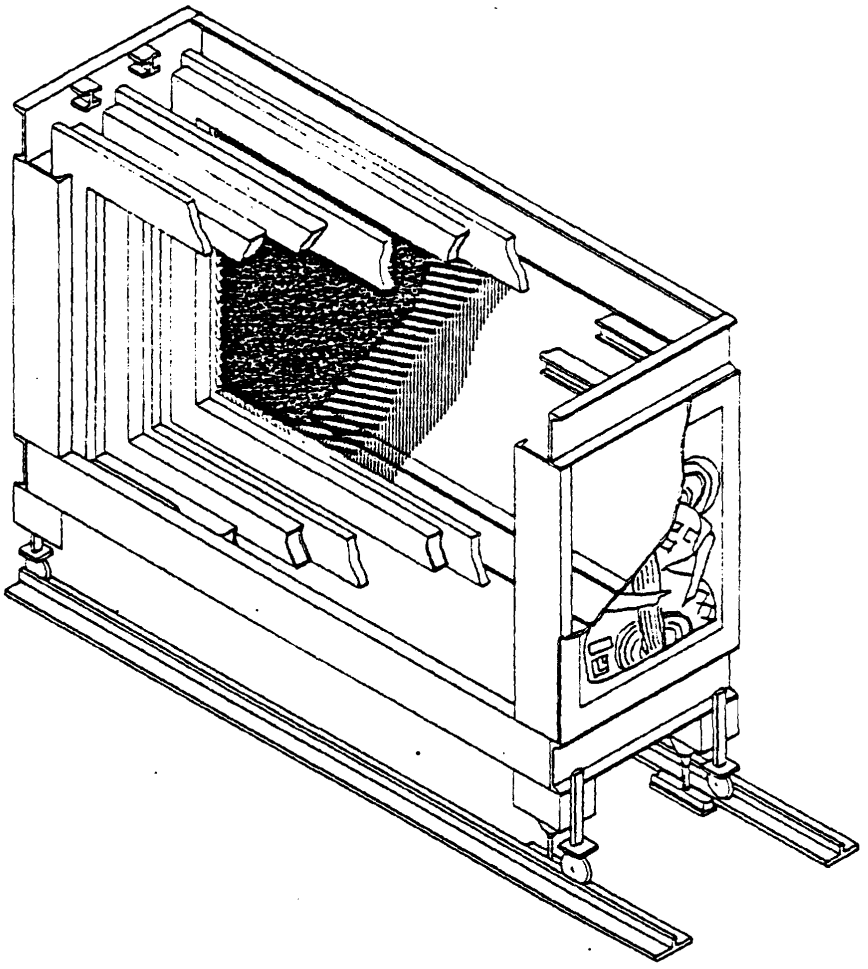

Figure 16. Drift Chamber D2

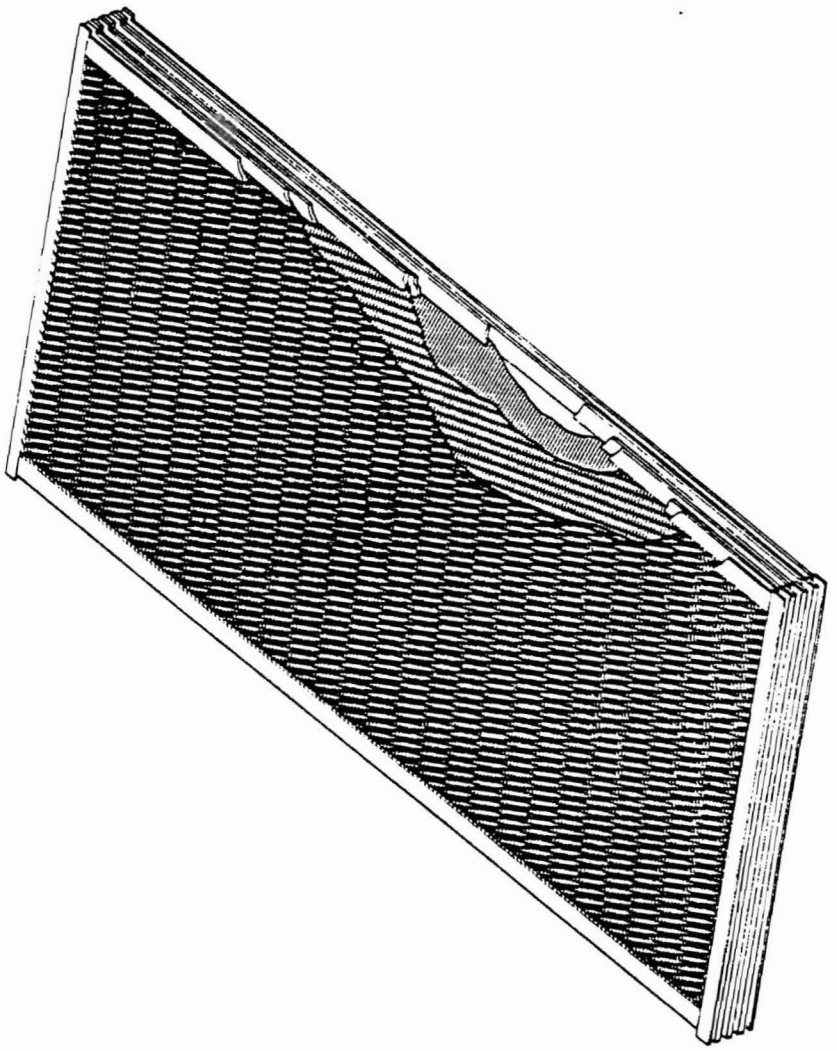

Figure 17. Drift Chamber D4

D1 ASSEMBLY

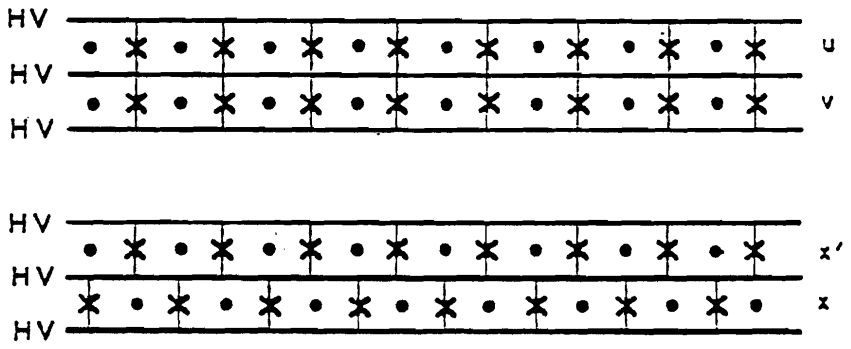

✕ - FIELD WIRES

• - SENSE WIRES

HV - HIGH VOLTAGE FIELD PLANES

D2-D4 ASSEMBLIES

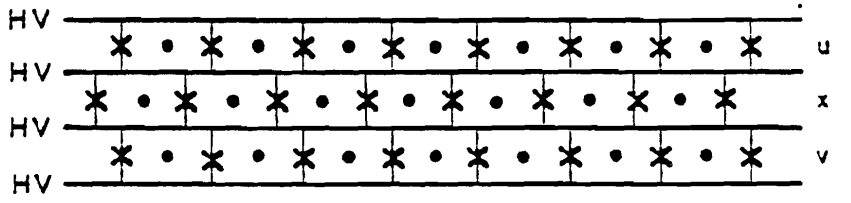

DRIFT CHAMBER CELL STRUCTURE

Figure 18

Figure 19

DRIFT CHAMBER SYSTEM (TOP VIEW)
(TOTAL OF 29 PLANES)

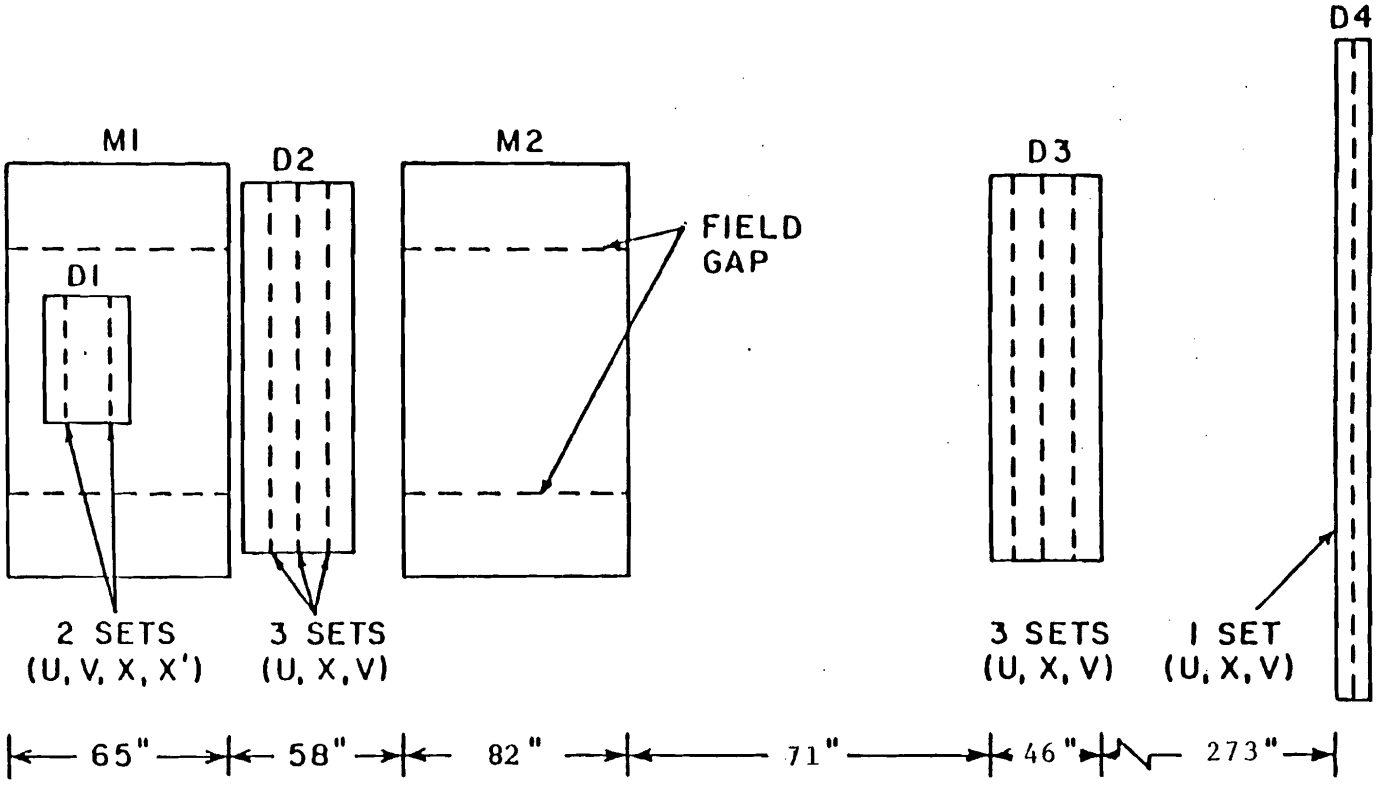

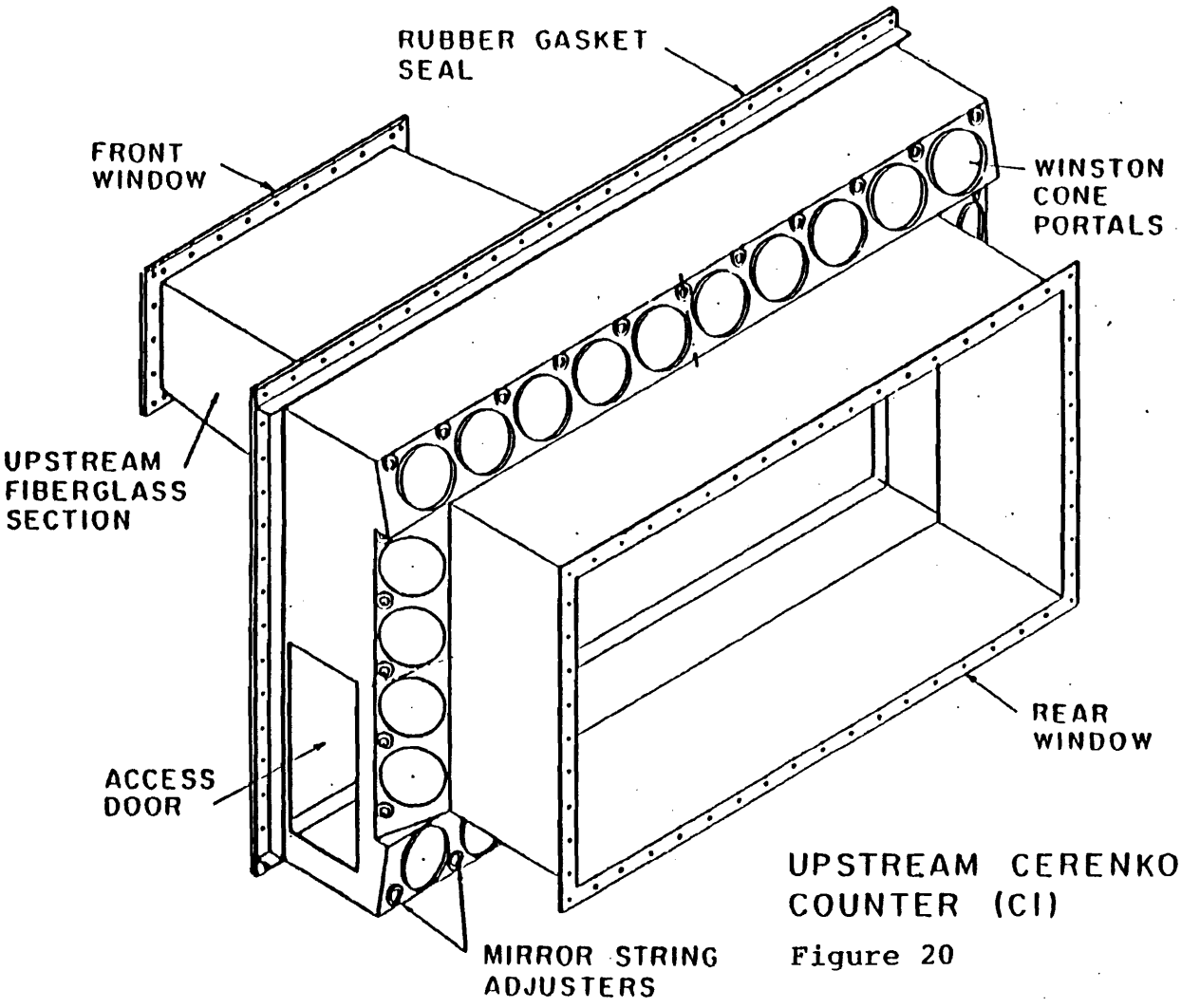

UPSTREAM CERENKOV COUNTER (C1)

Figure 20

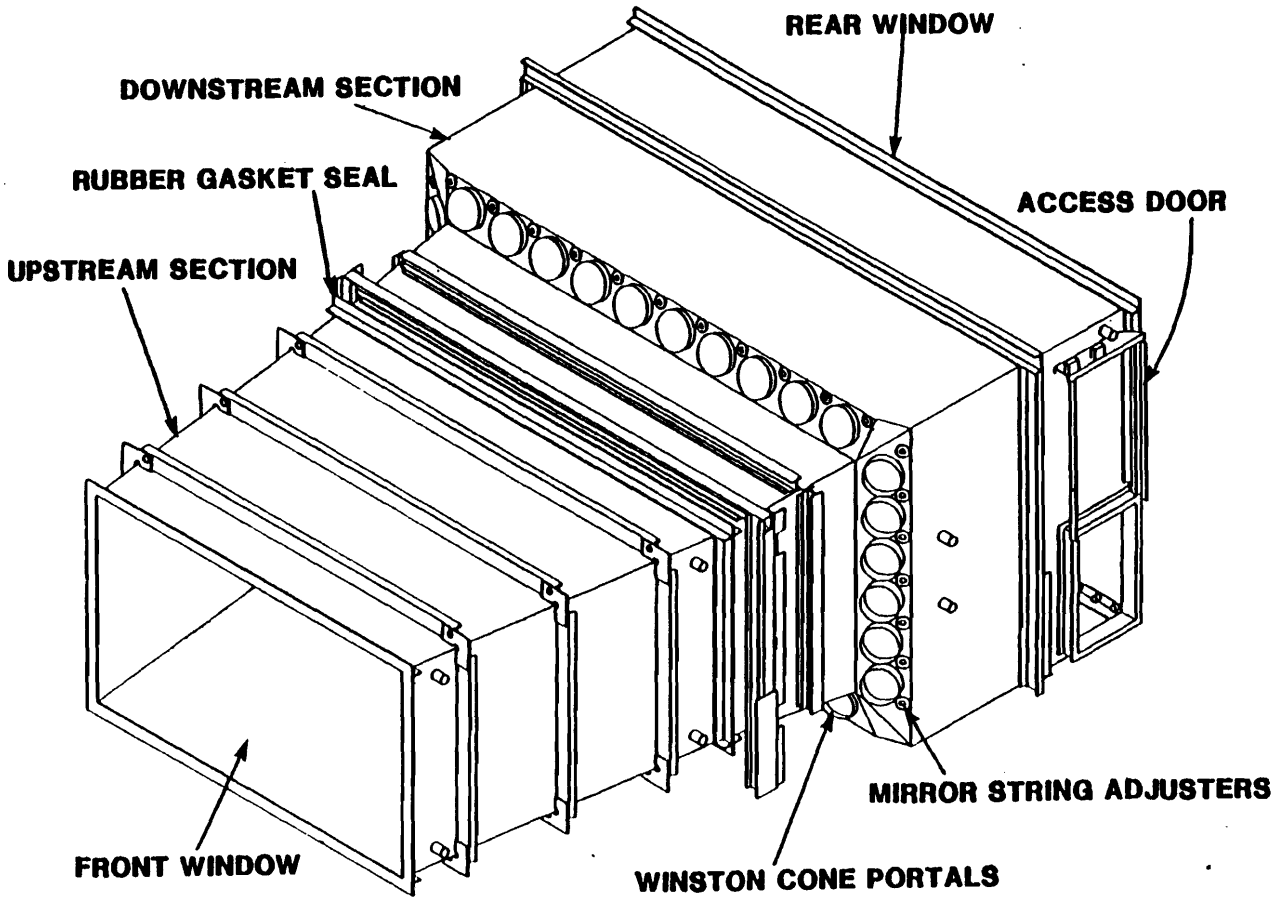

Figure 21

DOWNSTREAM CERENKOV COUNTER (C2)

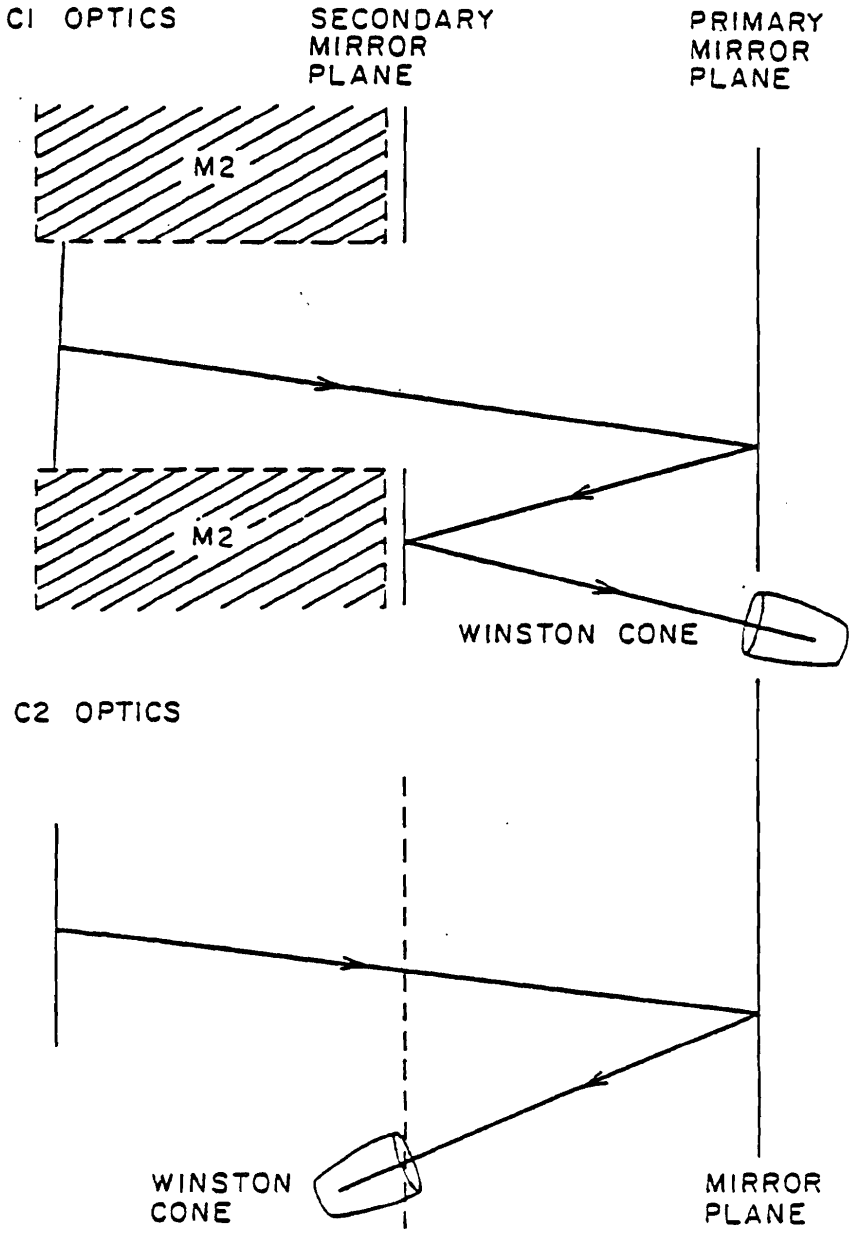
C1 OPTICS
SECONDARY MIRROR PLANE
PRIMARY MIRROR PLANE
M2
M2
WINSTON CONE
C2 OPTICS
WINSTON CONE
MIRROR PLANE

Figure 22

CERENKOV MIRROR SEGMENTATION

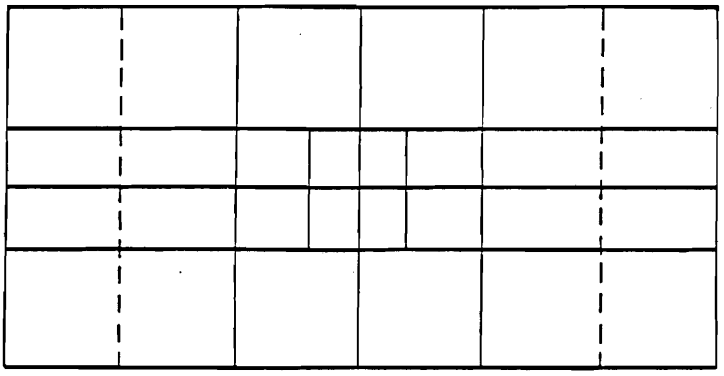

CERENKOV MIRROR SUSPENSION

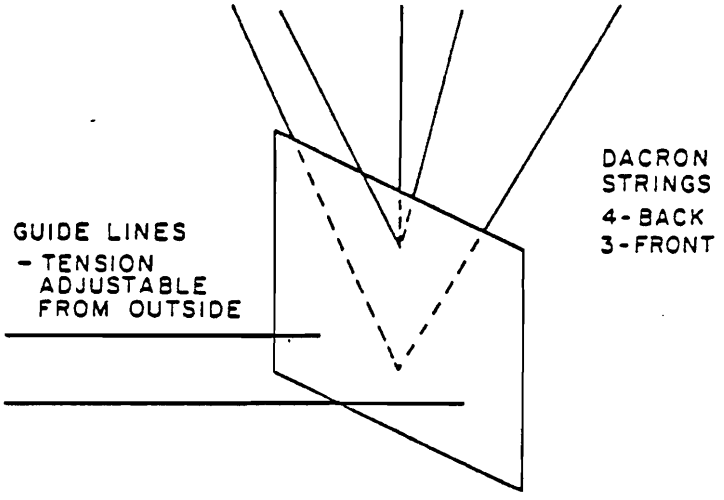

Figure 23

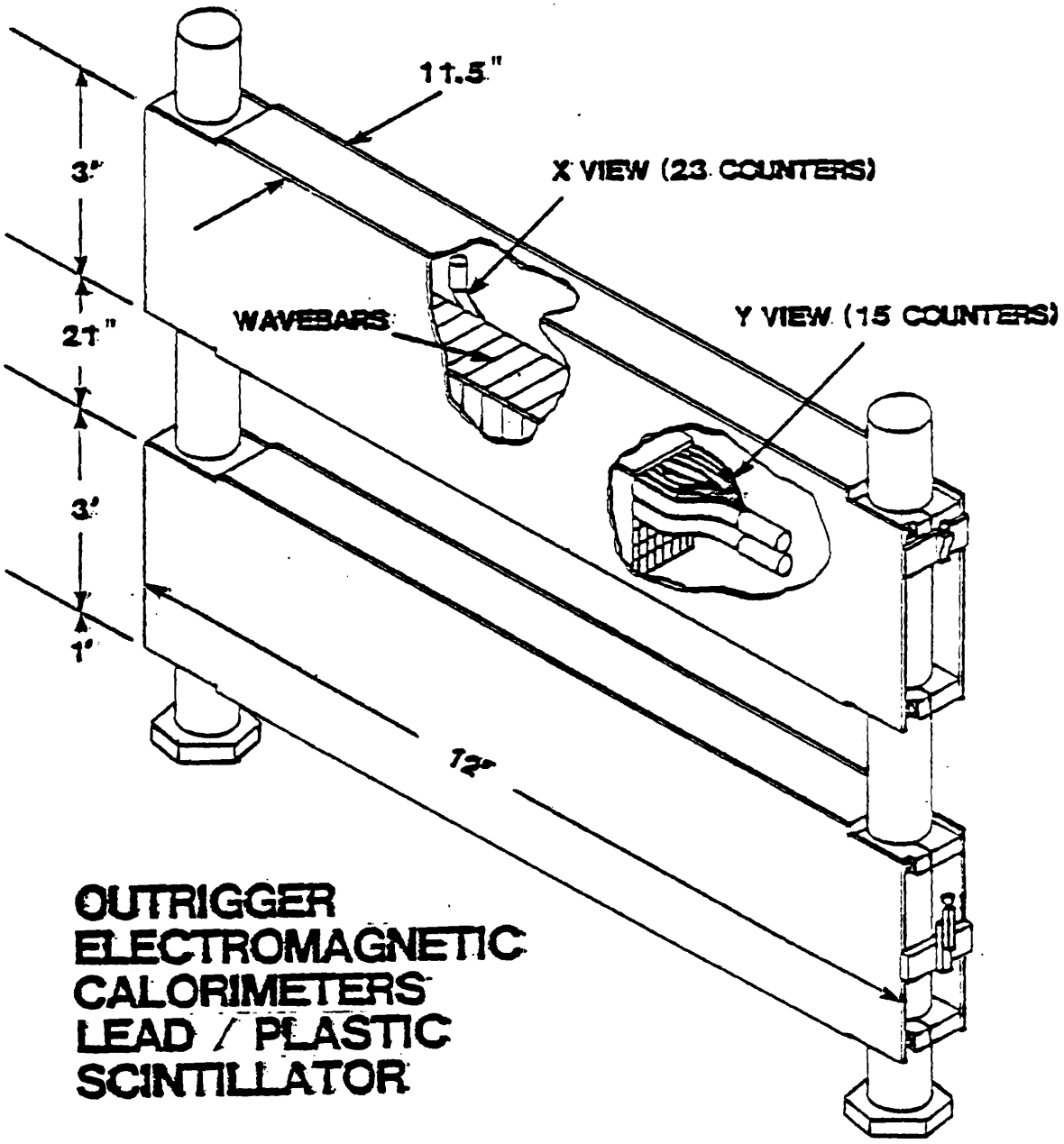
11.5"
3"
X VIEW (23 COUNTERS)
WAVEBARS
Y VIEW (15 COUNTERS)
21"
3'
1'
12'
OUTRIGGER
ELECTROMAGNETIC
CALORIMETERS
LEAD / PLASTIC
SCINTILLATOR

Figure 24

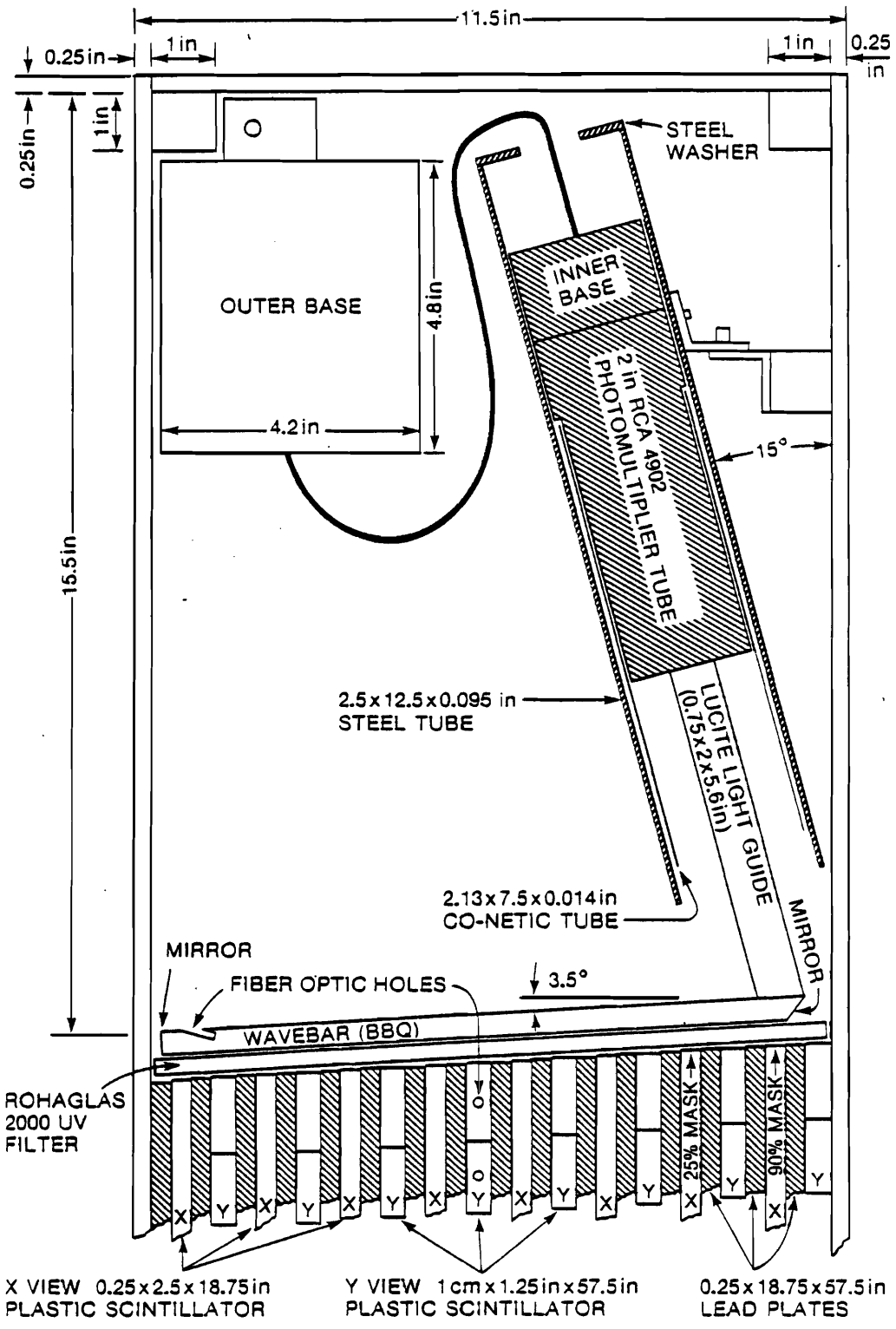

OUTRIGGER ELECTROMAGNETIC CALORIMETER SIDE VIEW

Figure 25

Figure 26

LASER SYSTEM

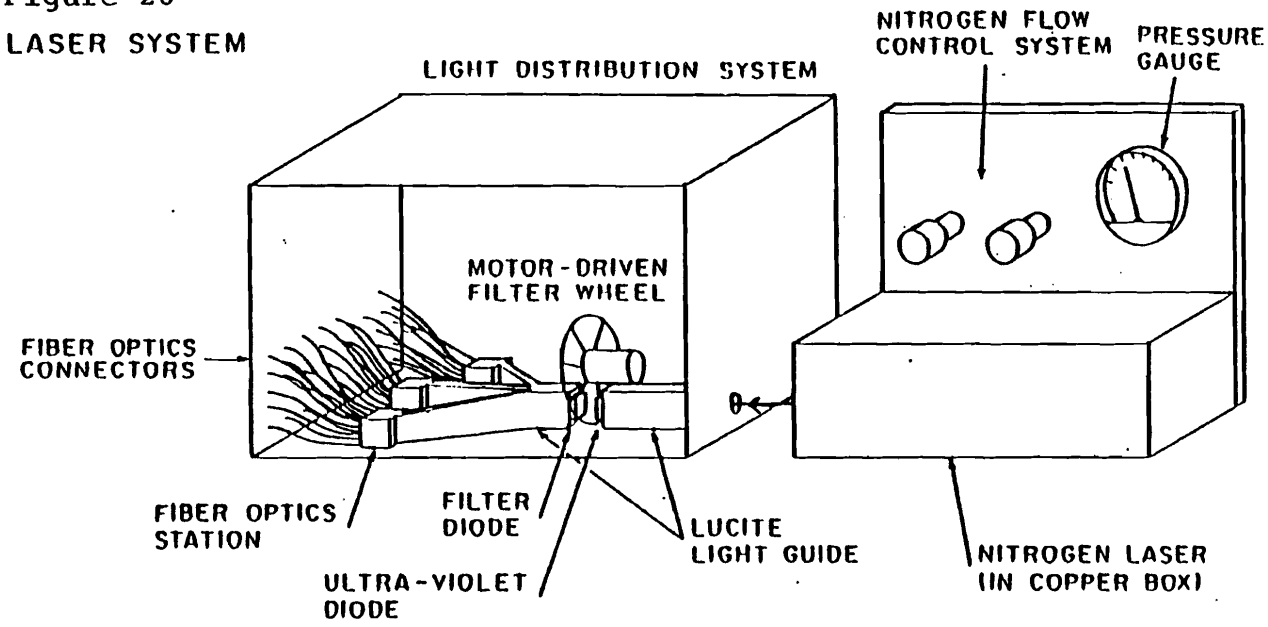

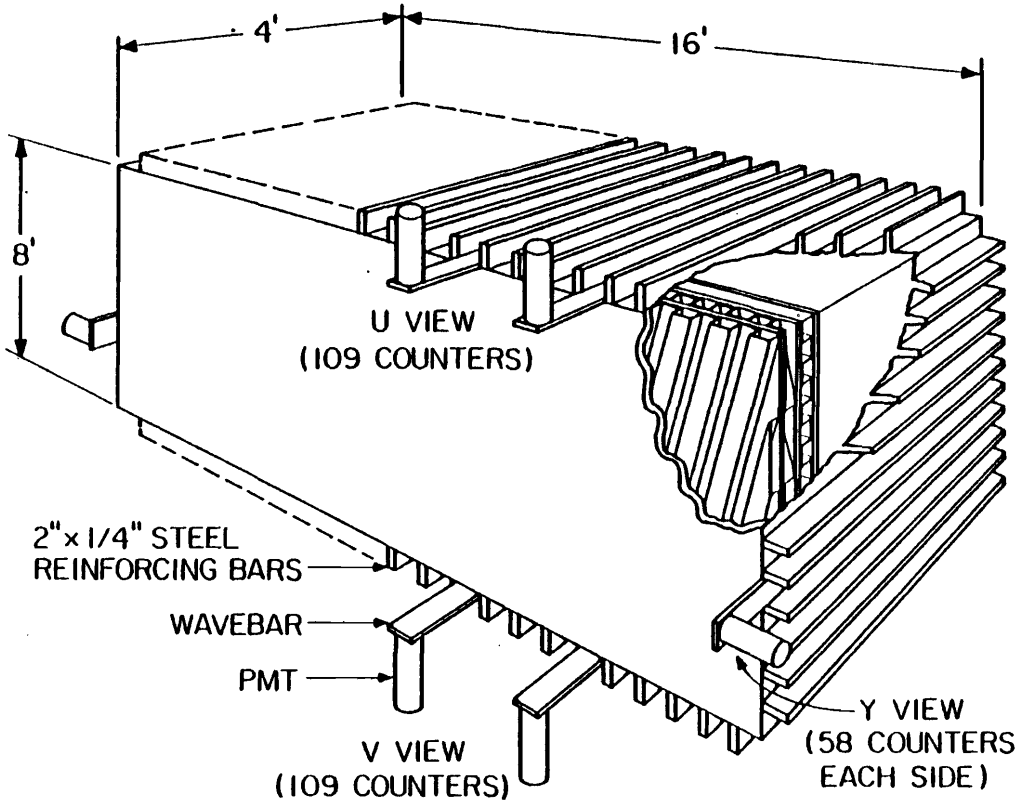

LEAD/LIQUID SCINTILLATOR SHOWER COUNTER (SLIC)
(SCHEMATIC)

Figure 27

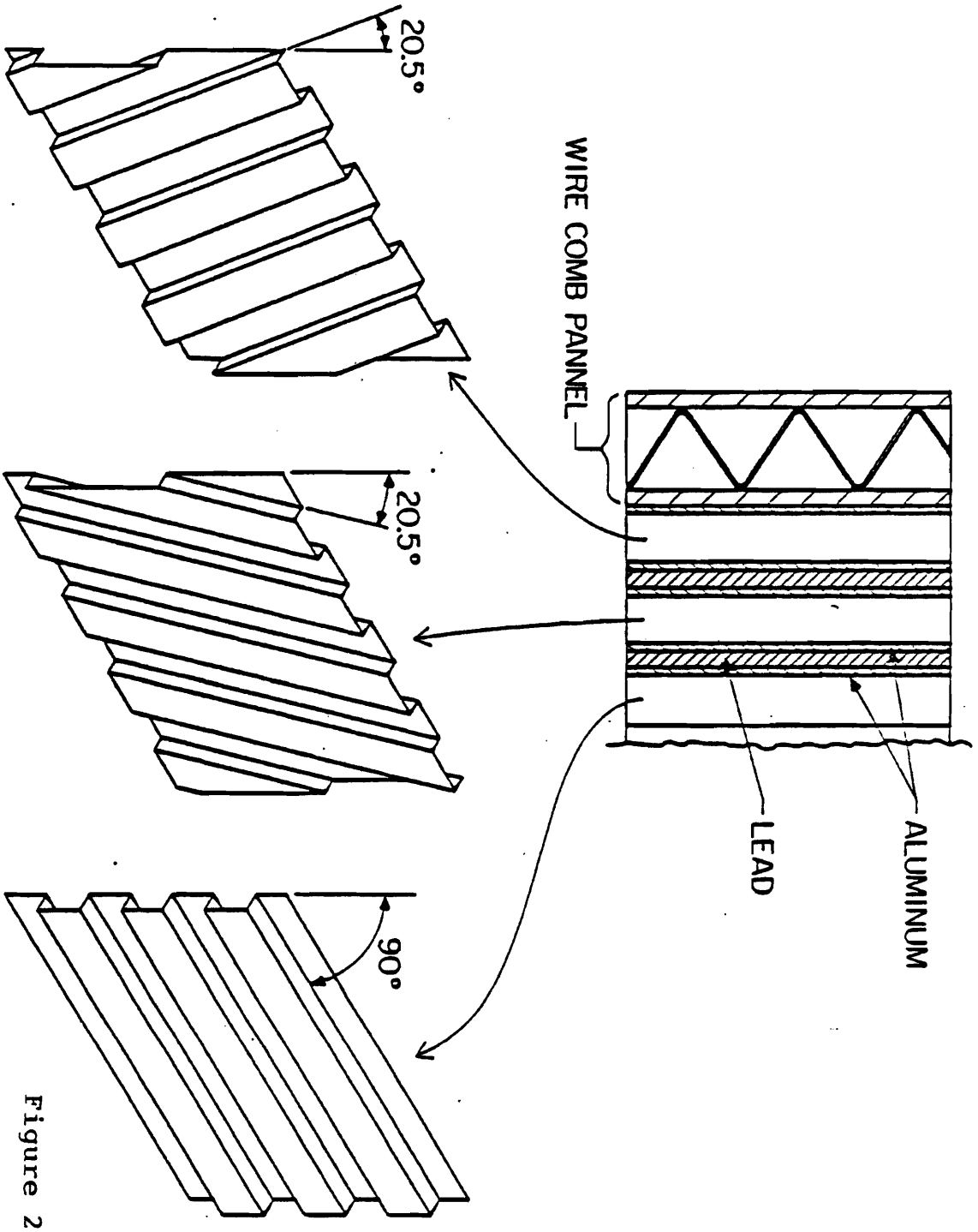

Figure 28

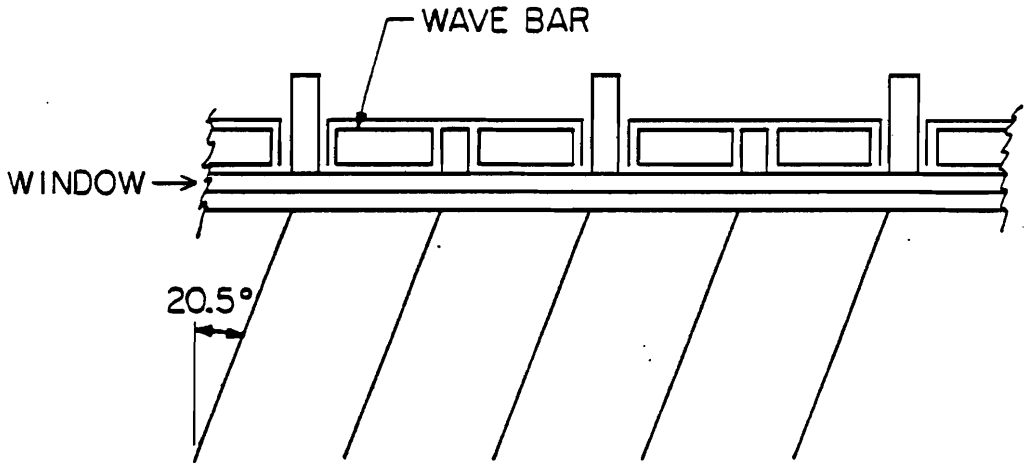

Figure 29

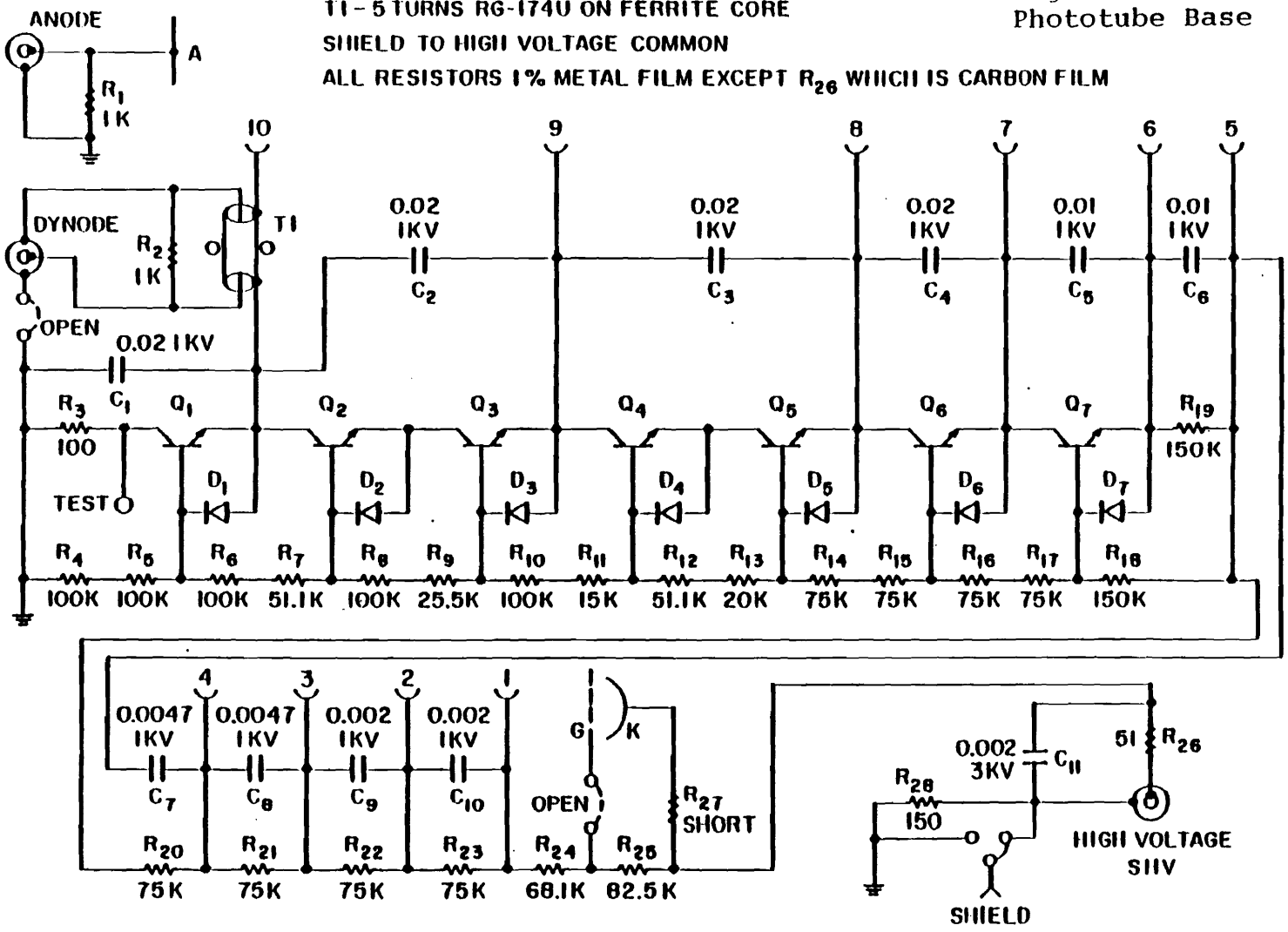

Figure 30
Phototube Base

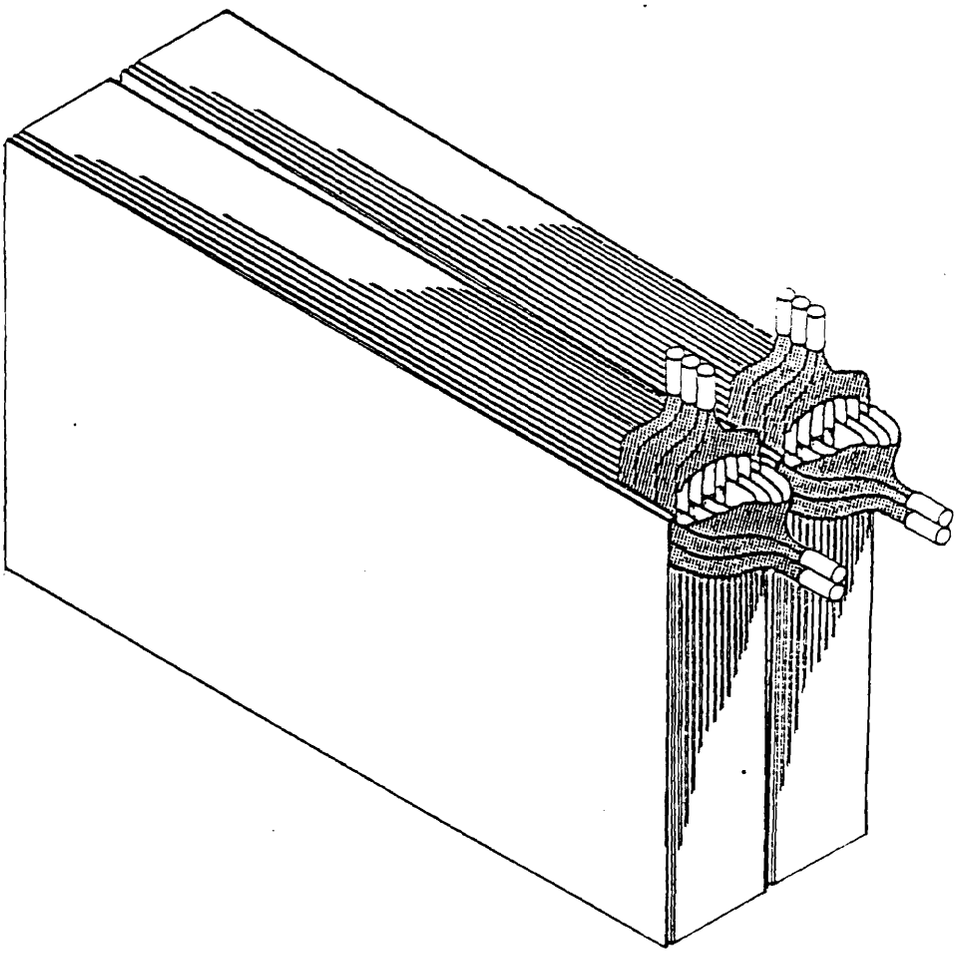

Figure 31. Hadronic Calorimeter

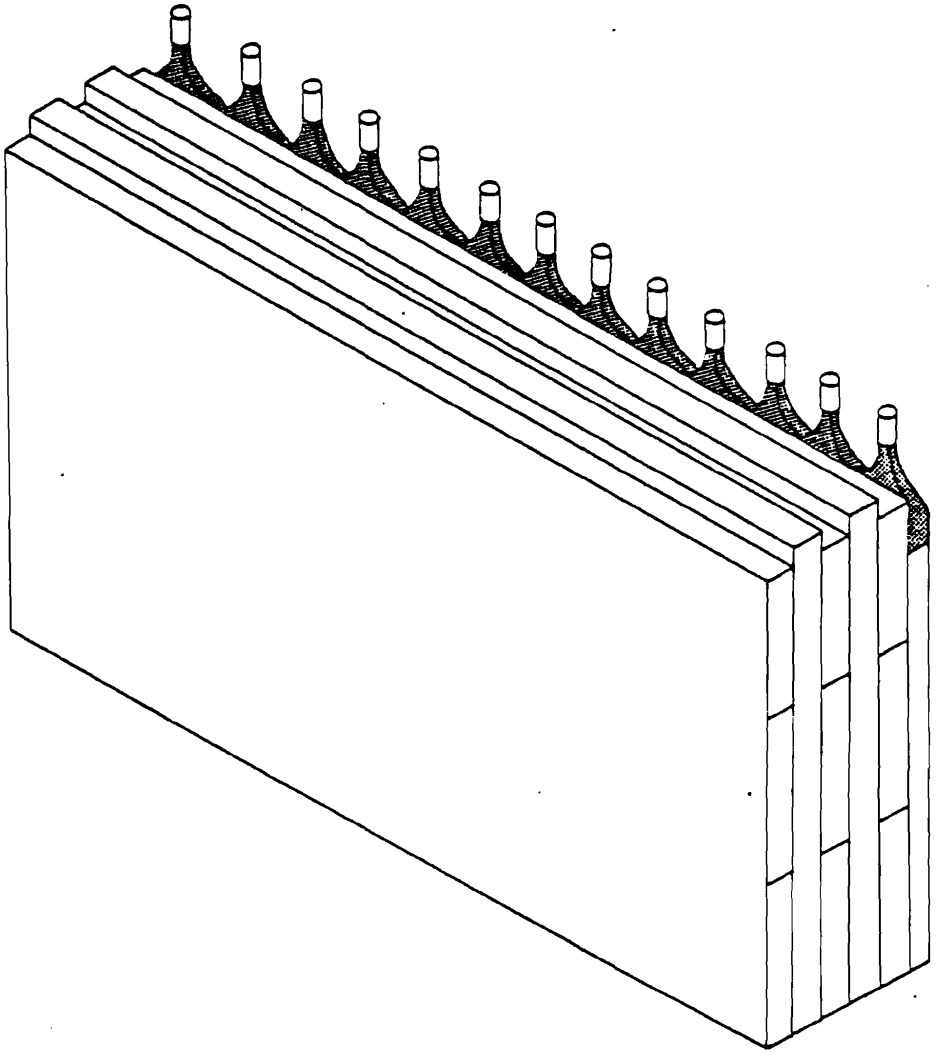

Figure 32. Muon Wall

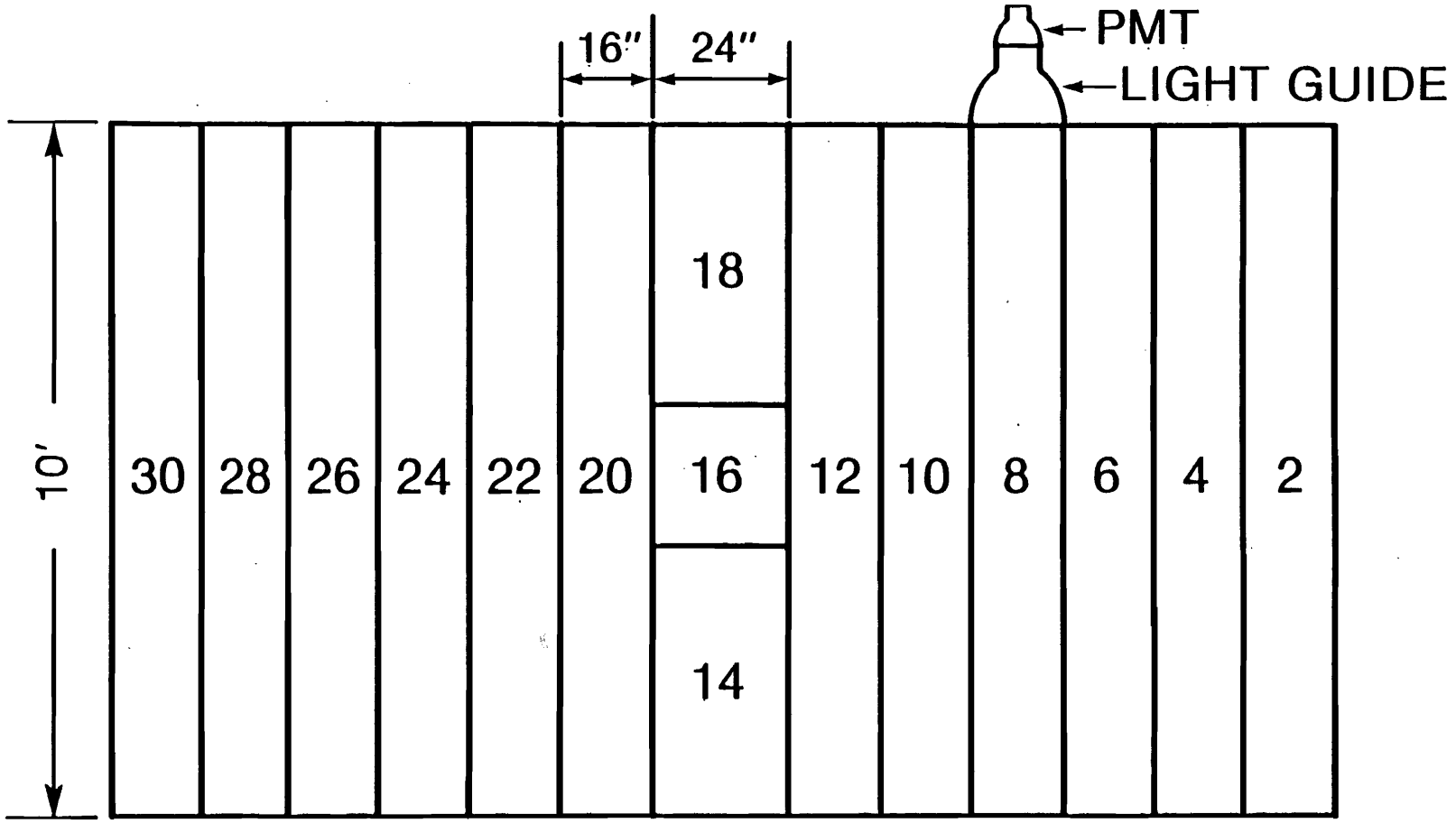

Figure 33

MUON WALL

Figure 34
HADRONIC
TRIGGER

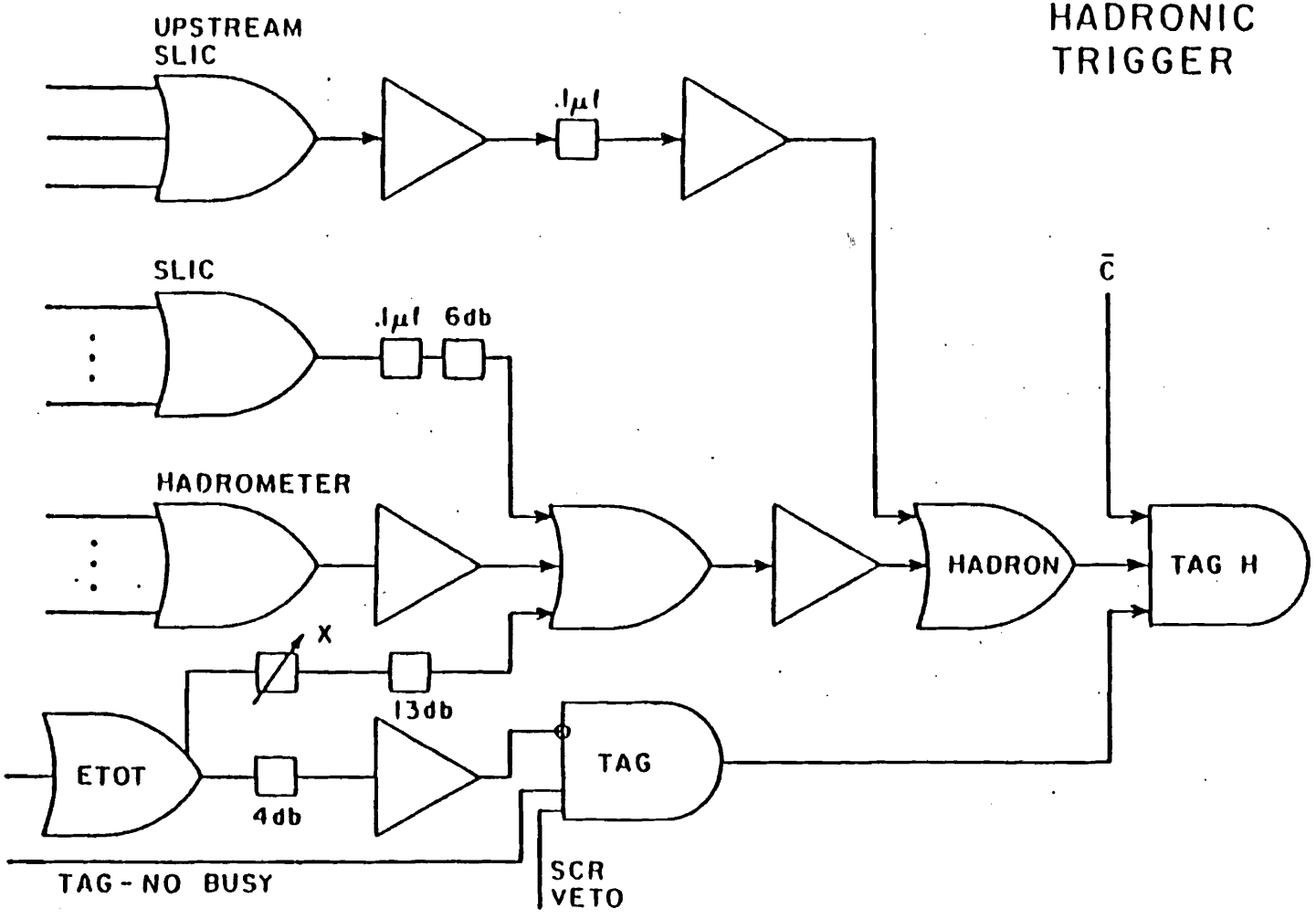

RECOIL PROCESSOR
- BASIC FLOW CHART

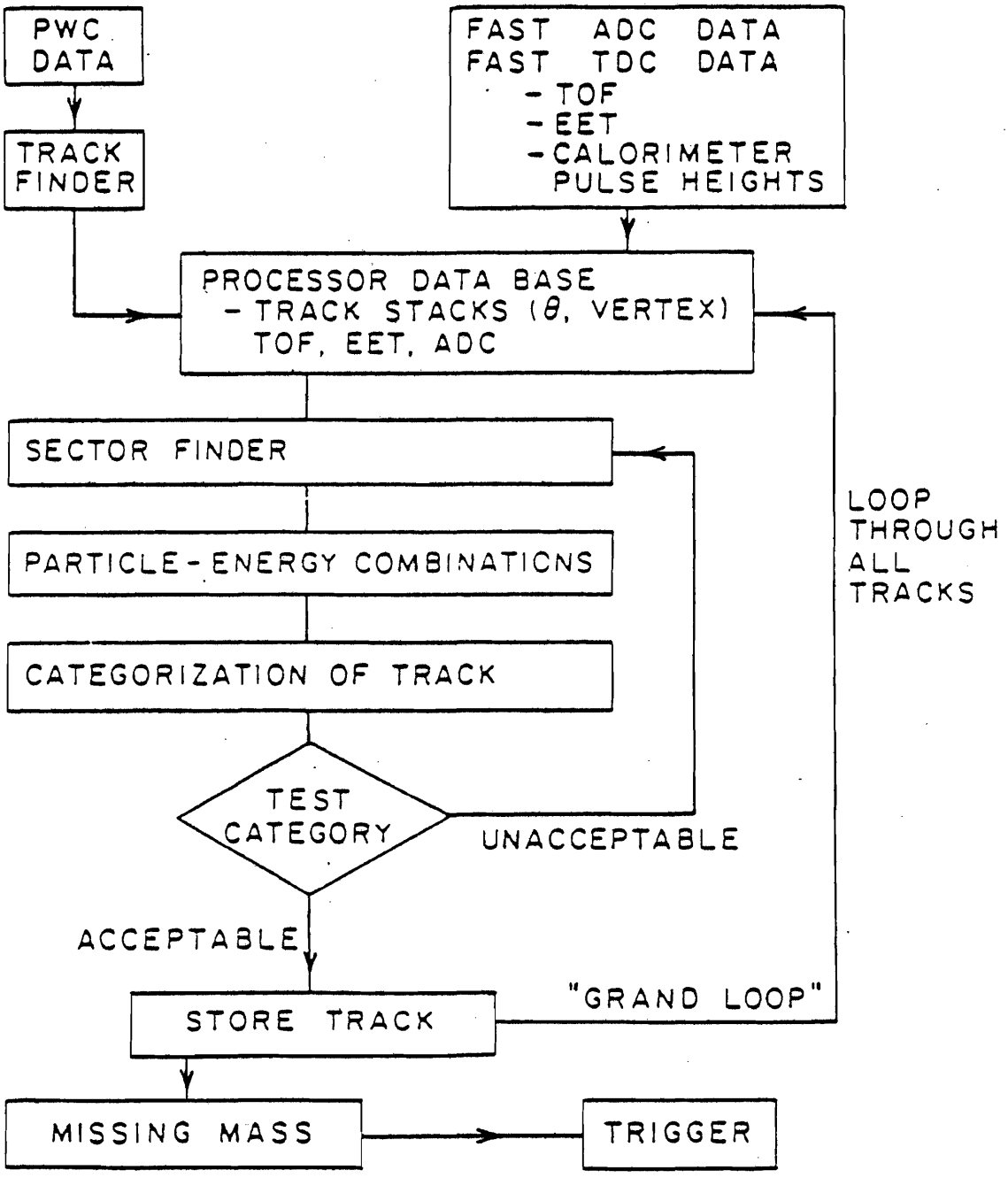

Figure 35

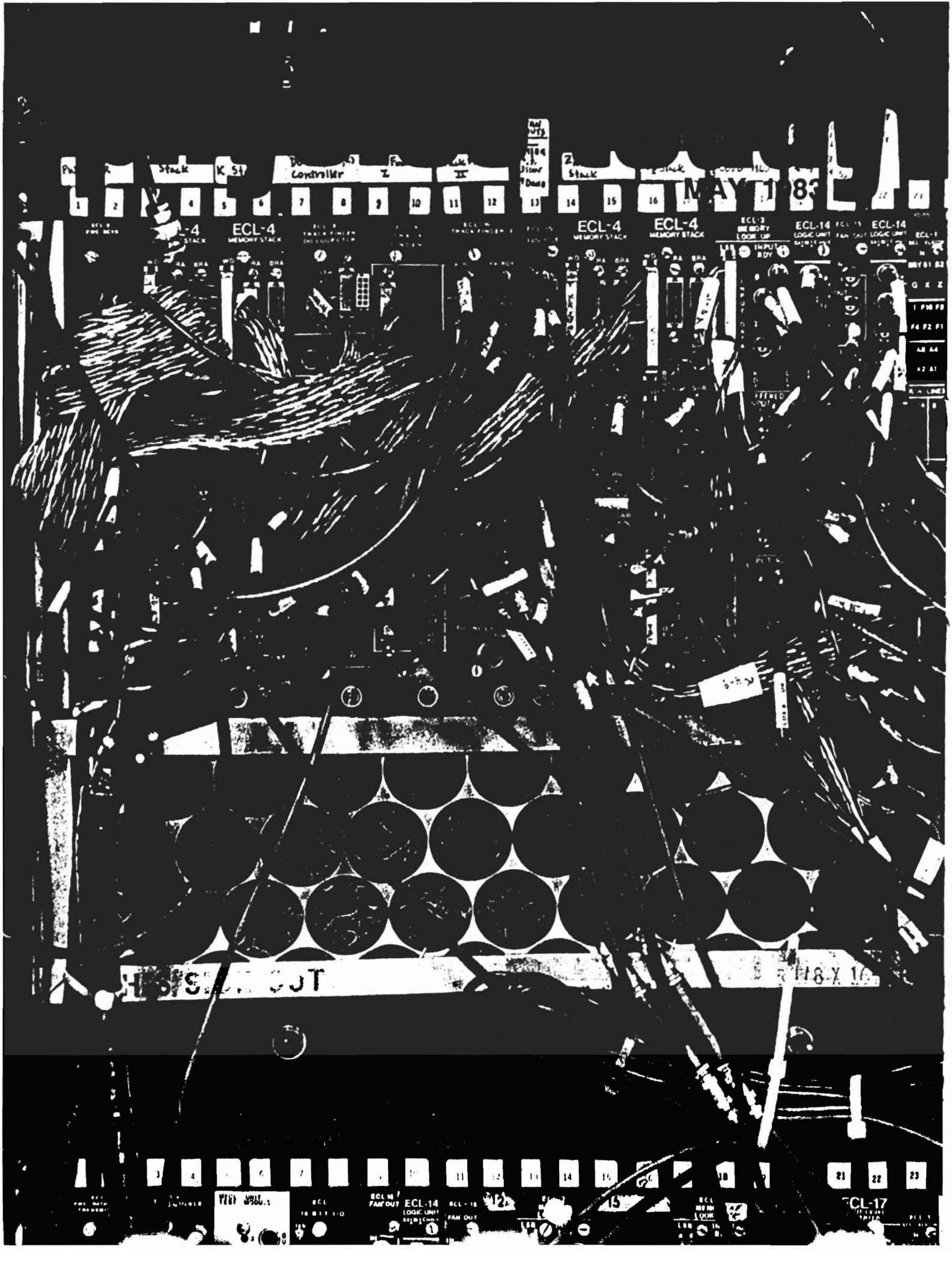
ECL-4
MEMORY STACK
ECL-14
LOGIC UNIT
MAY 18

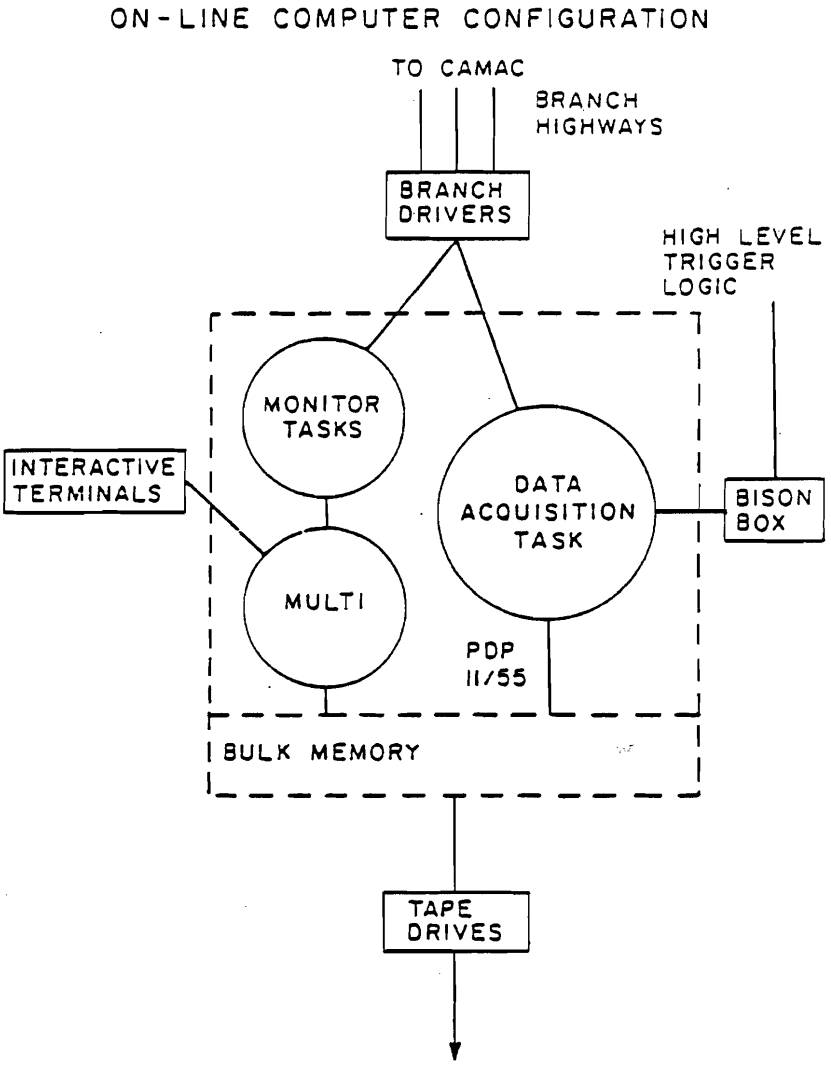
ON-LINE COMPUTER CONFIGURATION
TO CAMAC
BRANCH HIGHWAYS
BRANCH DRIVERS
HIGH LEVEL TRIGGER LOGIC
MONITOR TASKS
INTERACTIVE TERMINALS
DATA ACQUISITION TASK
BISON BOX
MULTI
PDP 11/55
BULK MEMORY
TAPE DRIVES

Figure 37

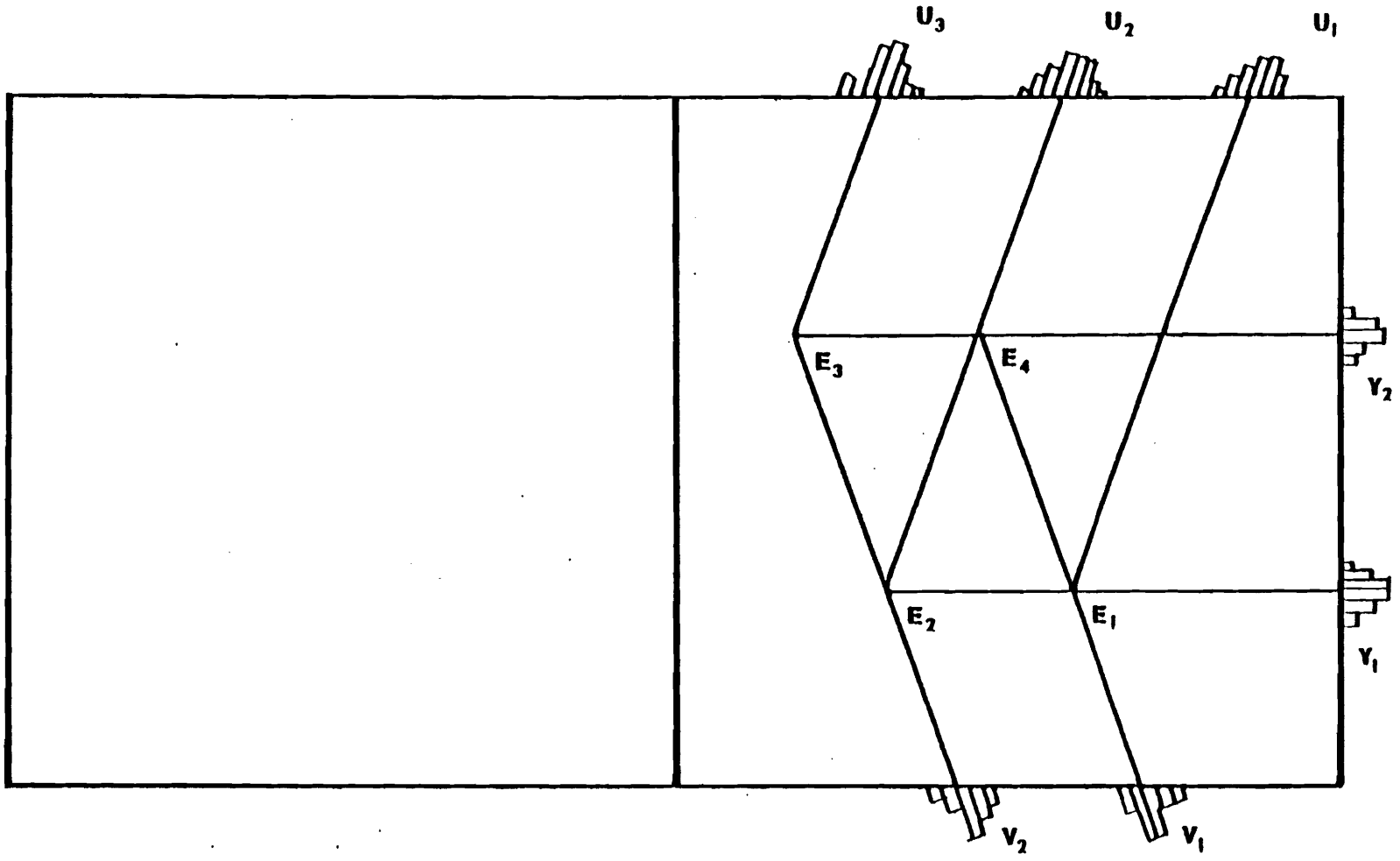

Figure 38

SIMPLE SLIC RECONSTRUCTION AMBIGUITY

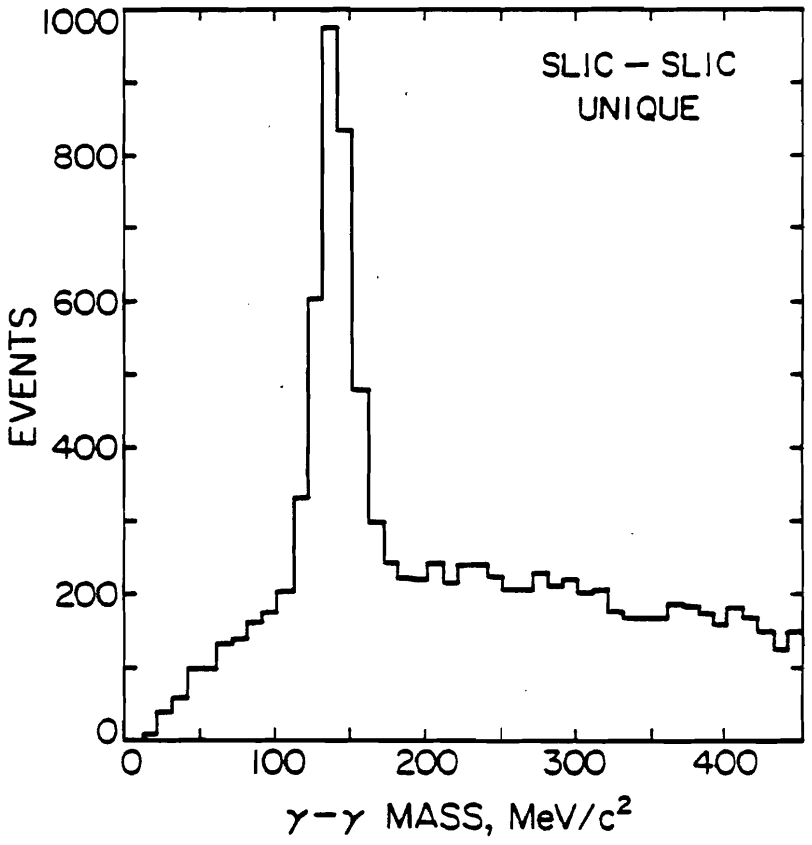
1000
800
600
400
200
0
EVENTS
SLIC – SLIC
UNIQUE
0
100
200
300
400
γ–γ MASS, MeV/c²

Figure 39

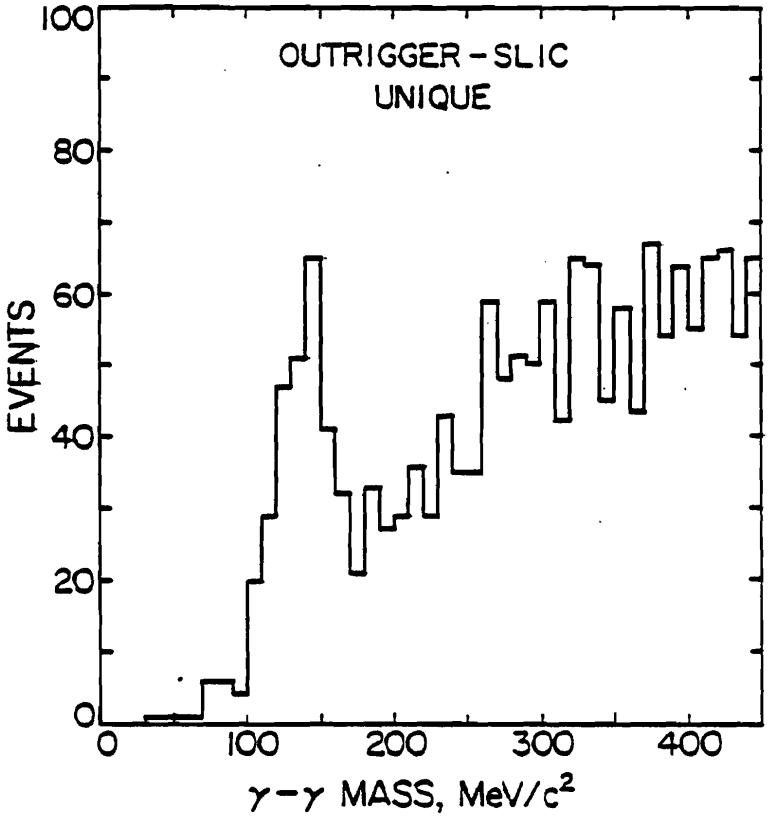
OUTRIGGER - SLIC
UNIQUE
EVENTS
100
80
60
40
20
0
0
100
200
300
400
γ−γ MASS, MeV/c²

Figure 40

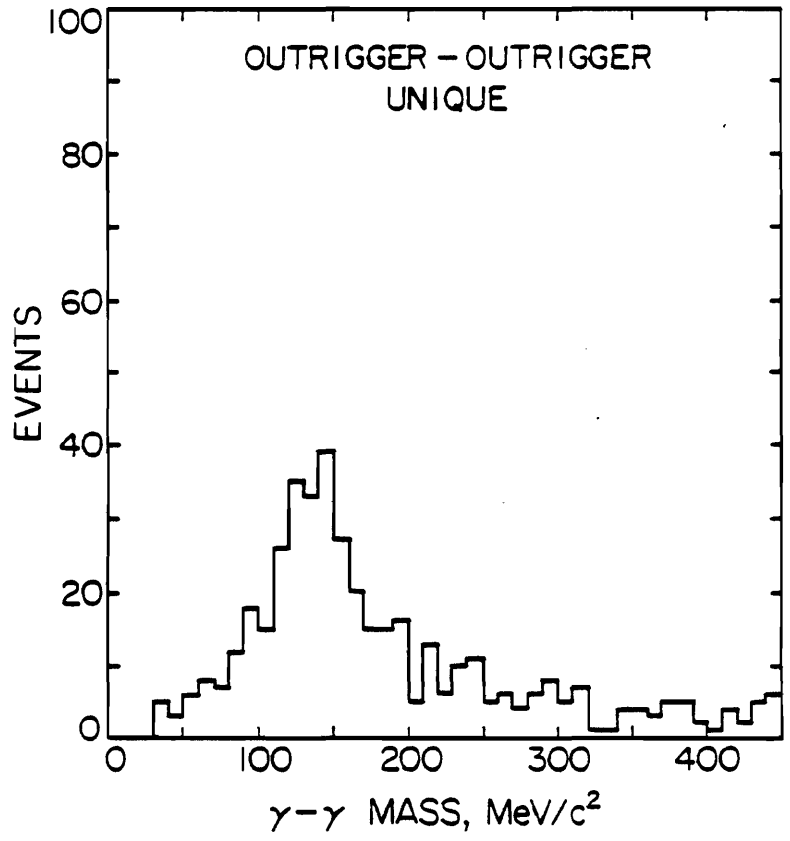
OUTRIGGER – OUTRIGGER
UNIQUE
EVENTS
100
80
60
40
20
0
0
100
200
300
400
γ–γ MASS, MeV/c²

Figure 41

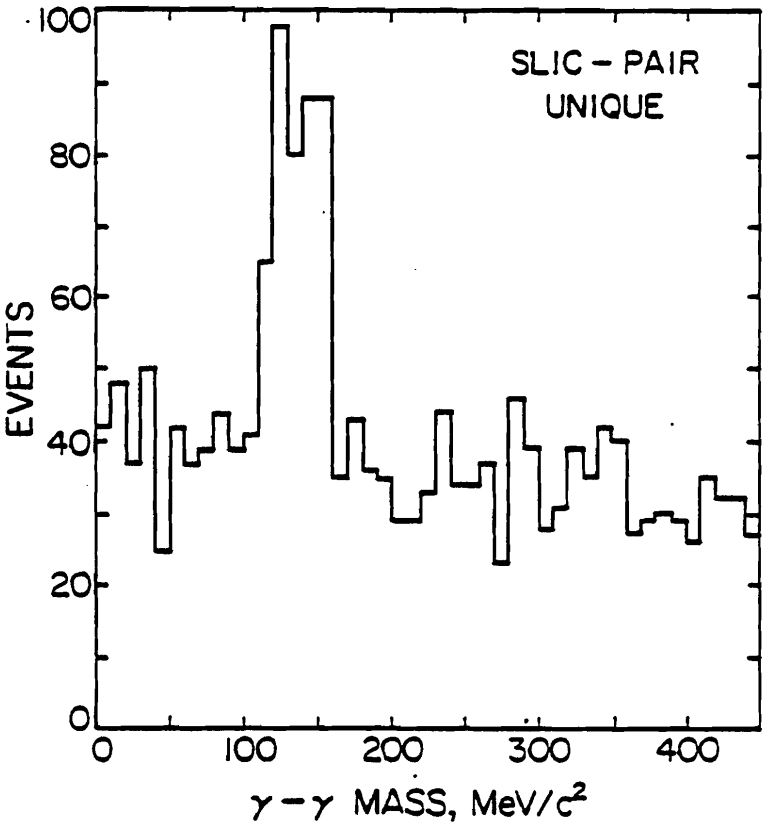
SLIC – PAIR
UNIQUE
EVENTS
0
20
40
60
80
100
0
100
200
300
400
γ – γ MASS, MeV/c²

Figure 42

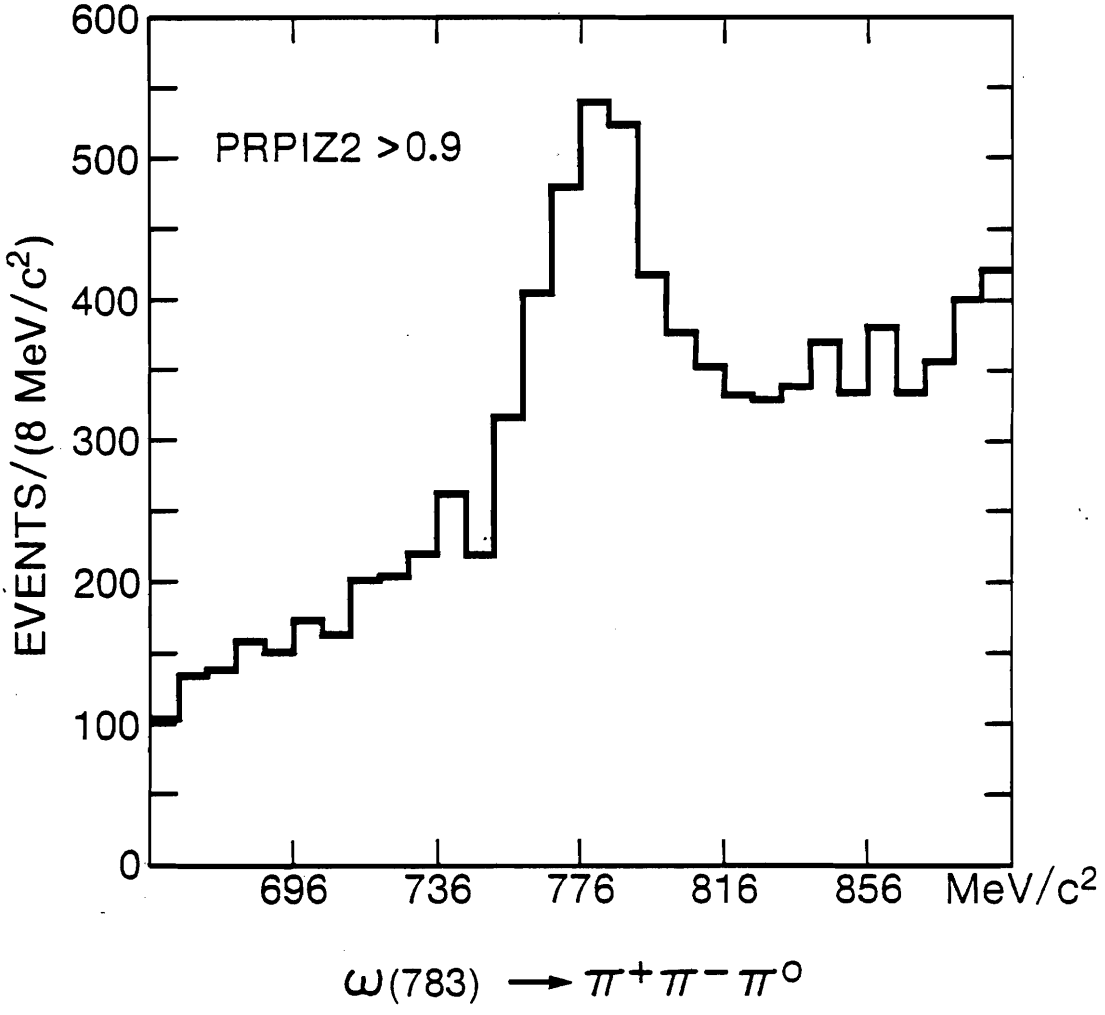
600
500
400
300
200
100
0
PRPIZ2 >0.9
EVENTS/(8 MeV/c²)
696
736
776
816
856
MeV/c²
ω(783) → π⁺π⁻π°

Figure 43

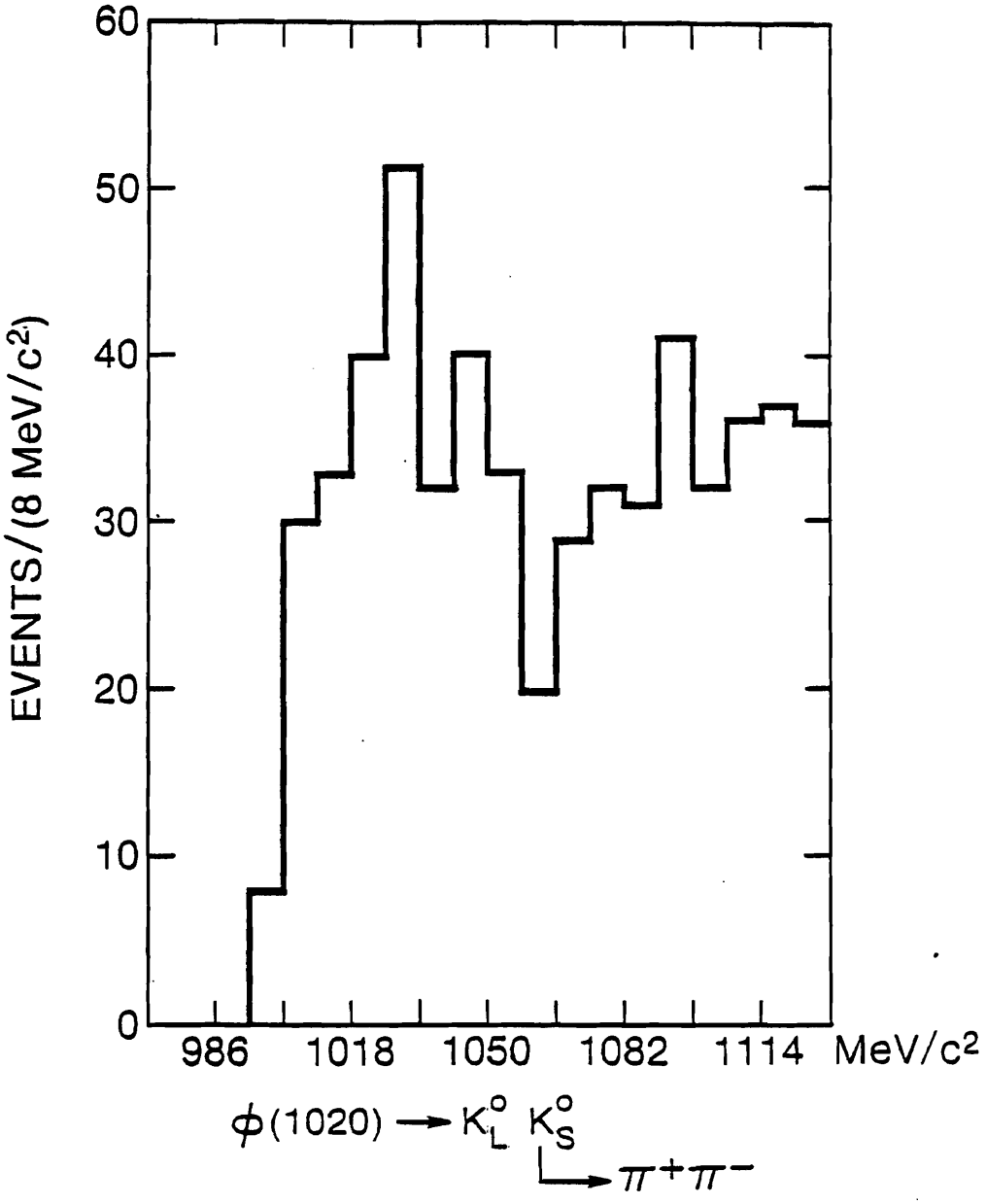
60
50
40
30
20
10
0
EVENTS/(8 MeV/c²)
986
1018
1050
1082
1114
MeV/c²
φ(1020) → K°L K°S
→ π⁺π⁻

Figure 44

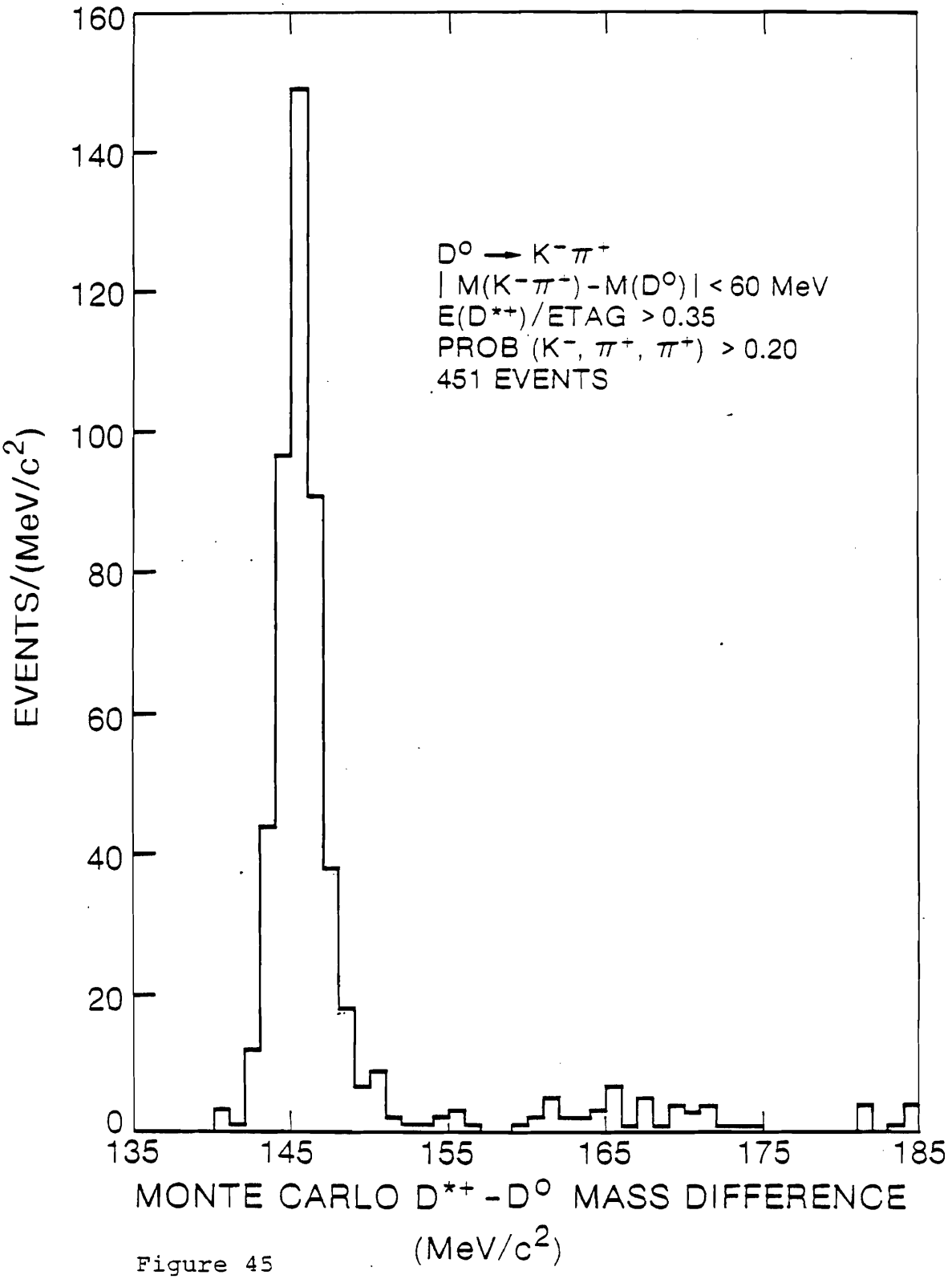
160
140
120
100
80
60
40
20
0
135
145
155
165
175
185
EVENTS/(MeV/c²)
D⁰ → K⁻π⁺
| M(K⁻π⁺) - M(D⁰) | < 60 MeV
E(D*⁺)/ETAG > 0.35
PROB (K⁻, π⁺, π⁺) > 0.20
451 EVENTS
MONTE CARLO D*⁺ - D⁰ MASS DIFFERENCE
(MeV/c²)

Figure 45

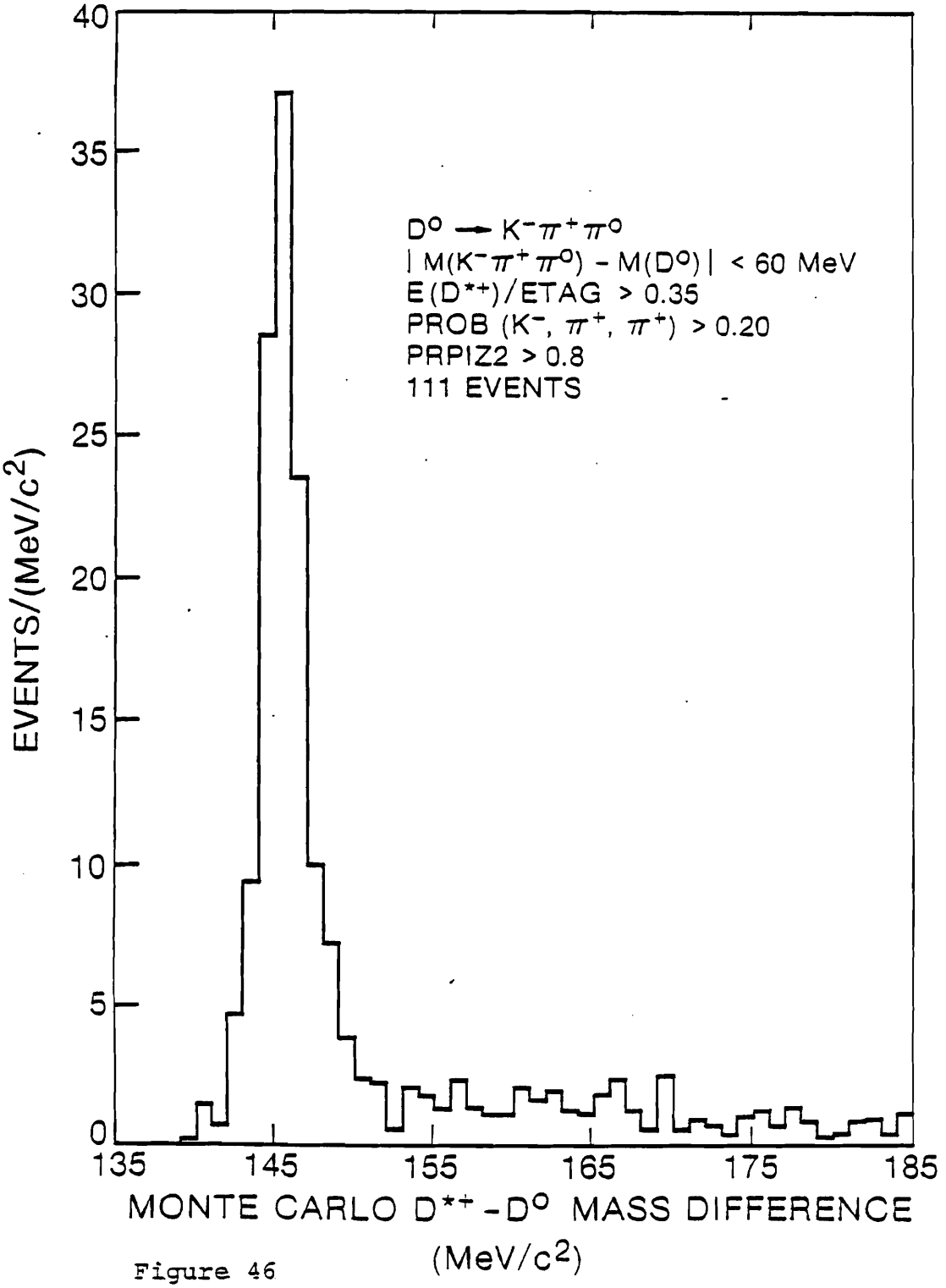
$D^0 \rightarrow K^-\pi^+\pi^0$
$|M(K^-\pi^+\pi^0) - M(D^0)| < 60$ MeV
$E(D^{*+})/ETAG > 0.35$
PROB $(K^-, \pi^+, \pi^+) > 0.20$
PRPIZ2 > 0.8
111 EVENTS
EVENTS/(MeV/c^2)
0
5
10
15
20
25
30
35
40
135
145
155
165
175
185
MONTE CARLO $D^{*+} - D^0$ MASS DIFFERENCE
(MeV/c^2)

Figure 46

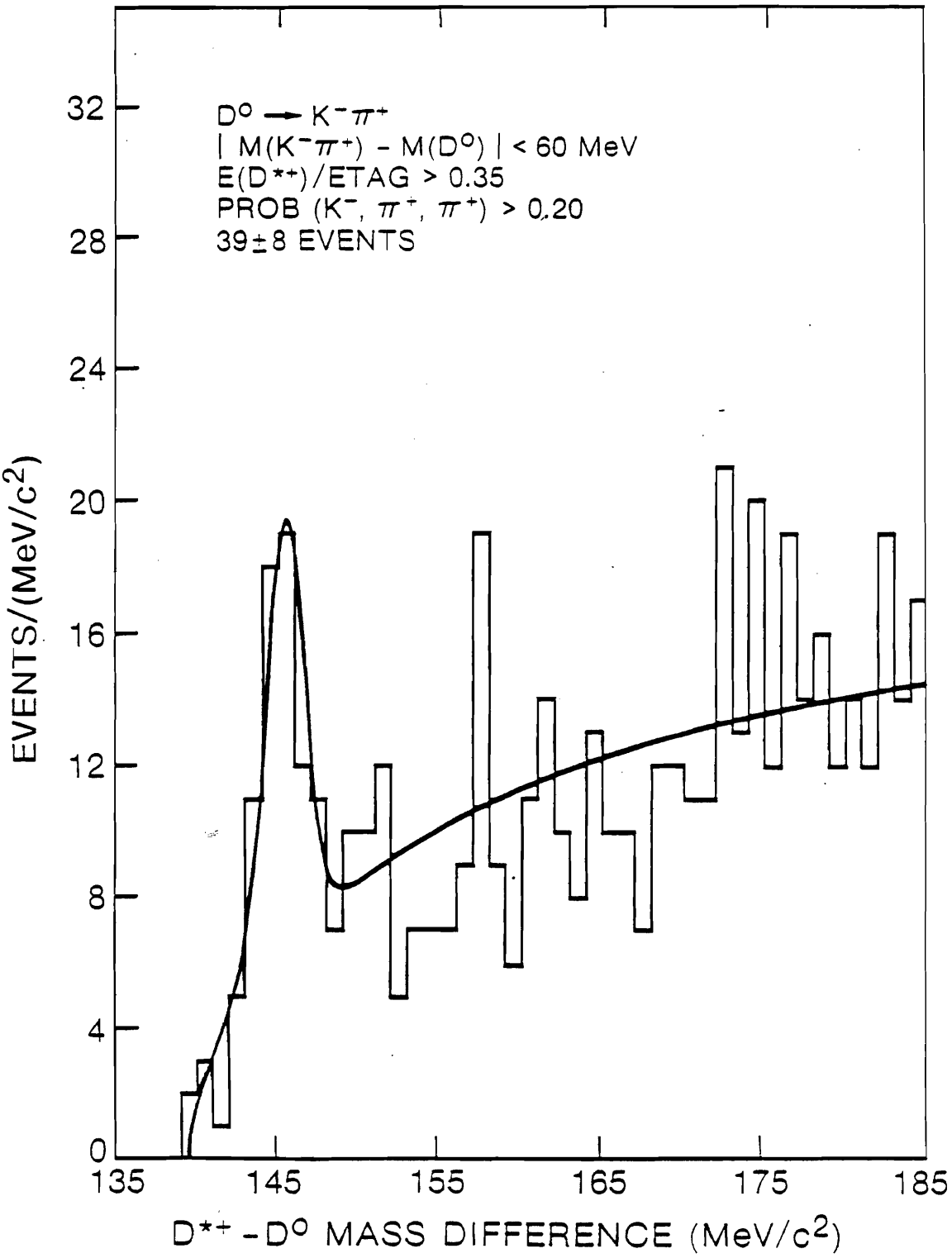
$D^0 \rightarrow K^-\pi^+$
$|\ M(K^-\pi^+) - M(D^0)\ | < 60$ MeV
$E(D^{*+})/ETAG > 0.35$
PROB $(K^-, \pi^+, \pi^+) > 0.20$
39 ± 8 EVENTS
EVENTS/(MeV/c^2)
0
4
8
12
16
20
24
28
32
135
145
155
165
175
185
$D^{*+} - D^0$ MASS DIFFERENCE (MeV/c^2)

Figure 47

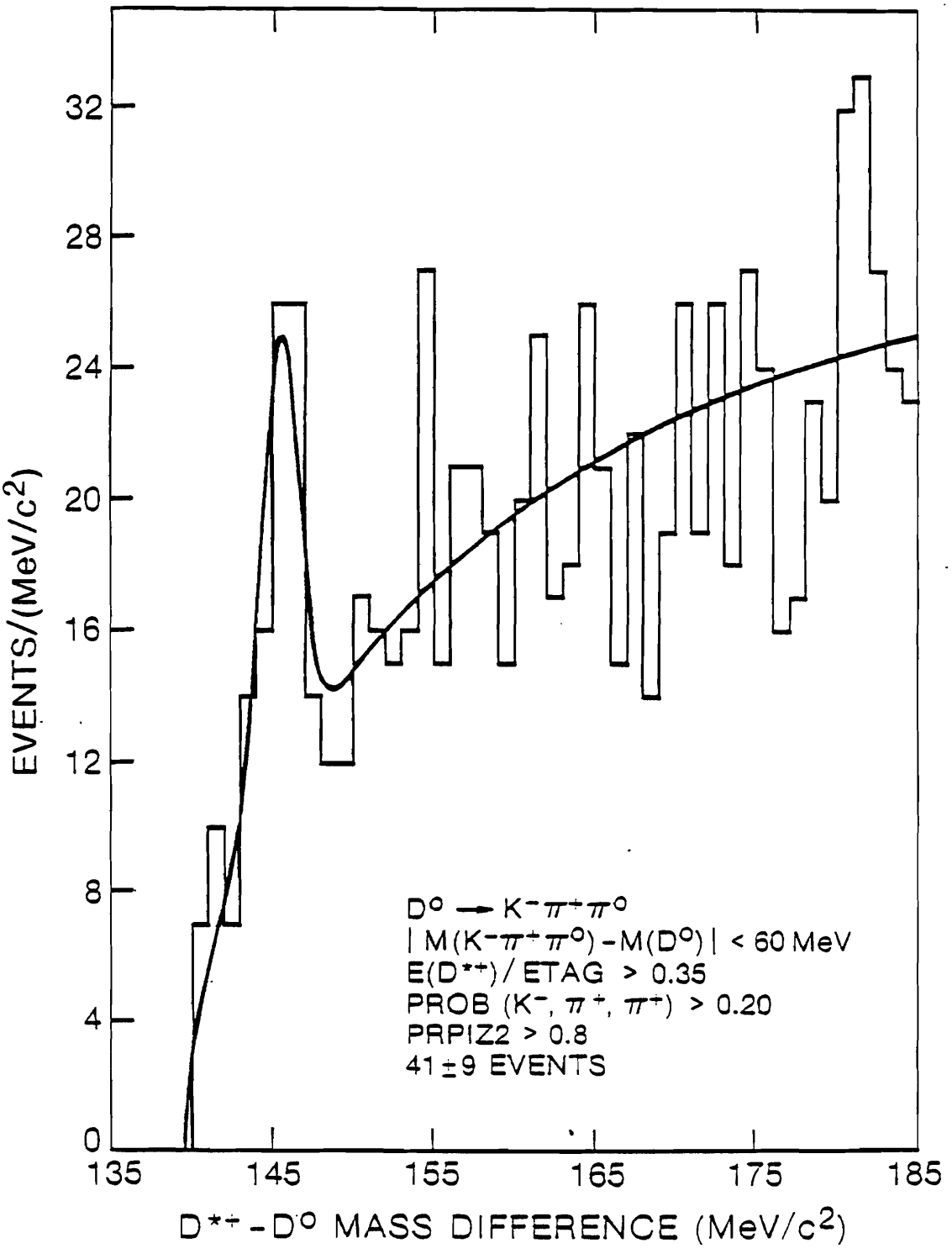
EVENTS/(MeV/c²)
D*⁺ - D⁰ MASS DIFFERENCE (MeV/c²)
D⁰ → K⁻π⁺π⁰
| M(K⁻π⁺π⁰) - M(D⁰) | < 60 MeV
E(D*⁺) / ETAG > 0.35
PROB (K⁻, π⁺, π⁺) > 0.20
PRPIZ2 > 0.8
41 ± 9 EVENTS

Figure 48

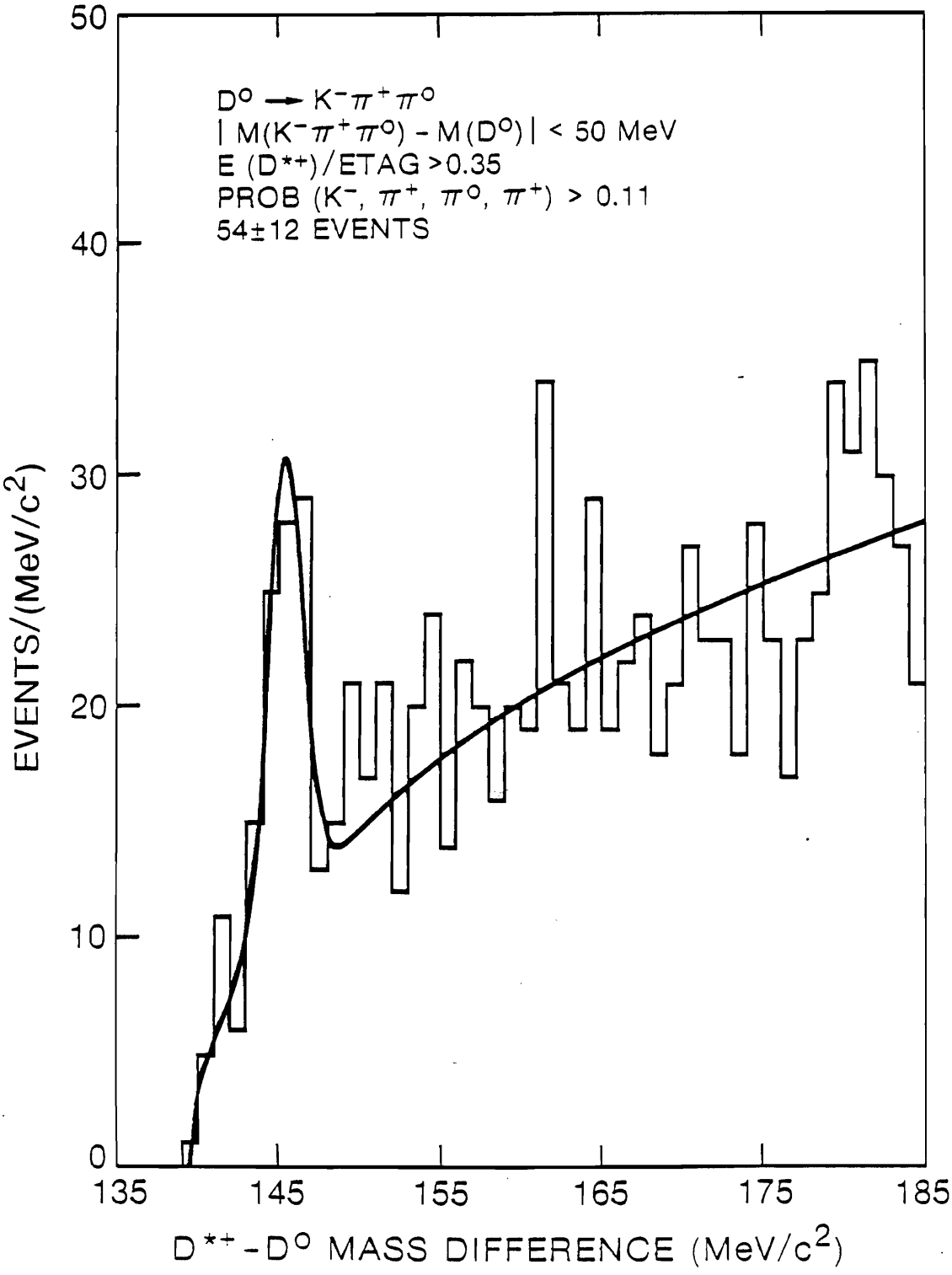
$D^0 \rightarrow K^-\pi^+\pi^0$
$|M(K^-\pi^+\pi^0) - M(D^0)| < 50$ MeV
$E(D^{*+})/ETAG > 0.35$
PROB $(K^-, \pi^+, \pi^0, \pi^+) > 0.11$
54±12 EVENTS
EVENTS/(MeV/c^2)
0
10
20
30
40
50
135
145
155
165
175
185
$D^{*+}-D^0$ MASS DIFFERENCE (MeV/c^2)

Figure 49

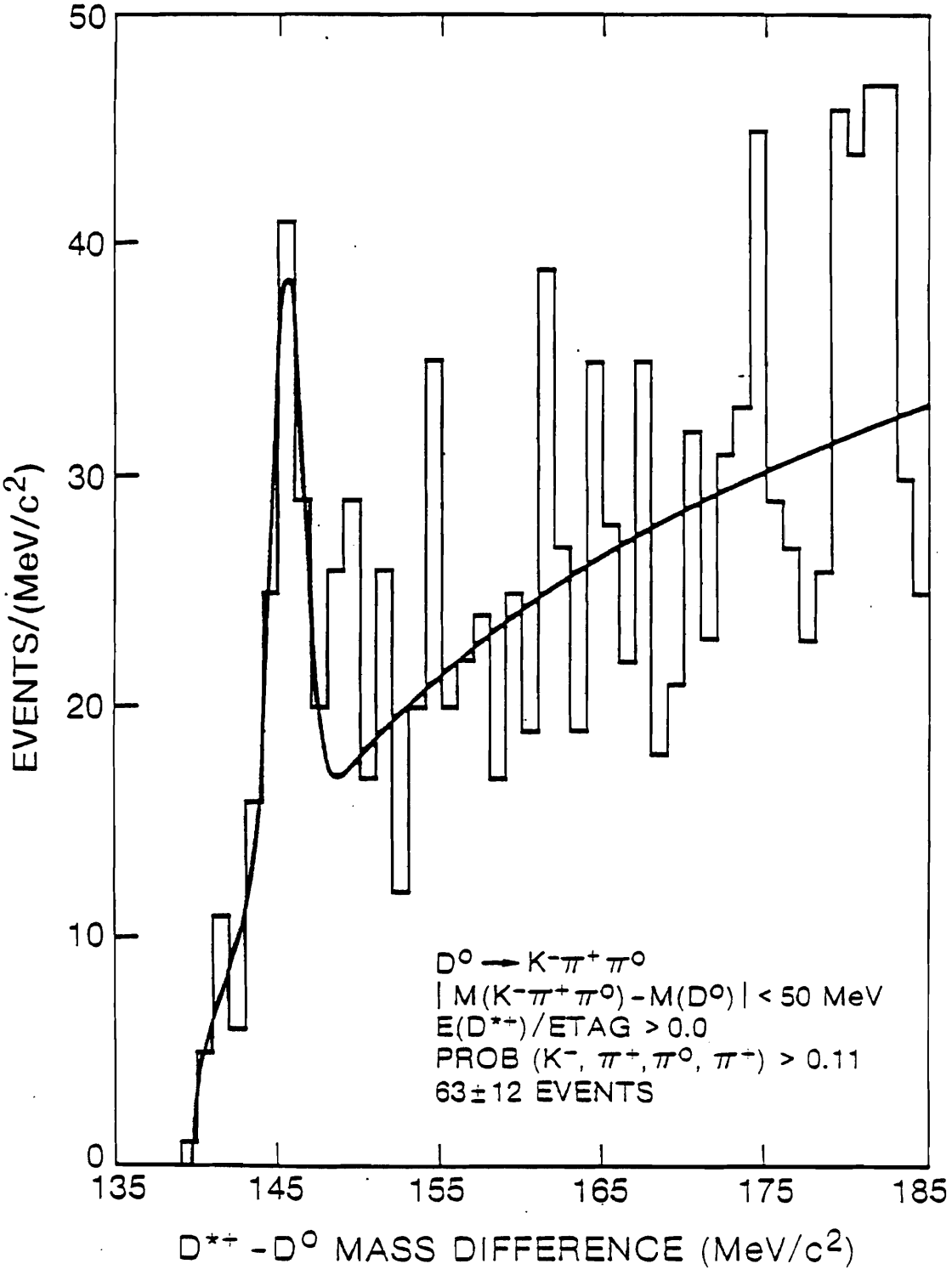
50
40
30
20
10
0
EVENTS/(MeV/c²)
135
145
155
165
175
185
D*± - D⁰ MASS DIFFERENCE (MeV/c²)
D⁰ → K⁻π⁺π⁰
| M(K⁻π⁺π⁰) - M(D⁰) | < 50 MeV
E(D*±)/ETAG > 0.0
PROB (K⁻, π⁺, π⁰, π⁺) > 0.11
63±12 EVENTS

Figure 50

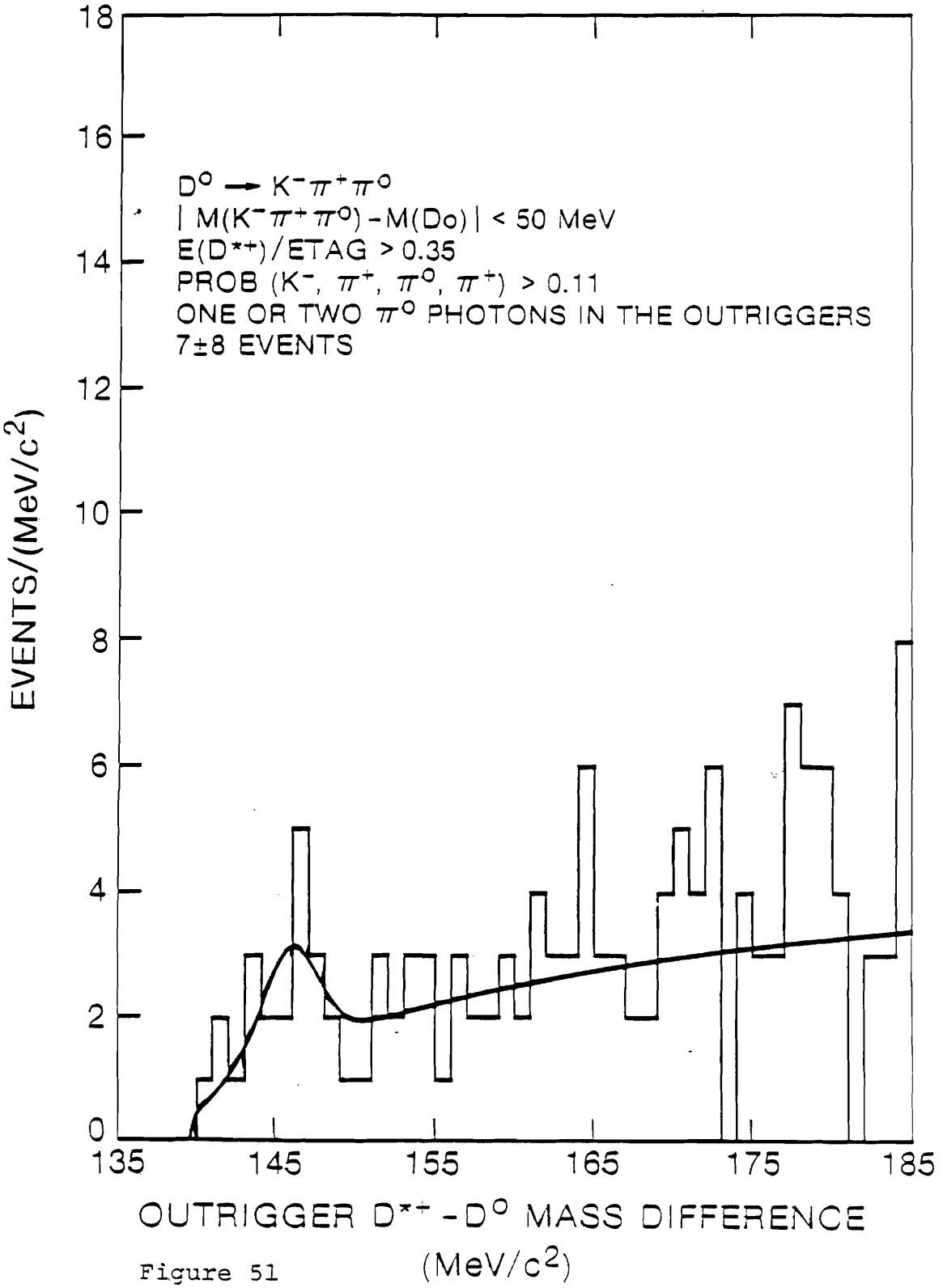
$D^0 \rightarrow K^-\pi^+\pi^0$
$|M(K^-\pi^+\pi^0) - M(Do)| < 50$ MeV
$E(D^{*+})/ETAG > 0.35$
PROB $(K^-, \pi^+, \pi^0, \pi^+) > 0.11$
ONE OR TWO π^0 PHOTONS IN THE OUTRIGGERS
7±8 EVENTS
EVENTS/(MeV/c^2)
0
2
4
6
8
10
12
14
16
18
135
145
155
165
175
185
OUTRIGGER $D^{*+} - D^0$ MASS DIFFERENCE
(MeV/c^2)

Figure 51

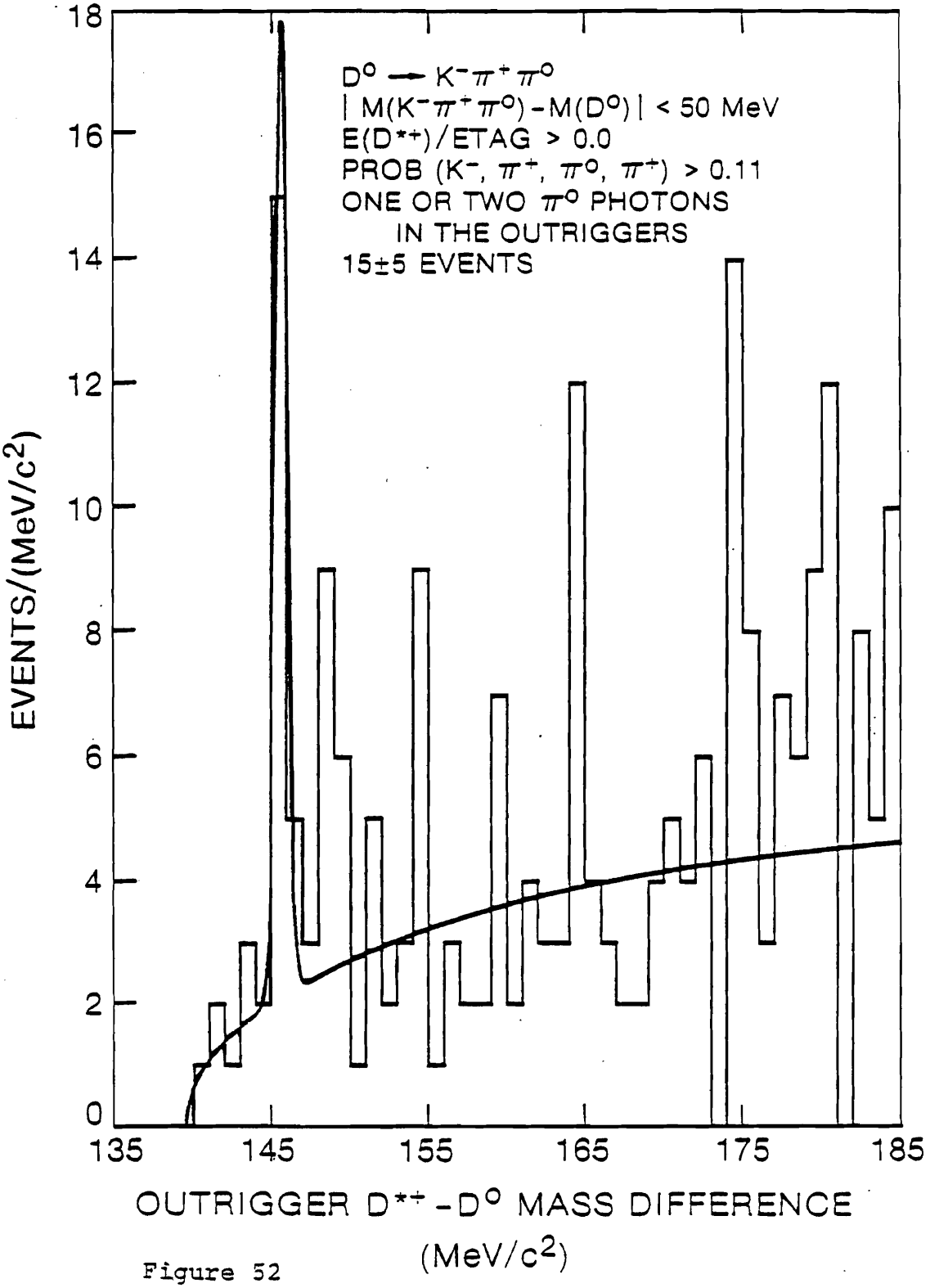
$D^0 \rightarrow K^-\pi^+\pi^0$
$|M(K^-\pi^+\pi^0) - M(D^0)| < 50$ MeV
$E(D^{*+})/ETAG > 0.0$
PROB $(K^-, \pi^+, \pi^0, \pi^+) > 0.11$
ONE OR TWO π^0 PHOTONS
IN THE OUTRIGGERS
15±5 EVENTS
EVENTS/(MeV/c²)
0
2
4
6
8
10
12
14
16
18
135
145
155
165
175
185
OUTRIGGER $D^{*+} - D^0$ MASS DIFFERENCE
(MeV/c²)

Figure 52

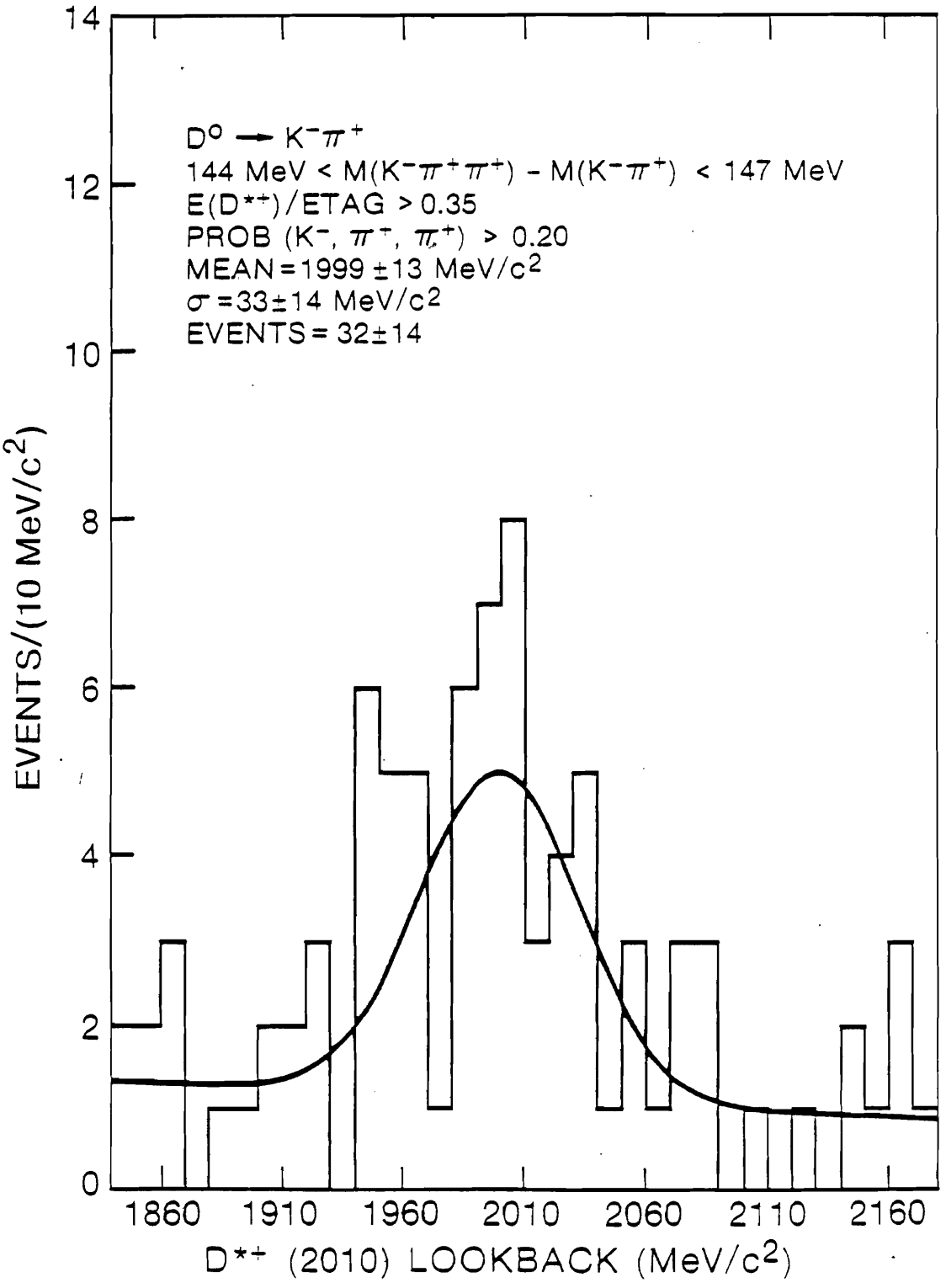
$D^0 \rightarrow K^-\pi^+$
144 MeV < M($K^-\pi^+\pi^+$) - M($K^-\pi^+$) < 147 MeV
E(D^{*+})/ETAG > 0.35
PROB (K^-, π^+, π^+) > 0.20
MEAN = 1999 ±13 MeV/c^2
σ = 33±14 MeV/c^2
EVENTS = 32±14
EVENTS/(10 MeV/c^2)
0
2
4
6
8
10
12
14
1860
1910
1960
2010
2060
2110
2160
D^{*+} (2010) LOOKBACK (MeV/c^2)

Figure 53

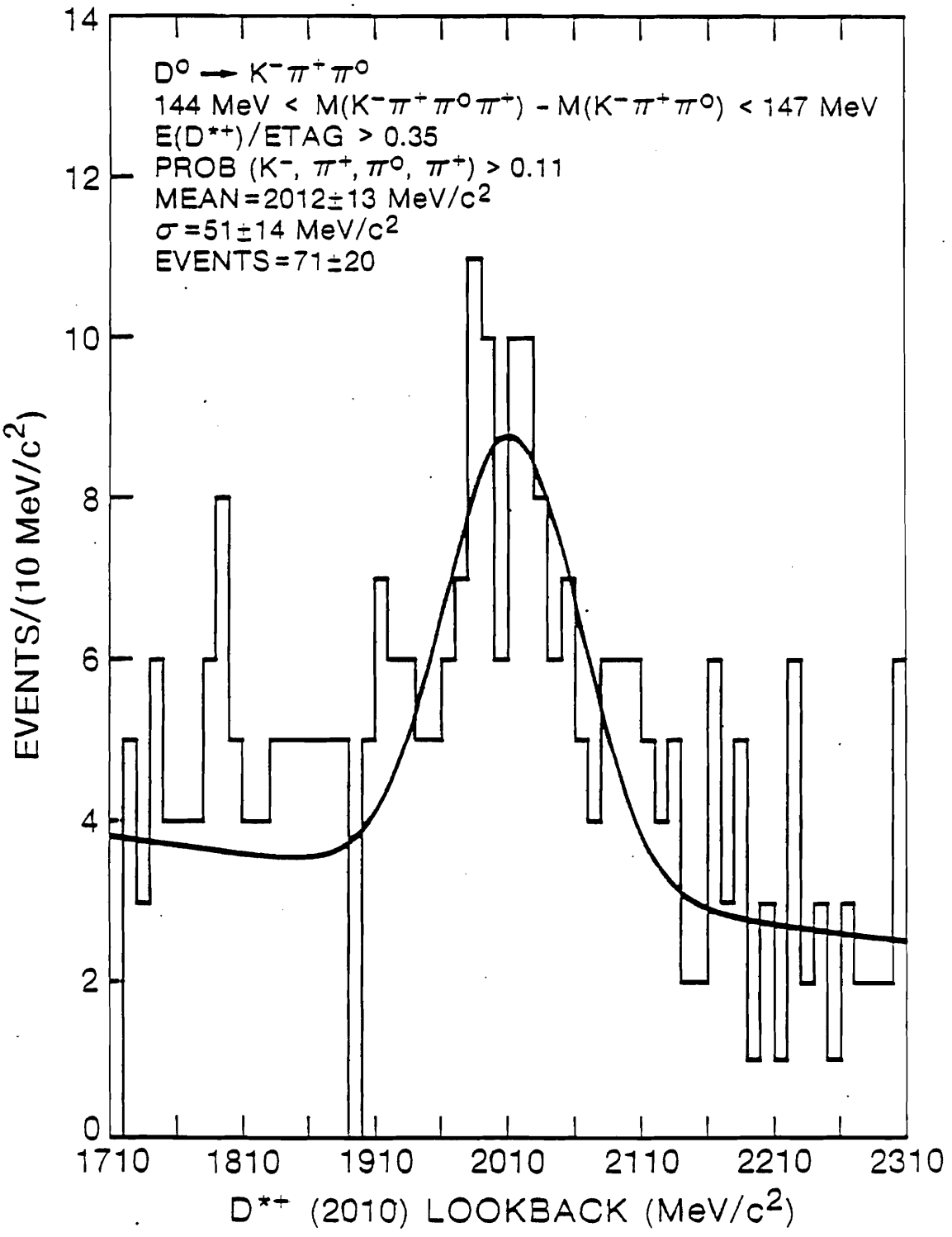
$D^0 \rightarrow K^-\pi^+\pi^0$
144 MeV < $M(K^-\pi^+\pi^0\pi^+) - M(K^-\pi^+\pi^0)$ < 147 MeV
$E(D^{*+})/ETAG > 0.35$
PROB (K^-, π^+, π^0, π^+) > 0.11
MEAN = 2012±13 MeV/c^2
σ = 51±14 MeV/c^2
EVENTS = 71±20
EVENTS/(10 MeV/c^2)
0
2
4
6
8
10
12
14
1710
1810
1910
2010
2110
2210
2310
D^{*+} (2010) LOOKBACK (MeV/c^2)

Figure 54

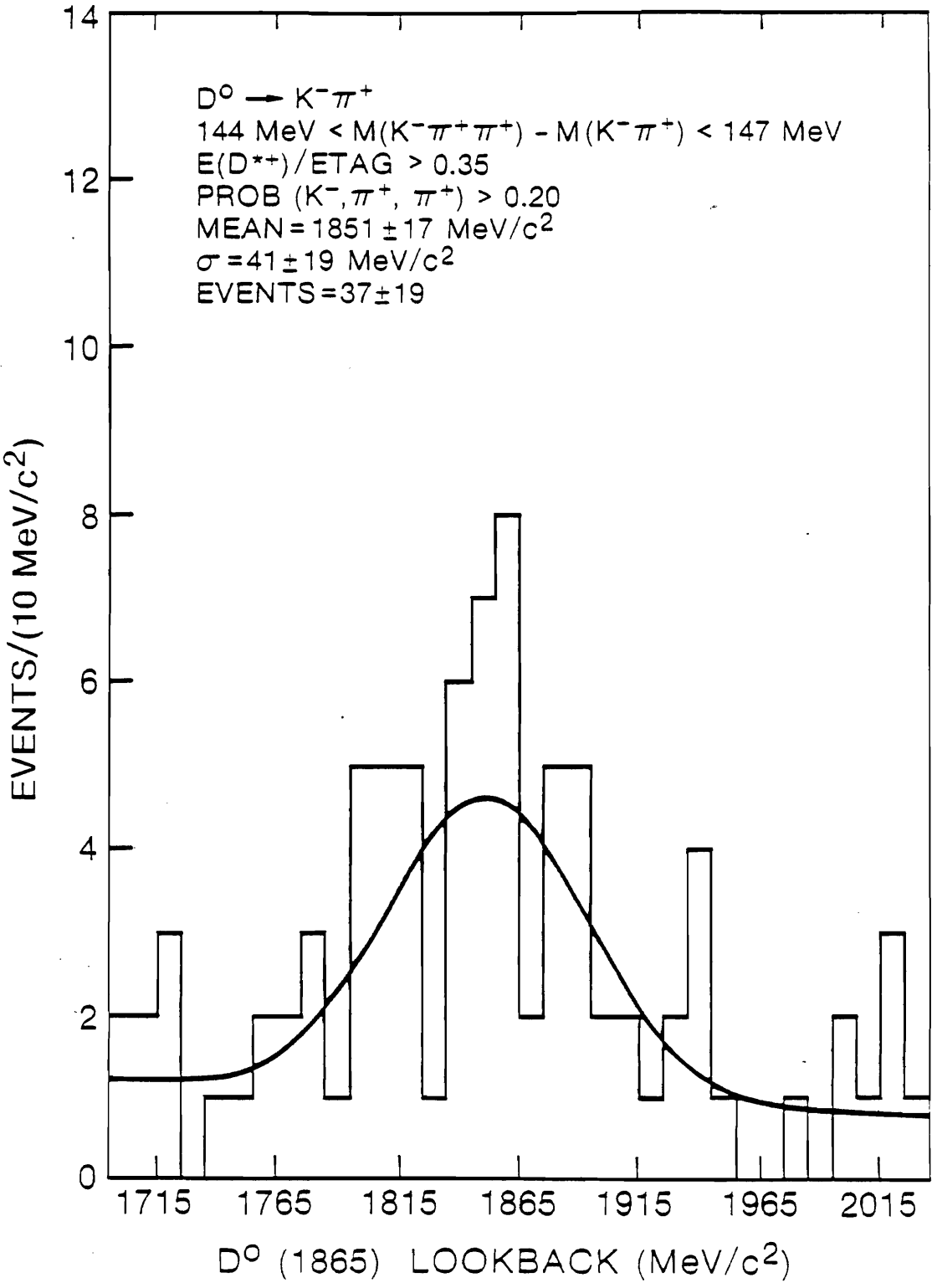
$D^0 \rightarrow K^-\pi^+$
144 MeV < M($K^-\pi^+\pi^+$) - M($K^-\pi^+$) < 147 MeV
E(D^{*+})/ETAG > 0.35
PROB (K^-,π^+, π^+) > 0.20
MEAN = 1851 ± 17 MeV/c^2
σ = 41 ± 19 MeV/c^2
EVENTS = 37 ± 19
EVENTS/(10 MeV/c^2)
0
2
4
6
8
10
12
14
1715
1765
1815
1865
1915
1965
2015
D^0 (1865) LOOKBACK (MeV/c^2)

Figure 55

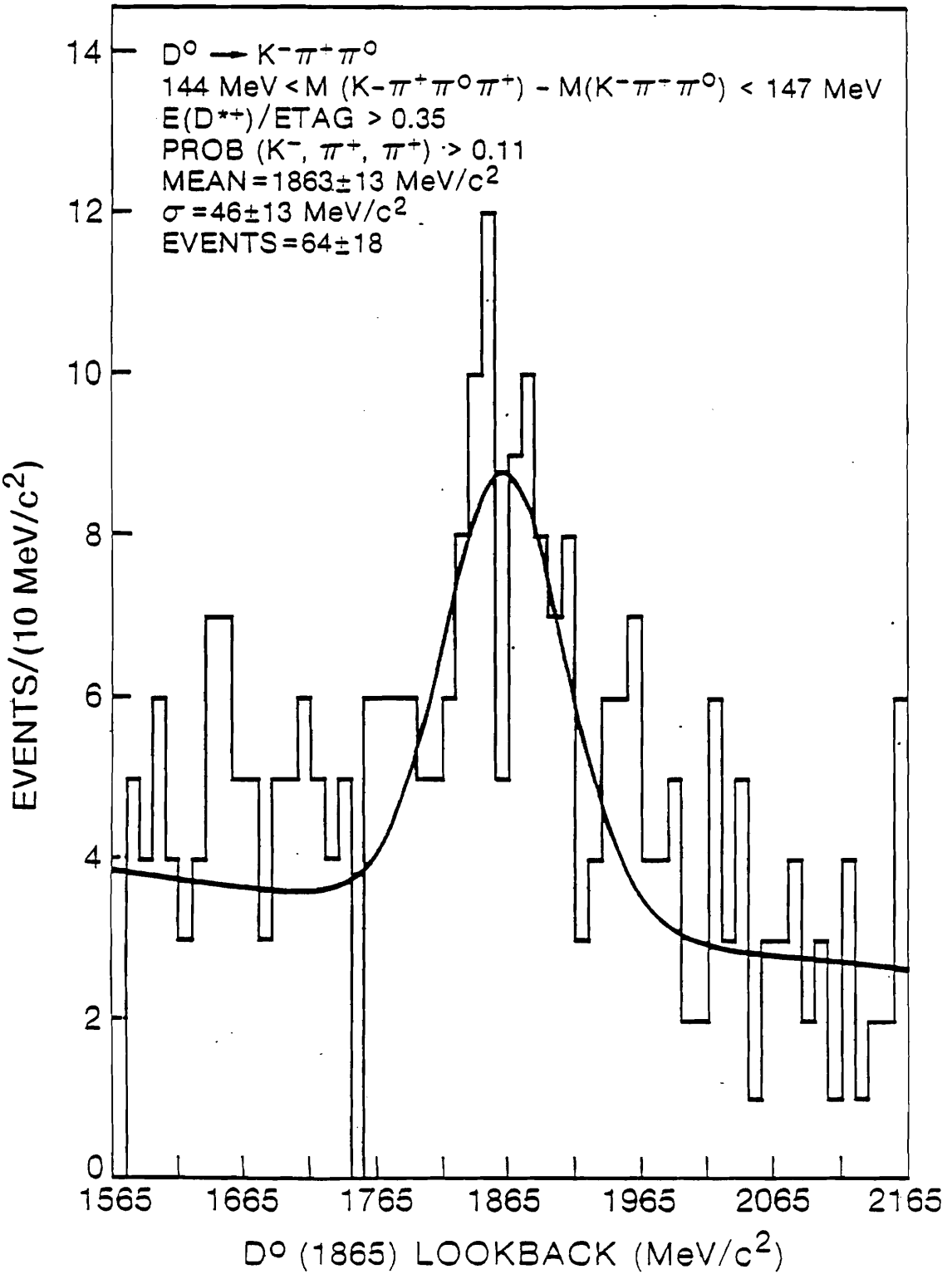
$D^0 \rightarrow K^-\pi^+\pi^0$
144 MeV < M ($K^-\pi^+\pi^0\pi^+$) - M($K^-\pi^-\pi^0$) < 147 MeV
E(D^{*+})/ETAG > 0.35
PROB (K^-, π^+, π^+) > 0.11
MEAN = 1863±13 MeV/c^2
σ = 46±13 MeV/c^2
EVENTS = 64±18
EVENTS/(10 MeV/c^2)
0
2
4
6
8
10
12
14
1565
1665
1765
1865
1965
2065
2165
D^0 (1865) LOOKBACK (MeV/c^2)

Figure 56

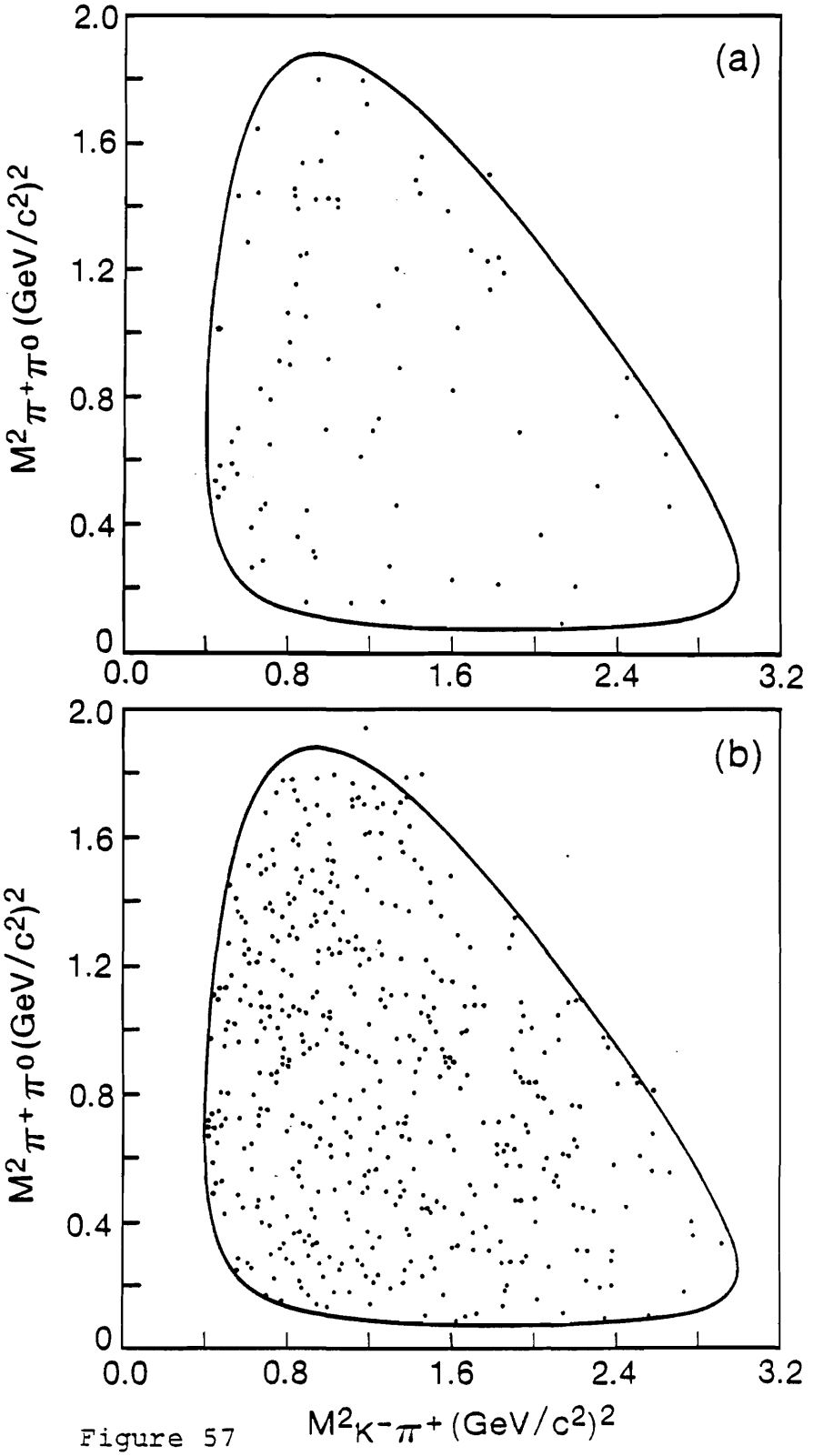

Figure 57

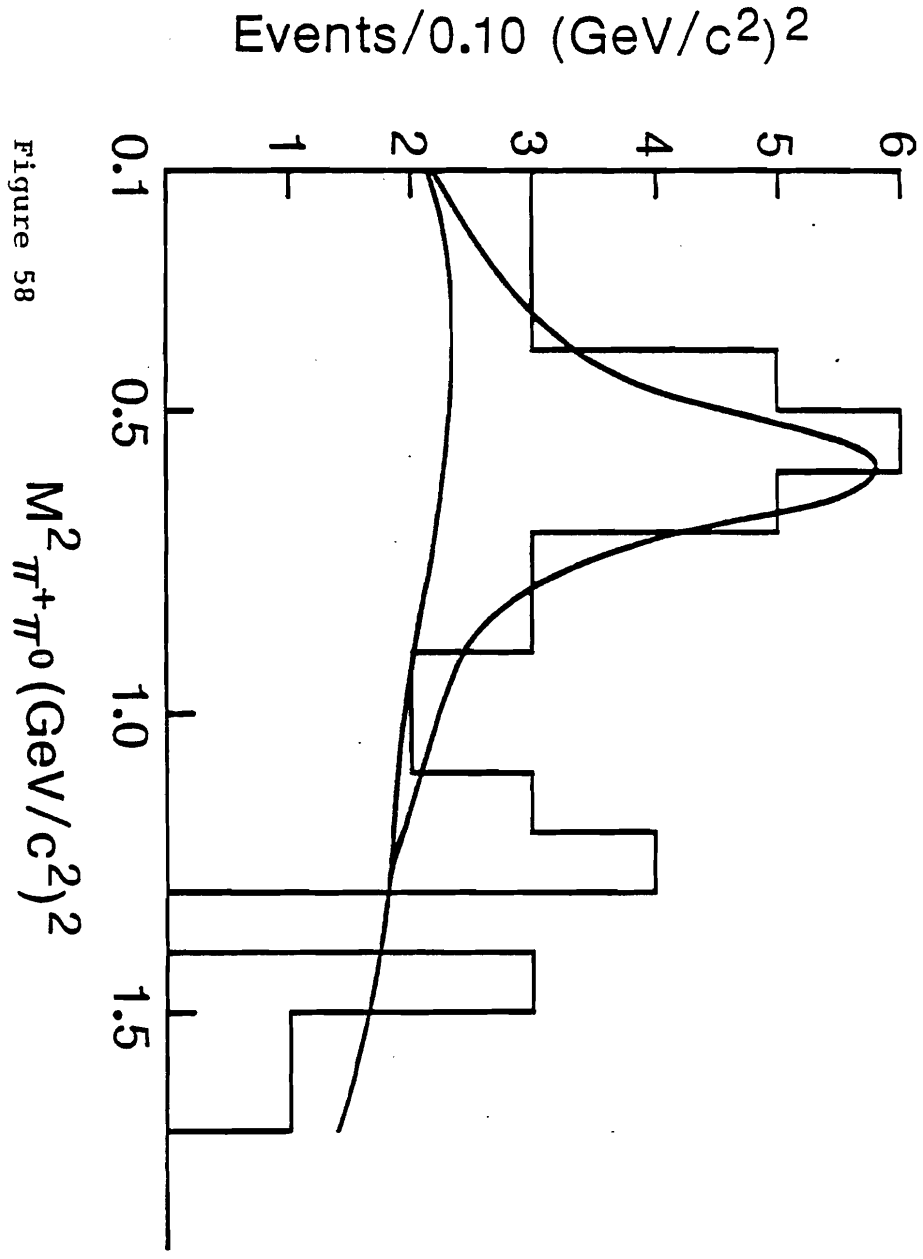

Figure 58

REFERENCES AND FOOTNOTES

[1] M. J. Losty et alii (Particle Data Group), Review of Particle Properties, Physics Letters 111B (1982).

[2] R. H. Schindler et alii (MARK II), Measurements of the Properties of D-Meson Decays, Physical Review D24 (1981) 78.

[3] George H. Trilling, The Properties of Charmed Particles, Physics Reports 75 (1981) 57.

[4] Steven Weinberg, A Model of Leptons, Physical Review Letters 9 (1967) 1264.

[5] Steven Weinberg, Effects of a Neutral Intermediate Boson in Semileptonic Processes, Physical Review D5 (1972) 1412.

[6] A. Salam, Elementary Particle Theory, edited by N. Svartholm, Almquist and Forlag, Stockholm (1968) 367.

[7] Jim Pinfold, A Study of Hadronic and Semi-Leptonic Neutral Current Events in Complex Nuclei, Ph.D. Thesis, London University, London, England (1977).

[8] A. Benvenuti et alii, Observation of Muonless Neutrino-Induced Inelastic Interactions, Physical Review D32 (1974) 800.

[9] M. Banner et alii (UA2 Collaboration), Observation of Single Isolated Electrons of High Transverse Momentum in Events with Missing Transverse Energy at the CERN $p\bar{p}$ Collider, Physics Letters 122B (1983) 476.

[10] G. Arnison et alii (UA1 Collaboration), Experimental Observation of Lepton Pairs of Invariant Mass around 95 GeV/c^2 at the CERN SPS Collider, Physics Letters 126B (1983) 398.

[11] G. Arnison et alii (UA1 Collaboration), Further Evidence for Charged Intermediate Vector Bosons at the SPS Collider, Physics Letters 129B (1983) 273.

[12] S. L. Glashow, J. Iliopoulos, and L. Maiani, Weak Interactions with Lepton-Hadron Symmetry, Physical Review D2 (1970) 1285.

[13] Martin Gorn, Problems in Comparing Diagrams with Group Theory in Non-Leptonic Decays, Nuclear Physics B191 (1981) 269.

[14] Ling-Lie Chau, Quark Mixing in Weak Interactions, Physics Reports 95 (1983) 1.

[15] Sinan Kaptanoglu, Nonleptonic Charmed-Meson Decays, Physical Review D18 (1978) 1554.

[16] C. Quigg and Jonathan L. Rosner, Hadronic Decays of Charmed Mesons, Physical Review D17 (1978) 239.

[17] Murray Peshkin and Jonathan L. Rosner, Isospin Restrictions on Charge Distributions in Charmed-Particle Decays, Nuclear Physics B122 (1977) 144.

[18] I. Bigi and L. Stodolsky, Quark Line Rule for Non-Leptonic Decays, SLAC-PUB-2410 (October 1979).

[19] Masahisa Matsuda et alii, Comments on the D-Meson Decays, Progress in Theoretical Physics 59 (1978) 1396.

[20] J. Appel et alii, The Tagged Photon Magnetic Spectrometer: Facility Design Report, Fermilab (May 1977).

[21] G. Gidal, B. Armstrong, and A. Rittenberg, Major Detectors in Elementary Particle Physics, LBL-91 Supplement UC-37 (March 1983).

[22] Bruce Hayes Denby, Inelastic and Elastic Photoproduction of J/ψ (3097), Ph.D. thesis, University of California, Santa Barbara, 1983 (unpublished).

[23] Alan L. Duncan, Characteristics of Hadronic States Observed in High Energy Diffractive Photoproduction in Hydrogen, Ph.D. thesis, University of Colorado, Boulder, 1982 (unpublished).

[24] R. R. Wilson and E. L. Goldwasser, National Accelerator Laboratory Design Report (January 1968).

[25] G. F. Hartner et alii, A Recoil Proton Detector Using Cylindrical Proportional Chambers and Scintillation Counters, Nuclear Instruments and Methods 216 (1983) 113.

[26] R. Yamada, J. Dinkel, R. J. Wojslaw, and C. D. Buchanan, Fermilab Magnet Mapping System, Nuclear Instruments and Methods 138 (1976) 567.

[27] C. Lechanoine, M. Martin, and H. Wind, Method for Efficient Magnetic Analysis in an Inhomogeneous Field, Nuclear Instruments and Methods 69 (1969) 122.

[28] H. Wind, Evaluating a Magnetic Field from Boundary Observations Only, Nuclear Instruments and Methods 84 (1970) 117.

[29] Henk Wind, Where Should a Magnetic Field Be Measured?, IEEE Transactions on Magnetics MAG-5 (1969) 269.

[30] C. W. Allen, Astrophysical Quantities Third Edition, Atholone Press, London (1973) 92.

[31] J. D. Jackson, Classical Electrodynamics, Second Edition, Wiley, New York (1975) 199.

[32] CO-NETIC AA alloy H_2 perfection annealed sheet is a nickel alloy made by the Magnetic Shield Division, Perfection Mica Company, 740 North Thomas Drive, Bensenville, Illinois.

[33] Both PIFAX plastic core P-140 and quartz core S-140 fiber optic cables from DuPont's Plastic Products and Resins Department in Wilmington, Delaware were used in the Outriggers. Even though the few quartz fibers employed received less light, due to their smaller core diameters, their lower attenuation in the 72 foot run to the Outriggers made them more than competitive.

[34] The values for radiation lengths, nuclear collision lengths, and nuclear interaction lengths are from Reference [1]. These three values for steel are 1.76cm, 10.2cm, and 17.1cm. For aluminum the values are 8.9cm, 25.5cm, and 37.2cm. For lead the numbers are 0.56cm, 9.8cm, and 18.5cm. The tungsten values are 0.35cm, 5.6cm, and 10.3cm. Lucite ($C_5H_8O_2$) and not scintillator was used for the C-Counters. Lucite's values are 34.5cm, 48.9cm, and 65.0cm. The values for polystyrene $(CH)^K$, 42.9cm, 55.2cm, and 68.5cm, are used for the plastic scintillator in the Outriggers and the Hadrometer. These numbers are divided by the ratio of the density of liquid scintillator to polystyrene (0.858/1.032 = 0.831) to yield 51.6cm, 66.4cm, and 82.4cm for the SLIC.

[35] V. Bharadwaj et alii, An Inexpensive Large Area Shower Detector with High Spatial and Energy Resolution, Nuclear Instruments and Methods 155 (1978) 411.

[36] V. Bharadwaj et alii, A Large Area Liquid Scintillator Multiphoton Detector, University of California at Santa Barbara (unpublished).

[37] Herbert Goldstein, Classical Mechanics, Addison-Wesley, Reading, Massachusetts (1950) 124.

[38] James T. Kenney, Project Engineers, 1675 Elevado, Arcadia, California 91006.

[39] C. Kerns, Photomultiplier Tube Base, Annual Report of the Fermi National Accelerator Laboratory (1980) 146.

[40] E. Barsotti, J. A. Appel, M. Haldeman, R. Hance, B. Haynes, J. Maenpaa, T. Nash, T. Soszynski, K. Treptow, S. Bracker, A Modular Trigger Processing System for High Energy Physics Experiments, IEEE Transactons on Nuclear Science NS-26 (1979) 686.

[41] J. Martin et alii, Use of the ECL-CAMAC Trigger Processor System for Recoil Missing Mass Triggers at The Tagged Photon Spectrometer at Fermilab, Proceedings of the Topical Conference on the Applications of Microprocessors to High Energy Physics Experiments, CERN 81-07 (1981) 164.

[42] T. Nash, A Review of Programable Systems Associated with Fermilab Experiments, ibidem, p. 132.

[43] T. Nash, Specialized Computers for High-Energy Experiments, Physics Today (May 1983) 36.

[44] Jon Mathews and R. L. Walker, Mathematical Methods of Physics, Second Edition, Benjamin, Menlo Park, California (1970) 375.

[45] Robert I. Jennrich, Stepwise Regression, in Statistical Methods for Digital Computers, Edited by Kurt Enslein, Anthony Ralston and Herbert S. Wilf, Chapter 4, Wiley, New York, (1977).

[46] N. R. Draper and H. Smith, Applied Regression Analysis, Second Edition, Wiley, New York (1981).

[47] B.H. Denby et alii, Inelastic and Elastic Photoproduction of J/ψ(3097), Physical Review Letters 52 (1984) 795.

[48] R. L. Ford and W. R. Nelson, The EGS Code System: Computer Programs for the Monte Carlo Simulation of Electromagnetic Cascade Showers (Version 3), SLAC Report No. 210, (June 1978).

[49] W. R. Nelson, Applicaton of EGS to Detector Design in High Energy Physics, Proceedings of the Second International School of Radiation Damage and Protection, Plenum, New York (1980) 239.

[50] D. J. Summers et alii, Study of the Decay $D^0 \to K^- \pi^+ \pi^0$ in High-Energy Photoproduction, Physical Review Letters 52 (1984) 410.

[51] K. Sliwa et alii, A Study of D* Production in High-Energy γp Interactions, FERMILAB-Pub-83/96 EXP 7320.516 (November 1983)

[52] Bill Schmidke, Derivation of Optimal Cut Algorithm, Internal E516 Report, Fermilab (May 1982).

[53] Jay Orear, Notes on Statistics for Physicists, UCRL-8417, University of California, Radiation Laboratory, Berkeley (1958).